
A Study of Singularities in Homotopy Continuation for Kinematic Applications

Caroline Therese Hills

Publication Date

06-11-2024

License

This work is made available under a All Rights Reserved license and should only be used in accordance with that license.

Citation for this work (American Psychological Association 7th edition)

Hills, C. T. (2024). *A Study of Singularities in Homotopy Continuation for Kinematic Applications* (Version 1). University of Notre Dame. <https://doi.org/10.7274/27569475.v1>

This work was downloaded from CurateND, the University of Notre Dame's institutional repository.

For more information about this work, to report or an issue, or to preserve and share your original work, please contact the CurateND team for assistance at curate@nd.edu.

A STUDY OF SINGULARITIES IN HOMOTOPY CONTINUATION FOR
KINEMATIC APPLICATIONS

A Dissertation

Submitted to the Graduate School
of the University of Notre Dame
in Partial Fulfillment of the Requirements
for the Degree of

Doctor of Philosophy

by
Caroline Therese Hills

Jonathan D. Hauenstein, Director

Graduate Program in Applied and Computational Mathematics and Statistics
Notre Dame, Indiana

November 2024

© Copyright by

Caroline T. Hills

2024

All Rights Reserved

A STUDY OF SINGULARITIES IN HOMOTOPY CONTINUATION FOR
KINEMATIC APPLICATIONS

Abstract

by

Caroline Therese Hills

Task requirements and positions of robotic kinematic systems can be represented by a system of polynomial equations. The use of homotopy continuation, a numerical method from algebraic geometry, solves these systems and analyzes their solution sets. However, these systems are plagued by branch points, and homotopy paths passing within proximity to these points experience ill-conditioning leading to computational burdens and even numerical failures. Although branch points negatively impact homotopy continuation methods, one can leverage knowledge regarding these points for solving and analyzing kinematic systems. First, we present a holistic consideration of the presence of branch points in homotopy systems of generic cases and an applied kinematic problem. We study the distribution of the image of branch points, ramification points, compactified to the Riemann sphere for select combinations of start and end systems of a homotopy. We compute metrics to assess the uniformity of the ramification point distribution and observe methods that impact that distribution, including the use of specially structured start systems and scaling coefficients. Next, we consider the complete computation of solution sets for the four-bar optimal path synthesis problem in kinematics. As task requirements become more complex, so do their resulting systems, ultimately leading one to consider an optimization formulation such as the least-squares approximation. Homotopy con-

tinuation methods, namely the use of random monodromy loops, can be employed to these polynomial formulations to yield a nearly, if not totally, complete solution set starting from a single seed solution. We consider three scenarios of the optimal path synthesis with no, one, and two pivots pre-specified and applied examples for each scenario. Lastly, we propose a method for kinematic path planning that incorporates topological ideas into computing a radius graph representation of the workspace for a five-bar mechanism. The workspace of a five-bar mechanism is a manifold possessing extra folds that, when projected into a 2D view, appears to admit additional internal boundaries. The mechanism satisfies additional constraints at these boundaries, but only a portion of those boundaries should be avoided due to unfavorable transmission qualities displayed by the five-bar. Our method identifies and removes these boundaries in a workspace discretization while preserving characteristics of the workspace manifold. We sample a sufficient number of points from the configuration space such that we preserve topological features of the manifold. Then, through homotopy applications, we identify and remove problematic boundaries from our viable workspace discretization for use in path-planning algorithms. We apply our method to two path-planning examples and show the resulting path and joint actuations taken by the five-bar mechanism.

To the loving memory of my grandfather, Raymond R. Rapala

CONTENTS

Figures	vi
Tables	x
Acknowledgments	xi
Chapter 1: Introduction	1
Chapter 2: Background	7
2.1 Numerical Algebraic Geometry	7
2.1.1 Nonsingular and singular solutions	7
2.1.2 Homotopy continuation theory	9
2.1.3 Parameter homotopies	13
2.1.4 Random monodromy loops	14
2.2 Kinematics of Planar Mechanisms	17
2.2.1 Isotropic coordinates	18
2.2.2 Four-bar mechanisms	19
2.2.2.1 Kinematic loop equations	20
2.2.2.2 Configuration space and singularities	21
2.2.3 Five-bar mechanisms	23
2.2.3.1 Kinematic loop equations	23
2.2.3.2 Configuration space and singularities	24
Chapter 3: Distribution of Homotopy Branch Points	25
3.1 Introduction	25
3.2 Pencils, Branch Points, and Sphere Mappings	31
3.2.1 Projective space and pencils	31
3.2.2 Branch points	32
3.2.3 Riemann sphere	33
3.2.4 Visualization of branch points	34
3.3 Computing Branch Points	37
3.4 Impact of Branch Points	42
3.4.1 Distance to ramification points	42
3.4.2 Probability of failure	43
3.4.3 Endgame failure	48

3.4.4	Scaling	54
3.4.5	Condition number near branch points	57
3.5	Examples	60
3.5.1	Quadratic systems	60
3.5.2	Precision point path synthesis	64
3.6	Conclusion and Discussion	69
Chapter 4: Complete Solution Sets of Four-Bar Approximate Path Synthesis		74
4.1	Introduction	74
4.1.1	Literature review	76
4.2	Mathematical Formulation	78
4.2.1	Approximate synthesis equations	78
4.2.2	Random monodromy loops	86
4.2.3	Schnabel estimator	88
4.2.4	Trace test	88
4.3	The General Case (No Pre-specification of Dimensions)	89
4.3.1	Ab initio computation	89
4.3.2	Solution set validation	91
4.3.3	Applied example	91
4.4	Pre-specification of One Ground Pivot	96
4.4.1	Ab initio computation	96
4.4.2	Solution set validation	97
4.4.3	Applied example	97
4.5	Pre-specification of Both Ground Pivots	98
4.5.1	Ab initio computation	98
4.5.2	Solution set validation	100
4.5.3	Applied example	100
4.6	Discussion	102
4.7	Conclusions	103
4.8	Acknowledgment	104
Chapter 5: Output Modes of a Five-Bar Mechanism		110
5.1	Introduction	111
5.2	Background	112
5.3	Method	115
5.3.1	Sampling and graph construction	117
5.3.2	Singularity avoidance	118
5.3.3	Computational considerations	121
5.4	Results	122
5.4.1	Perpendicular velocity ellipses at an x - y point	122
5.4.2	A ceiling and a floor	123
5.5	Conclusions	124

Appendix A: Kinematic Derivations	131
A.1 Four-Bar Mechanism	131
A.1.1 Forward kinematics	132
A.1.2 Inverse kinematics	135
A.2 Five-Bar Mechanism	136
A.2.1 Forward kinematics	136
A.2.2 Inverse kinematics	137
Appendix B: Cognate Transforms and Solution Values for Chapter 4	139
B.1 Cognate Transformations for the General Case Formulation	139
B.2 Cognate Transformations for the Pre-specification of One Ground Pivot	139
B.3 Design Positions and Parameters for the Applied Examples	140
B.4 Solution Values for the Applied Examples	140
B.4.1 The general case (no dimensions pre-specified)	144
B.4.2 One dimension pre-specified	147
B.4.3 Two dimensions pre-specified	149
Bibliography	152

FIGURES

1.1 Graphical abstract of research contributions for Chapter 4	4
2.1 A successful parameter homotopy from start system $F(x; p_s)$ to target system $F(x; p_f)$	11
2.2 A homotopy from start system $G(x)$ to target system $F(x)$ with the red paths converging to an isolated singular point and the dashed path diverging off to a solution at infinity.	12
2.3 Graphical representation of the Riemann surface of $w = \sqrt{z}$. The monodromy loop follows the dashed path that starts at the parameters p^* , circles around the branch cut that when projected down is a closed loop, and returns to a new solution that lies on the fiber of which p^* is the projection in the parameter space.	15
2.4 A visual representation of the RML described in Eqns. 2.8a, 2.8b, 2.8c and applied in Chapter 4. The starting points that were not returned to at the end of the RML are denoted in blue; the solution that is a member of both the start and end solution sets is denoted in pink; new solutions found by the RML are denoted in green.	16
2.5 Three planar mechanisms of a serial 2R (left), four-bar (middle), and five-bar (right).	18
3.1 Illustrating on a small region the logarithm of the maximum condition number for each solution in relationship to the location of the ramification points (black). Proximity to ramification points increases the maximum condition number in the surrounding space resulting in “hot spots.”	30
3.2 Ramification point scatter plot and heat map for $N = 6$ in Example 9.	36
3.3 Histograms of longitude and z -coordinate for $N = 6$ in Example 9.	37
3.4 Detail of $\delta_j(\theta)$ and $\delta_{\min}(\theta)$ for $N = 6$ in Example 9. Here, several plots of $\delta_j(\theta)$ are shown as dashed V-shape centered at each longitude θ_j while $\delta_{\min}(\theta)$ is overlaid in solid blue.	44
3.5 Probability of δ^* -failure, P_{fail} , versus normalized safe distance $\widehat{\delta^*}$ for Example 9 and its rescaled counterpart from Section 3.4.4. The diagonal line shows the slope expected from a uniform distribution of branch points.	47

3.6	Ramification point scatter plot and heat map for $k = 3$ in Example 22.	55
3.7	Histogram counts for number of ramification points for Example 22 with $k = 3$ along longitude $[0^\circ, \pm 180^\circ]$ (left) and the z -coordinate $[-1, 1]$ (right).	56
3.8	Probability of δ^* -failure, P_{fail} , versus normalized safe distance $\hat{\delta}^*$ for Example 22, $k = 3$. The diagonal red line shows the slope expected from a normal distribution of branch points. The green dotted line is the actual slope of P_{fail} , plotted in blue. The exceptional location of a ramification point close to the pole triggers $\hat{\delta}^*$ -failure at $\hat{\delta}^* \approx 0.69$	56
3.9	Ramification point density after scaling the start system of Example 9. Compare to Fig.s 3.2 and 3.3, and note change of scale in the color bar and the histogram counts.	58
3.10	Log-log plot comparing $\ \tau - \tau^*\ $ with the condition number of $H_u(u(\tau), \tau)$ as $\tau \rightarrow \tau^*$ with the slope being approximately $-\frac{1}{2}$	59
3.11	Histograms of the longitude of the ramification points for the six cases with $N = 12$	62
3.12	Histograms of the z -coordinates of the ramification points for the six cases with $N = 12$	63
3.13	Comparison of P_{fail} for the six cases with $N = 6, 8, 10, 12$	64
3.14	The seven-point path synthesis problem is to find all four-bars (one of which is drawn) whose coupler point passes through the precision points D_0, \dots, D_6 . Ground pivot A is given, but pivot B and the lengths of the five segments composing the mechanism are variables to be found.	67
3.15	Comparison of solving 7-point problem with one fixed pivot using (a) linear product start system and (b) dense start system. The scaling pushes ramification points towards the start system, resulting in a highly skewed z -coordinate histogram. To visualize this, the histogram plot of the z -coordinate on the right uses a logarithmic (\log_{10}) vertical axis.	70
3.16	Ramification point density for solving 7-point problem with one fixed pivot using (a) linear product start system and (b) dense start system.	71
4.1	Graphical summary of the proposed method for solving the approximate path synthesis design problem.	79
4.2	Schematic of a four-bar linkage for path synthesis.	79
4.3	Computational summary of the <i>ab initio</i> solving for the general case formulation showing (a) the ratio of repeat solutions per RML iteration and (b) the Schnabel estimates with 95% confidence intervals.	90

4.4	The six-bar mechanism and coupler curve used for the applied example of the general case.	92
4.5	Example solutions of applied problem for the general case formulation that exhibit branch and circuit defective behavior.	94
4.6	Computational summary of the <i>ab initio</i> solving when one ground pivot is pre-specified showing (a) the ratio of repeat solutions per RML iteration and (b) the Schnabel estimates with 95% confidence intervals.	105
4.7	A candidate design from the pre-specification of one ground pivot computation. (a)‘After making contact with the work surface. (b) Said surface pushes the gripper end up, relative to itself, and into a work-piece to be gripped. Contact with the work surface actuates the gripper, and the four-bar linkage guides its end into the workpiece. (c) Such a gripper might comprise of two pairs of opposing halves.	106
4.8	The solution design exhibiting preferred design characteristics for the one dimension pre-specified example.	107
4.9	Ratio of repeat solutions per RML iteration when both ground pivots are pre-specified.	107
4.10	The chosen solution from which the final design was derived.	108
4.11	Three snapshots, namely, a stowed configuration, an intermediate configuration and a deployed configuration, of deployable aircraft wing mechanism.	108
4.12	(a) The gripper prototype in action. (b) Lifting a 100g weight. (c) From a side view, preparing to grab a plastic card.	109
5.1	Views of the configuration spaces of a serial 2R (left) and a parallel five-bar (right). 1st row: The output workspace for each manipulator. 2nd row: The 2R admits two IK solutions, the five-bar admits four. 3rd row: The input actuator space for each manipulator, with holes visible for the five-bar. 4th row: An (x, y, ψ) view of the configuration manifold. The skewering line shows the locations of the IK solutions for a set (x, y)	125
5.2	Schematic of a five-bar mechanism. The velocity ellipse with respect to the input angles ϕ and ψ is shown at its end-effector (x, y)	126
5.3	Example 1: At the x - y point shown, there exists another configuration with a velocity ellipse perpendicular to the one displayed.	127
5.4	Example 1: A feasible path marked with six snapshots, marked alphabetically from A to E, to switch between the configurations corresponding to two perpendicular velocity ellipses. The workspace and the input singularity curves shown correspond to the output mode to which each configuration belongs. Output modes are distinguished by color.	128

5.5	Example 2: The portion of the output bound which functions as a ceiling or floor is indicated with a box.	129
5.6	Example 2: A feasible path marked with six snapshots, marked alphabetically from A to E, for the ceiling-to-floor example. The workspace and the input singularity curves shown correspond to the output mode to which each configuration belongs. Output modes are distinguished by color.	130
A.1	The function $\arccos(\theta) = x$ is shown in the solid line along the circle; there are two solutions on the circle per value of θ	133
B.1	The computed solution, the global minimum, with the absolute smallest cost function for the zero dimensions pre-specified example.	144
B.2	The computed solution with the absolute smallest cost function for the one dimension pre-specified example.	147
B.3	The solution design, dimensions given in B.6, that bears the highest similarity to the reference design.	149
B.4	The computed solution with the absolute smallest cost function for the two dimension pre-specified example.	151

TABLES

3.1 Probability of failure slopes, $S = \frac{dP_{\text{fail}}}{d\delta^*}(0)$ for the six cases: expected value, $\mathbb{E}(S)$; actual value, S (rounded off).	65
3.2 Minimum latitude for the six cases: number of branch points, M ; expected minimum latitude, E_M ; actual minimum latitude, ϕ_{\min} ; and $cdf(\phi_{\min})$	66
4.1 Exponents (a, b) for the 47 moments in the general case	84
4.2 Exponents (a, b) for the 41 moments when one or both ground pivots are pre-specified	85
4.3 Table of Fig 4.5 solutions and their dimensions and error metrics. . .	95
4.4 Numerical values of the final chosen design solution for the one dimension pre-specified applied example.	99
5.1 Five-bar dimensions for the two examples	126
5.2 Summary of the radius graphs for the two examples	126
B.1 Numerical values of the 47 continuous moments of the general case applied example.	141
B.2 Design positions of the applied example for the pre-specification of one ground pivot formulation.	142
B.3 Design positions of the applied example for the pre-specification of both ground pivots formulation	143
B.4 The dimensions of the top ten solutions as per lowest absolute cost value for the General Case example. Note that Fig. 4.5(b), Fig. 4.5(a), and Fig. 4.5(d) are the third, fifth, and ninth lowest costs, respectively.	145
B.5 Table showing the dimensions of the ten lowest absolute costs values for the one dimension pre-specified applied example.	146
B.6 Numerical values of the one dimension pre-specified solution shown in Fig. B.3 that bears the highest resemblance to the reference path. . .	148
B.7 Table showing the dimensions of the ten lowest absolute costs values for the two dimension pre-specified applied example.	150

ACKNOWLEDGMENTS

This dissertation marks more than the completion of a PhD; it is the culmination of my formal education completed exclusively at Notre Dame. From professors, classmates, friends, and rowing coaches and teammates, there are countless people who have influenced my time at Notre Dame and to whom I extend my appreciation.

First, I would like to thank my advisor Dr. Jonathan Hauenstein who gave me my first experience in math research and without whom this dissertation would not have been possible. I would also like to thank my collaborators: Dr. Mark Plecnik, Dr. Aravind Baskar, Dr. Charles Wampler, Dr. Andrew Sommese, Dr. Parker Edwards, and Dr. Taylor Brysiewicz. I am very honored and lucky to have had the opportunities to work with you. Thank you to the ACMS Department as a whole, especially Melissa Ornat, Kathy Phillips, and Nancy Herman.

To the Research in Industrial Projects for Students team at the Institute for Pure and Applied Math at UCLA, especially Dr. Susana Serna, thank you for a fantastic experience that ignited my interest in pursuing this PhD; and to Dr. William Bachrach, thank you for the conversations that strengthened my PhD motivations even if they seemed intended to talk me out of pursuing this degree.

Beyond my beloved retreats to the Warren Dunes, I would like to express gratitude for the places this PhD journey has brought me, from Amsterdam to China Lake to Laurel, and for all the people I have met along the way. I would like to recognize the communities of support and camaraderie I found in World Gym Mishawaka, especially from Tony "tha Trainer" Lipsey, and St. Margaret's House South Bend.

Much love to my feline "co-author", Thelma, who made sure I had a cat in my lap

while writing and even during a few meetings. And Louise, too.

Thank you especially to my “adoptive parents”, Uncle Bryan and Aunt Chris, for being my home away from home.

Above all, the deepest and sincerest gratitude to my actual parents, Everett and Therese, who steadfastly weathered the highs and lows of this journey with me ever since I stepped onto Notre Dame’s campus for my first year of college.

CHAPTER 1

INTRODUCTION

Homotopy continuation is a method used to solve polynomial systems which arise in mathematical applications of science and engineering. By starting with a system G and its known solutions to $G = 0$, one can obtain the solutions for a target system F with unknown solutions to $F = 0$ by continuously deforming the solutions of G along parameterized paths connected to the solutions of F . This method for solving polynomial systems, known as homotopy continuation, is especially applicable to robotic kinematic synthesis problems, namely motion and path synthesis.

Robotic kinematics requires knowledge of the mechanism's geometry and dynamics in order to derive and solve expressions governing the motion and the path the mechanism must follow. Synthesis problems become more interesting when one considers *closed chain* mechanisms, where the joints of a mechanism are connected by leg links and the movement of select actuated joints drives the motion of the other legs. Four-bar mechanisms are a closed chain mechanism that trace one-dimensional curves in the plane [81]. Regarding motion synthesis, up to five orientations can be specified to which the mechanism's motion exactly configures, known as Burmester's problem [30]. In path synthesis, the mechanism can trace exactly through up to nine specified points, known as Alt's problem [3]. A combination synthesis of N specified motions and M specified points is known as a (M, N) Alt-Burmester problem [27, 115].

Since the solutions to robotic kinematic synthesis are algebraic subsets of a nonempty Zariski topology [36], it is of interest and efficiency to study these poly-

nomial systems arising in kinematics through the lens of algebraic geometry. Even more interesting is to employ *numerical algebraic geometry* methods to compute and analyze the solution sets, namely through homotopy continuation techniques. The *Bézout number* of a polynomial system is an upper bound to the generic root count that can be computed based on the degrees of the polynomial functions within the system [121]. While the above problems can have varied Bézout counts depending on their formulations, researchers have successfully computed their complete solution sets. Burmester in 1886 found at most six four-bars in the solution set to his five-pose problem [30]. Wampler, Morgan, and Sommese in 1992 computed the complete solution set to Alt’s Problem through numerical homotopy continuation and tracked 143,360 paths for 1,442 solution curves (applying cognate transformations and symmetries admits 8,652 total mechanism design solutions) [124]. Brake, Hauenstein, Murray, Myszka, and Wampler in 2016 solved the (M, N) Alt-Burmester problem in depth analyzing both the set’s dimension and degree for the possible (M, N) combinations [27].

A homotopy system admits branch points which are positive dimensional components [18, 81, 111]. Physically at these points a mechanism loses a degree of freedom in its movement; mathematically the system possesses a rank-deficient Jacobian matrix and ultimately a non-unique solution called a singular solution. A polynomial system that is structured with higher order terms and equations admits a larger Bézout bound on its generic root count [121]; it also admits a greater branch point count. Numerical algebraic geometry studies the computation of these solution sets, of which it is important to understand the complications of tracking through or nearby branch points especially when tracking a large number of homotopy paths.

This dissertation focuses on exploring numerical algebraic geometry concepts to understand the behavior of a homotopy system with regards to the distribution of ramification points, images of the branch points, and the effect of the branch points

on homotopy path tracking and solution computation. With this understanding, we consider applications of those ideas and methods to solve problems arising in kinematic analysis and synthesis. This work will describe the theoretical ideas to establish the complexity while moving towards chapters containing more applied work that showcase real world practicality.

Chapter 2 provides the reader with introductory mathematical derivations and definitions to terms and concepts utilized throughout this work both within numerical algebraic geometry and kinematics. While it will hopefully give the reader a solid background with which to read the proceeding chapters, it is a non-exhaustive list of all concepts contained within this work.

Chapter 3 inspects the distribution of homotopy ramification points compactified to the Riemann sphere through visualizations and probabilistic metrics. Homotopy continuation methods employ the “gamma trick” to guarantee a trackable homotopy, but this method does not guarantee the homotopy path will not pass near a branch point that would require smaller tracking steps or an increase in numerical precision [13]. Therefore, it is important to understand the potential distribution of those ramification points to gain an *a priori* understanding of the risk of failure when employing a homotopy in finite precision. We observe potential uniformity in the distribution of ramification points of a homotopy system and derive metrics with uniformity assumptions to analyze combinations of homotopy start and target systems. Our metrics include the measure of distance to ramification points for any path, the probability of failure curve for a homotopy system, and the expected minimum latitude of all the ramification points such that the homotopy continuation invokes a successful singular endgame. This is joint work with Andrew Sommese, Charles Wampler, and Jonathan Hauenstein.

Chapter 4 presents the nearly complete and complete solve of the four-bar optimal path synthesis problem, where the number of specified precision points is larger

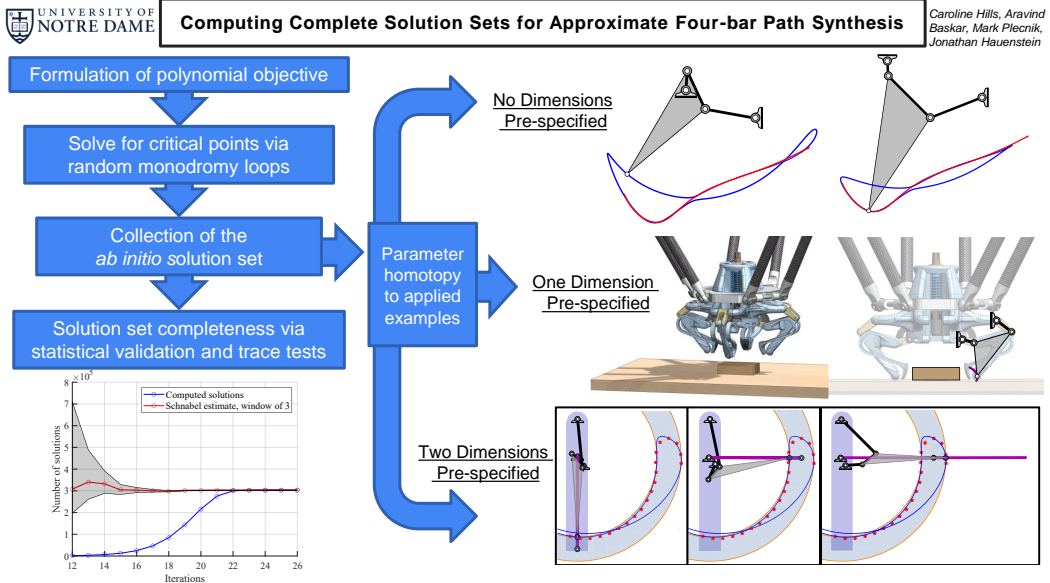


Figure 1.1. Graphical abstract of research contributions for Chapter 4.

than the maximum of nine presented in Alt's Problem [66]. The one-dimensional algebraic coupler curve synthesized by the mechanisms approximately passes through the prescribed precision points in the plane. To retain a polynomial system, we recast the problem as a least-squares minimization of the distance between coupler curve and the precision points; therefore one solves the optimization problem by solving for the critical points of the system. This requires solving a highly nonlinear system with a large Bézout bound, of which monodromy loops provide an efficient computation method requiring only one generic seed solution. These loops, when encircling a branch points of unknown locations, may return to different and unique solutions within the fiber of our original parameters, which we collect into a total solution set. As this solution set grows, one can assess the completeness through a variety of standards including statistical estimates inspired by biological studies and a geometric validation analysis known as the trace test. We present three different scenarios, each with their own applied example, using this optimization framework: a general

case with no simplifications, and two cases with one and two mechanism dimensions pre-specified. This chapter is a version of the work that has been published in Mechanism and Machine Theory [66]. It is joint work with Mark Plecnik, Aravind Baskar, and Jonathan Hauenstein.

Chapter 5 investigates the singular boundaries within a five-bar workspace. Five-bar mechanisms possess a multi-dimensional workspace manifold that, when projected to a two-dimensional view, appears to possess additional internal boundaries. At these boundaries, the five-bar exhibits a “singular” configuration as described by the collapse or infinite extension of the end-effector transmission ellipse axes. This requires the distinction between singularities [42] we sort into either Type I or Type II singularities. Type I singularities can be passed through with different joint actuation of the mechanism. Type II singularities are truly impassable boundaries inducing singular configurations that, once achieved, the mechanism cannot move from the position without exhibiting infinite and impossible forces. Since the expressions for the singularity curves are algebraic, one can compute the set at which this curve vanishes and use topological principles to create a radius graph workspace representation that retains the workspace’s characteristics. The sample points are homotopied to the nearest boundary curve and the resulting transmission characteristics of the mechanism are analyzed to determine the impassable singularity curves of the workspace. The result is a stronger resolution-complete domain of those boundaries that can be used in path-planning algorithms. This chapter is a version of the work that has been presented at the 2023 IEEE International Conference on Robotic and Automation [42]. It is joint work with Mark Plecnik, Aravind Baskar, Parker Edwards, and Jonathan Hauenstein.

Appendix A presents the derivation of the kinematic equations for planar four and five-bar mechanisms and a computer-friendly psuedocode of the algorithms. A brief background on the different kinematic problems and use of rotations is addition-

ally presented. The kinematic problems stem from the mechanism loop and coupler equations with different unknown variables for which one solves so these derivations also elucidate characteristics of a four-bar's configuration and coupler curve. These expressions for the four-bar mechanism can be generalized for use in visualizing the mechanism's configuration and/or coupler curve. After presenting the kinematic expressions for the four-bar mechanism, those of the five-bar are introduced, as they build from the equations of the four-bar.

Appendix B presents algebraic expressions for the relationships of Roberts' cognates for the General Case and Pre-specification of One Ground Pivot as described in Chapter 4, Sec. 4.3 and 4.4. The appendix also provides numerical values of the moment parameters to the three applied examples and, where applicable, the precision point values. The solutions with the ten lowest cost values and a visualization of the lowest cost mechanism are provided for each applied example. These solutions are classified as global or local minima or saddle points.

These works were supported in part by funding from the National Science Foundation, under Grant Nos. CMMI-2041789 and CCF-2331400.

CHAPTER 2

BACKGROUND

2.1 Numerical Algebraic Geometry

The study of the solution sets of polynomial systems is called algebraic geometry. The study of numerically computing and analyzing the solution sets to polynomials systems is known as *numerical algebraic geometry* [18].

2.1.1 Nonsingular and singular solutions

In mathematics, a function maps elements from one space to another. It is important to know if that mapping is unique, meaning it can be reversed to obtain the original elements, especially if the original space has certain defining features.

Example 1. Let $F(x; p) = x^2 - p^2$ where $x, p \in \mathbb{C}$; x is a solution variable of the system and p is a parameter to the system. If $p = 1$, then $F(x; 1) = x^2 - 1$. This expression has two solutions, $x = \{-1, 1\}$ called *isolated nonsingular solutions*.

Now let $p = 0$ such that $F(x; 0) = x^2$. The solution set only has one solution, $x = \{0\}$. This solution is a non-unique double root called a *isolated singular solution*.

Note that solution sets to polynomial systems are algebraic. The previous example had a singular point, but singularities can also be expressed as higher dimensional sets.

Remark 2. Let $F(x; p) = (x - p)^2$ and $G(x; p) = x - p$. In the latter expression, $x = p$ is the line of nonsingular solutions. For $F(x; p)$, this line is exclusively singular solutions.

In algebraic geometry, solution sets are broken down into *irreducible components* where singular solutions are called *positive dimensional sets* [24, 25].

Consider the case of a polynomial system, such as a differential equation. There are multiple theorems that state the conditions for the existence and uniqueness of a solution to an initial value differential equation [1, 71].

These theorems rely on smoothness and continuity of the function and its first derivative and, for sharper guarantees, boundedness of the derivative by a Lipschitz constant [71]. Solutions to differential equations violate the conditions needed for solution uniqueness when the Jacobian matrix of the variables is not full rank, or equivalently where the determinant of the Jacobian is zero. The Jacobian with respect to the variables x is defined as the operator J_x such that $J_x H = \frac{\partial H}{\partial x}$.

Remark 3. For the previous example, $J_x F = \frac{\partial F}{\partial x} = 2(x - p)$. If singularities occur when the determinant is zero then, $\det(J_x F) = 2(x - p) = 0$, which is just the line defined by $x = p$.

Example 4. Let $F(x_1, x_2) = \begin{bmatrix} x_1^2 + x_2^2 \\ x_1(x_1 + x_2) + 1 \end{bmatrix}$. This system consists of two quadric polynomials and admits 4 nonsingular solutions. The Jacobian at a point (x_1, x_2) is

$$J_x F = \begin{bmatrix} 2x_1 & 2x_2 \\ 2x_1 + x_2 & x_1 \end{bmatrix}.$$

This Jacobian is singular when $\det(J_x F) = 2x_1^2 - 4x_1x_2 - 2x_2^2 = 0$. Which occurs when $x_1 = (-1 \pm \sqrt{2})x_2$, which is two perpendicular lines intersecting at the origin.

At these points where the Jacobian matrix loses rank the tangent space is not similar to that of nearby points [18]. This leads to issues in computational and numerical methods.

2.1.2 Homotopy continuation theory

Homotopy continuation is a key method based in numerical algebraic geometry. A *homotopy* is a smooth function $H(x, t) : \mathbb{C}^N \times (0, 1] \mapsto \mathbb{C}^N$ and a numerical method to solve polynomial systems by deforming known solutions of start system to obtain the solutions to a target system.

A homotopy continuation method is a two-step method that consists of an *ab initio* solve of a start system and a *tracking* of the solution paths to approximate the solutions of a target system.

Consider a polynomial system $F(x) = 0$ with N equations and variables $x \in \mathbb{C}^N$,

$$F(x) = \begin{bmatrix} f_1(x_1, \dots, x_N) \\ \vdots \\ f_N(x_1, \dots, x_N) \end{bmatrix} = 0. \quad (2.1)$$

This system is our target system of which we do not know the solutions. To solve for this system by homotopy continuation, we can setup a similar system $G(x) = 0$ to which we know the solutions or can compute them easily and deform the system and its solutions to that of $F(x)$,

$$H(x, s) = sG(x) + (1 - s)F(x) \quad (2.2)$$

where $s \in \mathbb{R}$, $s \in (0, 1]$ is a path parameter starting at 1 and decreasing towards 0. This homotopy is called a *total degree homotopy*. A homotopy can be constructed where the converse is true, that s starts at 0 and increases towards 1, however starting s at 1 and approaching 0 allows for more digits of precision in the case that the target system admits singular solutions [18].

One will encounter difficulties when solving the system described in Eqn. 2.2 because s , which is on the real number line, will directly track through any singularity

that lies on the real number line in between 0 and 1. Instead, one employs what is known as the “gamma trick” to shift the path of s so that, with probability one, the new homotopy path is guaranteed to be smooth and singularity-free. We define a new path parameter,

$$q(t) = \frac{\gamma t}{\gamma t + (1 - t)} \quad (2.3)$$

where $\gamma \in \mathbb{C}$. Set $s = q(t)$ and substitute into Eqn. 2.2 to simplify to

$$H(x, t) = \gamma t G(x) + (1 - t) F(x). \quad (2.4)$$

Notice that $H(x, 0) \equiv \gamma G(x)$ and $H(x, 1) \equiv F(x)$. This trick holds for essentially any value of γ since the number of singularities of the system H is finite. For a deeper explanation of the gamma trick, the reader is encouraged to refer to [18, § 2.1.1].

It is imperative that the paths connecting the isolated solutions between our start and target systems be smooth maps from $(0, 1] \mapsto \mathbb{C}^N$. Additionally, every point along our homotopy path is a solution to our homotopy equation. Then, solving along these paths from our start system is equivalent to solving for the limit of the path as $t \rightarrow 0$, or solving the initial value Davidenko differential equation obtained by differentiating Eqn. 2.4 with respect to the path variable t .

$$\frac{\partial H}{\partial x} \frac{dx}{dt} + \frac{\partial H}{\partial t} = 0 \quad (2.5)$$

Numerically solving Eqn. 2.5 is done in a two step “predictor-corrector” method. The most basic of these methods is a first-order tracking method of an Euler prediction step, an extrapolation of the line tangent to the homotopy path at the current point, and a correction step that uses Newton iterations to sharpen the prediction to the actual solution on the homotopy path. The derivation of the two-step method is rooted in considering the first terms of a Taylor series about the point (x, t) [109].

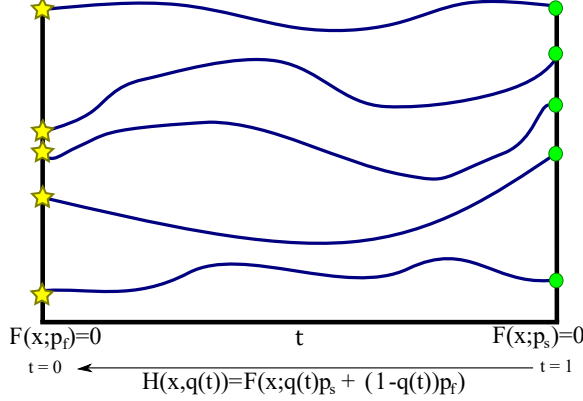


Figure 2.1. A successful parameter homotopy from start system $F(x; p_s)$ to target system $F(x; p_f)$.

The basic predictor and corrector equations are

$$y_{j+1} = y_j - J_x H(y_j, t_j)^{-1} \frac{\partial H(y_j, t_j)}{\partial t} \Delta t_j \quad (2.6a)$$

$$x_{j+1} = x_j - [J_x H(x_j, t_{j+1})]^{-1} H(x_j, t_j) \quad (2.6b)$$

where $\Delta t_j = t_{j+1} - t_j$, and y_j are the variable approximations at values $t_0 = 1 > t_1 > \dots > 0$. Equation 2.6b starts with an initial value of the Euler prediction, or $x_0 = y_{j+1}$.

This differential equation is not unique when the Jacobian of the system, $J_x H = \frac{\partial H}{\partial x}$, is not invertible in Eqn. 2.6b or equivalently $\text{rank}(J_x H) < N$.

Due to the guarantees of the gamma trick, there are no singular solutions lying on our homotopy path; however, the presence of singularities nearby the path can impact the numerical performance as the solution values become “near singular”. Near singular solutions are not guaranteed to converge to the homotopy path when we employ Newton’s Method, which requires an invertible Jacobian [71]. Homotopy solvers, such as **Bertini**, attempt to remedy this issue by taking a smaller prediction step before applying Newton iterations and by increasing computer precision as needed.

Additionally, **Bertini** provides options to use higher-order predictor methods, such as Runge-Kutta 4th order method, of which more information is provided in [18].

As these solution sets are algebraic, they can be manifolds and surfaces; the singularities deform the solution space and create poles in these spaces. One must use techniques such as the Cauchy integral for computations involving these poles [71]. This work will often use the term singularities or *branch points* in describing these solutions.

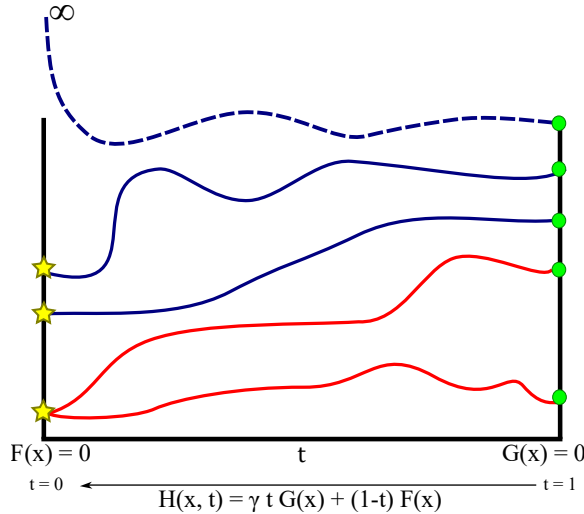


Figure 2.2. A homotopy from start system $G(x)$ to target system $F(x)$ with the red paths converging to an isolated singular point and the dashed path diverging off to a solution at infinity.

In total degree homotopies, we noted that not all homotopy paths track to finite isolated nonsingular solutions at the target system. We track this number of homotopy paths because a generic system admits a constant number of solutions, ignoring multiplicity of the solutions [122]. This number, an upper bound to the

number of generic solutions, is known as the Bézout number. It is computed based on the degree d of the system [121]. When the systems admit more structure, such as physically meaningful or real solutions, then the isolated nonsingular solutions may be less than the Bézout number. This is the consequence of homotopy paths diverging to infinity or meeting at singular solutions, as shown in Fig. 2.2. With some knowledge of variable groupings and the introduction of auxiliary variables to the system, one can reduce the homogeneous Bézout bound and the number of paths tracked. The tracking of infinite paths and singular solutions are rarely useful and imposes computational stress on homotopy solvers.

2.1.3 Parameter homotopies

For problems in kinematics, real target systems are often parameterized by physical characteristics such as link lengths or precision points. These constraints complicate directly solving the system. In such cases, one can instead compute solutions to a similar system with generic parameter coefficients and deform the parameters to that of the target system. When deforming the parameters, one tracks the respective deformation of the solutions, too. This method, shown in Fig. 2.1, is called a *parameter homotopy*.

Consider Eqn. 2.1 with analytic parameters $p \in \mathbb{C}^M$,

$$F(x; p) = \begin{bmatrix} f_1(x_1, \dots, x_N; p_1, \dots, p_M) \\ \vdots \\ f_N(x_1, \dots, x_N; p_1, \dots, p_M) \end{bmatrix} = 0. \quad (2.7)$$

This system represents a family of polynomial systems $F(x; p) = 0$ of which we can use parameter homotopies to compute solutions to other systems $F(x; p_f)$ where p_f is the set of the target parameters.

Similarly to a total degree homotopy, a parameter homotopy must first have an

ab initio solve of the start system system $F(x; p_s) = 0$ where p_s is the starting set of parameters. This is often the more computationally expensive step but need only to be done once. The next step applies the parameter homotopy $H(x, t) = F(x; q(t)p_s + (1 - q(t))p_f)$, $t \in (0, 1]$, with $q(t)$ defined in Eqn. 2.3, to compute the solutions to our target system $F(x; p_f) = 0$. Unlike the total degree homotopy, a parameter homotopy only tracks the number of solutions of the system, not the Bézout number of the system. The parameter homotopy is an attractive method such that the same *ab initio* starting system can be used as the basis for multiple parameter homotopies to a variety of parameter values.

2.1.4 Random monodromy loops

Monodromy is a group action applied to solution sets to “circle around” the parameter space to understand how solutions act.

The solutions to parameterized systems are algebraic sets that are subsets of a nonempty space in the Zariski topology which is smooth and connected. This allows us to define a loop parameterized by $\gamma(t) \in \mathbb{C}$, not to be confused with the γ present in the gamma trick, such that $\gamma(1) = \gamma(0) = p^*$ and apply monodromy action to the system $F(x; \gamma(t)) = 0$. This parameter set p^* is a projection of the *fiber* containing solutions to the system $F(x; p^*)$ [83]. This can also be modeled as system of three straight line homotopies with the solutions traveling to two intermediary systems defined by the generic parameter sets p_2 , p_3 before returning to the original start system defined by the parameter set p_1 .

$$H_1(x, t) = F(x; q(t)p_1 + (1 - q(t))p_2), \quad (2.8a)$$

$$H_2(x, t) = F(x; q(t)p_2 + (1 - q(t))p_3), \quad (2.8b)$$

$$H_3(x, t) = F(x; q(t)p_3 + (1 - q(t))p_1) \quad (2.8c)$$

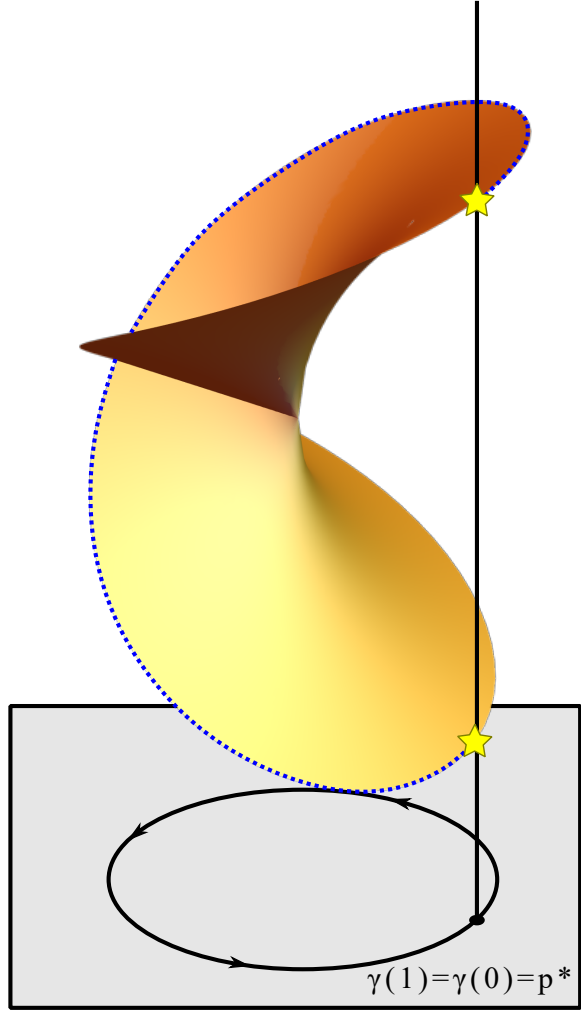


Figure 2.3. Graphical representation of the Riemann surface of $w = \sqrt{z}$. The monodromy loop follows the dashed path that starts at the parameters p^* , circles around the branch cut that when projected down is a closed loop, and returns to a new solution that lies on the fiber of which p^* is the projection in the parameter space.

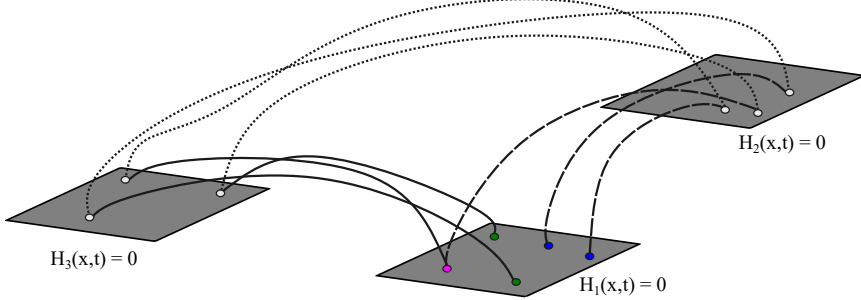


Figure 2.4. A visual representation of the RML described in Eqns. 2.8a, 2.8b, 2.8c and applied in Chapter 4. The starting points that were not returned to at the end of the RML are denoted in blue; the solution that is a member of both the start and end solution sets is denoted in pink; new solutions found by the RML are denoted in green.

With $t \in (0, 1]$.

When a random monodromy loop encloses a branch point in the parameter space, the paths return to the fiber often at different solution values, as shown in Figs. 2.3 and 2.4. These solutions are valid solutions and, if previously unknown, can be collected into the known solution set. While this method is not novel [7, 58, 60], it is a key method to numerical algebraic geometry. Iterative applications of random monodromy loops is a root-finding method that requires *a priori* knowledge of only one root to a system.

As with iterative methods, there needs to be a criteria for when to stop. A simple criteria is when the loops no longer track to unique solutions, but there are other means of validating solution set completeness [26, 59, 107]. For a test of sharp completeness, one can employ a *trace test* algorithm to the solution set. The linear trace test is an algebraic geometry method that computes completeness of a solution set by examining the intersection of the fiber of the parameter space's sliced along a fiber of the solution space [110]. Higher order trace tests rely on derivative values of the solution set [59]. In the case of extremely large problems with solution counts within the hundreds of thousands to even millions, a trace test would be computationally

impractical if even feasible. Instead, statistical models provide estimators and confidence intervals to the total count. These statistical models are inspired by biological “capture-mark-recapture” models to estimate wild population numbers, namely the Lincoln-Petersen, Chapman, and Schnabel models [33, 74, 77, 95].

2.2 Kinematics of Planar Mechanisms

These sections serve to illustrate the reader on concepts and mathematics that describe kinematic synthesis.

Mechanisms defined in this work are *planar*, meaning their movement is constrained to a two-dimensional plane. The simplest planar mechanism is a serial chain consisting of two links connected by two revolute (R) joints, commonly referred to as a 2R mechanism. One joint is fixed to the ground, denoted as a *pivot*, and the other joint connects the ground link to a second link with a end-effector, see Fig. 2.5.

Define \mathcal{M} to be the total freedom for a given body, which for a planar mechanism is 3, \mathcal{N} to be the number of bodies, or links, of a mechanism (including the ground link); \mathcal{J} the number of joints; and \mathcal{F}_j is the DoF for a joint j . For planar mechanisms, the number of degrees of freedom (DoF) are defined by Grübler’s formula [81].

$$\#DoF = \mathcal{M}(\mathcal{N} - 1 - \mathcal{J}) + \sum_{j=1}^{\mathcal{J}} \mathcal{F}_j, \quad (2.9)$$

A revolute joint admits 1-DoF.

Example 5. Consider the serial 2R mechanism in Fig. 2.5 consisting of $\mathcal{M} = 3$, $\mathcal{N} = 3$ links and $\mathcal{J} = 2$ revolute joints ($\mathcal{F}_j = 1$ for $j = 1, 2$). Then, by Grübler’s formula, the DoF of the 2R mechanism is

$$3(3 - 1 - 2) + 2 = 2.$$

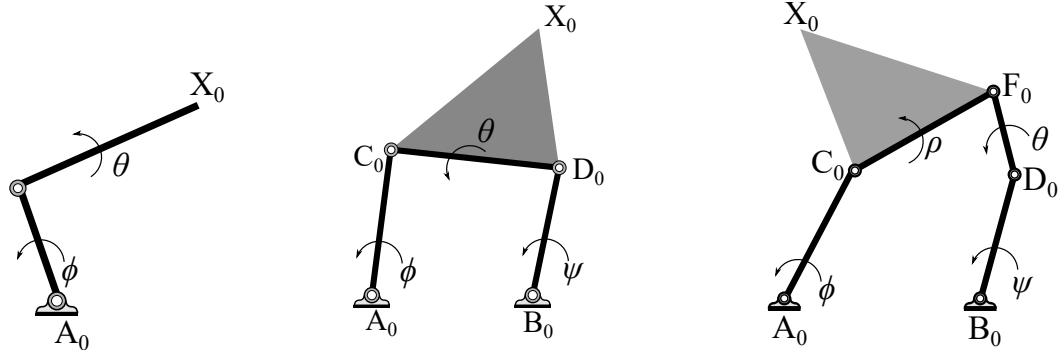


Figure 2.5. Three planar mechanisms of a serial 2R (left), four-bar (middle), and five-bar (right).

This mechanism is known as an *open-loop* or *serial chain* mechanism.

2.2.1 Isotropic coordinates

The use of isotropic coordinates with complex variables and parameters afford simpler mathematical descriptions over Cartesian coordinates in kinematic equations.

Consider a complex variable z ; its complex conjugate is denoted \bar{z} . However, complex conjugation is not algebraic, which is a requirement if our equations are polynomial. One can define an independent variable $z^* = \bar{z}$ and solve the system as usual. Then, within the total solution set, a real, physically meaningful solution exists when $z^* = \bar{z}$ [122]

We can define z in terms of its real and imaginary parts where $x, y \in \mathbb{R}$ and $i = \sqrt{-1}$ such that $z = x + yi$ and $\bar{z} = x - yi$. When we solve the system for all solutions, only those solutions where x, y are real will $\bar{z} = \text{conj}(z)$.

Regardless, one can always map between the two coordinate representations [122]. The transformation of real-valued Cartesian coordinates to isotropic is given by

$$z = x + yi, \quad \bar{z} = x - yi$$

Where x and y are real values and z is a complex value and \bar{z} is its conjugate. The map from isotropic to Cartesian is given by

$$x = \frac{z + \bar{z}}{2}, \quad y = \frac{z - \bar{z}}{2i}$$

Since a movement of a point within the complex plane can be considered a translation and rotation, we note that both operations are naturally defined isotropically. Define a rotation $Q = e^{\theta i}$ where θ is an angle in radians. Recall that a complex exponential can be defined in terms of cos and sin; this rotation operator is equivalent to an Euler rotation matrix about the z -axis (e.g. see [67]). Since rotation operators are of unit magnitude, scaling in the complex plane is achieved through the multiplication of a scalar. Then a full operation of scaling by a factor s and rotating by θ degrees in the complex plane is expressed as $se^{\theta i}$.

2.2.2 Four-bar mechanisms

A *four-bar mechanism* is a closed kinematic chain consisting of a 2R mechanism where the end point is constrained by another leg. The fourth bar is the leg connecting the two ground pivots.

Remark 6. One can verify via Grübler's formula for $\mathcal{M} = 3$, $\mathcal{N} = \mathcal{J} = 4$, $\mathcal{F}_j = 1$ for $j = 1, 2, 3, 4$ that a four-bar mechanism is a 1-DoF mechanism.

A valid four-bar mechanism has the condition that any link length cannot be greater than the sum of the other three link lengths. Grashof's condition [49] states that a four-bar with link lengths $\ell = \{l_1, l_2, l_3, l_4\}$, l_4 being the ground link, will have a complete 360° rotation of the link leg about the actuated pivot if the following holds

$$\max(\ell) + \min(\ell) < \text{sum of the other two link lengths.}$$

This pivot is then called the *crank* of the mechanism. A mechanism where the linkage does not complete the full rotation about the pivot but rather oscillates is known as a *rocker*. Four-bar mechanisms can be defined as *crank-rockers*, *double-cranks*, or *double-rockers*. For more information on four-bar mechanism geometry and classifications, refer to [47, 81].

Consider the four-bar mechanism in Fig 2.5 where we call the isotropic dimensions $\{A_0, B_0, C_0, D_0, X_0\}$ the “home configuration”. One can easily observe that summing the vectors starting at either ground pivot, looping about the chain, will sum to zero. We derive systems to describe the movement and orientation of these mechanisms from their *kinematic loop* equations.

2.2.2.1 Kinematic loop equations

Figure 2.5 is an arbitrary initial configuration of a four-bar mechanism, and the angles ϕ , ψ , and θ measure the displacement of the mechanism from that initial configuration [96]. The mechanism exhibits motion from from motors placed at either ground pivot to actuate the joint and rotate the leg to a given angle measurement, known as the *input angle* of the mechanism. The angle of the passive link moved by the rotation of the actuated joint is known as the *output angle*. With the angular displacements, the loop equation now becomes

$$A_0 + R_\phi(C_0 - A_0) + R_\theta(D_0 - C_0) = B_0 + R_\psi(D_0 - B_0), \quad (2.10)$$

where $R_\phi = e^{\phi i}$, $R_\psi = e^{\psi i}$, $R_\theta = e^{\theta i}$.

Since these dimensions are defined isotropically, their complex conjugate expressions must hold [123].

Notice the position of the *coupler point* X_0 can be described starting from either ground pivot. Points defined within the workspace which the mechanism is con-

strained to pass through are known as *precision points*, or equivalently in Chapter 4 as *design positions*. For a given precision point X_j , the loop equations are

$$A_0 + R_\phi(C_0 - A_0) + R_\theta(X_0 - C_0) = X_j \quad (2.11a)$$

$$B_0 + R_\psi(D_0 - B_0) + R_\theta(X_0 - D_0) = X_j \quad (2.11b)$$

A precision point X_j admits at most two nonsingular configuration solutions of the mechanism, often referred to “leg up” or “leg down” configurations [96]. These kinematic equations are very important in deriving systems of kinematic movement, namely forward kinematics where the joint locations and angles are known; inverse kinematics where the coupler point location is known but the joint locations and angles are unknown; and path and motion synthesis where precision points and/or configurations are pre-specified constraints the mechanism must obey [81].

Appendix A provides the derivation of the four-bar kinematic loop algorithms from Eqns. 2.10, 2.11a, and 2.11b; other ways to set up these equations to derive the necessary systems for the problem can be referenced in [6, 81, 96].

2.2.2.2 Configuration space and singularities

The configuration space of a four-bar mechanism is a one-dimensional algebraic curve [81]. Regardless of the four-bar’s classification, for the input angles $\phi \in [0, 2\pi]$, the coupler point X of the mechanism traces an algebraic curve within the plane, known as the *coupler curve*. The coupler curve is a real-valued *tri-circular sextic*, meaning it is of degree six and circularity of three.

Remark 7. The circularity of a curve refers to the multiplicity at which it passes through the “circular points at infinity” in the projective plane given by

$(X, Y, W) = (1, \pm i, 0)$, the two roots of $X^2 + Y^2 = 0$. For a tri-circular sextic curve of Cartesian variables (X, Y) , this is shown by the appearance of $(X^2 + Y^2)^3$ within

the curve expression [122, 123].

A valid coupler curve admits at most three self-intersections at least one of which must be real. Since a four-bar admits a “leg up” and “leg down” configuration, the coupler curve consists of two *circuits*, or the complete collection of orientations without any joint disconnection [75], for the two configuration options. A curve admits a *circuit defect* when the mechanism’s configurations belong to a disjoint input angle domain. A *branch* on a circuit is the continuous positions of a mechanism between two configurations. Bifurcations of the circuit arise when the mechanism faces a cross-roads in continuing its configuration movements [81] and gives rise to *branch defects*. Equivalently, a branch defect can be thought of as when the mechanism’s configurations are not of the same mode assembly, meaning that the mechanism must be reassembled to continue along the branch [19]. Generating mechanism designs that are circuit and branch defect-free as well as methods to detect and rectify defects are active research areas [5]. Mechanisms tracing coupler curves with defects admit no real world implementation. However, one can always consider another design to trace the same curve because coupler curves are an invariant to a group of mechanism designs known as *Roberts’ cognates*.

For one given coupler curve, there are 3 unique but geometrically related mechanism designs that trace the same curve [100]. This family of designs identified by its coupler curve is known as *Roberts’ cognates*. In the case one can invoke symmetry between the ground pivots [6], the number of mechanisms to a Roberts’ cognate group is doubled to six..

During the tracing of the coupler curve, we are interested that the four-bar does not encounter a singular configuration. Singular configurations result in a DoF loss to the mechanism and occur at configurations where the joints are collinear and the system’s Jacobian is not full rank. At these configurations, one inspects the velocity ellipse of the end effector, or coupler point, of the four-bar mechanism. The

ellipse's axes describe the *transmission qualities* of the mechanism. A four-bar in a singular configuration has a collapsed velocity ellipse; it cannot generate velocities in certain directions. The mechanism is “locked” due to the loss of freedom. For more information on four-bar velocity and dynamics, please refer to [7, 8, 81]

2.2.3 Five-bar mechanisms

Closed chain mechanisms with a greater number of legs greater have mathematical behavior that builds upon the concepts of four-bar mechanisms [103]. Often these n -bar mechanisms consist of four-bar sub-mechanisms, including the cases of six, eight, and ten-bar mechanisms. As one increases the number of linkages within the mechanism, the forces and velocity exerted and sustained on the mechanism's joints becomes of interest especially at prescribed points within the configuration space.

Five-bar mechanisms show the rapid increase in mathematical complexity when one adds just one extra link to a four-bar. A five-bar is a 2-DoF mechanism, meaning its coupler point can achieve a position at any point (x, y) within the workspace. In fact, each point within the five-bar workspace admits up to 4 configurations with different transmission qualities.

Remark 8. Grübler's formula with $\mathcal{M} = 3$, $\mathcal{N} = \mathcal{J} = 5$, $\mathcal{F}_j = 1$ for $j = 1, 2, 3, 4, 5$ verifies that a five-bar mechanism is a 2-DoF mechanism.

2.2.3.1 Kinematic loop equations

Consider the five-bar mechanism in Fig 2.5 shown in its home configuration with a loop equation

$$A_0 + R_\phi(C_0 - A_0) + R_\rho(F_0 - C_0) = B_0 + R_\phi(D_0 - B_0) + R_\theta(F_0 - D_0) \quad (2.12)$$

where $R_\phi = e^{\phi i}$, $R_\psi = e^{\psi i}$, $R_\theta = e^{\theta i}$, and $R_\rho = e^{\rho i}$.

Similarly the coupler point equations for a five-bar are

$$A_0 + R_\phi(C_0 - A_0) + R_\rho(X_0 - C_0) = X \quad (2.13a)$$

$$B_0 + R_\psi(D_0 - B_0) + R_\theta(F_0 - D_0) + R_\rho(X_0 - F_0) = X \quad (2.13b)$$

2.2.3.2 Configuration space and singularities

Configuration spaces of higher dimensional mechanisms are often manifolds of the same dimension as the DoF of the mechanism [46]. It is key to understand and visualize the configuration space when there are the presence of boundaries that impact the connectedness of the space, see Fig. 5.1. Path planning algorithms are limited by the *resolution*, discretization, of the configuration space [81]. Meaning a poor mathematical description that does not provide a sufficient representation of the configuration space and its bounds will have the appearance of erroneous connected components and diminished or presumably no possible mechanism movement between configurations.

In five-bar mechanisms, the bounds of the configuration space are defined by circular arc segments and four-bar coupler curves. Singularities to a five-bar mechanism occur when the middle joints C_0, D_0, F_0 are collinear. At these configurations the five-bar loses a DoF and collapses into a four-bar mechanism [81]. Recall that singular configurations result in a loss of a DoF for a mechanism. So a 2-DoF five-bar will act like a 1-DoF four-bar at singular configurations. A four-bar mechanisms configuration space is a one-dimensional algebraic curve, hence why the configuration bounds of five-bar mechanism are based in four-bar coupler curves.

A five-bar's end effector admits a velocity ellipse that relates the forces and their directions exerted by the five-bar. Understanding these dynamics of the mechanism stems from considering the first derivatives of Eqns. 2.12, 2.13a, and 2.13b.

CHAPTER 3

DISTRIBUTION OF HOMOTOPY BRANCH POINTS

Homotopy continuation is a standard method used in numerical algebraic geometry for solving multivariate systems of polynomial equations. Techniques such as the so-called gamma trick yield trackable homotopies with probability one. However, since numerical algebraic geometry employs numerical path tracking methods, being close to a branch point may cause concern with finite precision computations. This work is the first in a systematic study of branch points of homotopies to elucidate how branch points are distributed and use this information to study the probability of failure when using finite precision. Several examples, including a system arising in kinematics, with various start systems are included to demonstrate the theoretical analysis.

3.1 Introduction

Homotopy continuation is a method that has been used to solve many problems in mathematics, science, and engineering. By starting with a known solution set to a given system of equations $G = 0$, one can use homotopy continuation to deform from system G to a target system F to find the solutions of $F = 0$ [2, 88]. In this chapter, we consider multivariate polynomial systems over the complex numbers, in which case G can be chosen to guarantee, with probability one, that all isolated solutions of F will be found by tracking solution paths starting at the solutions of $G = 0$. The techniques of numerical algebraic geometry generalize this functionality to find all solution sets regardless of their dimension [109]. To be more precise, success with “probability one” means that certain parameters can be chosen generically in a

nonempty Zariski-open set in which the solution paths exist and are nonsingular. The working assumption in practice is that making the choice of these parameters using a pseudo-random number generator is equivalent to choosing them generically. While this is a well-justified assumption, the fact remains that these paths must be tracked numerically and may pass near branch point singularities. Hence, the number of branch points and their distribution impact the probability of failure in a numerical implementation.

Let U be \mathbb{C}^N or a compactification thereof, such as a product of projective spaces. Our objective is to numerically solve the polynomial system $F(u) : U \rightarrow \mathbb{C}^N$ starting from a polynomial system $G(u) : U \rightarrow \mathbb{C}^N$ and its isolated solutions by tracking the solution paths of the homotopy

$$H(u, t) = \gamma t G(u) + (1 - t) F(u), \quad t \in (0, 1] \subset \mathbb{R} \quad (3.1)$$

where $\gamma = e^{\theta i}$ in which the angle θ is chosen uniformly on $[-\pi, \pi]$ and $i = \sqrt{-1}$. When U is a product of projective spaces, u is a set of homogeneous coordinates and one may choose to work on a randomly selected coordinate patch [85] or adaptively switch patches as a path is tracked [57]. Our convention is to start at $t = 1$ and end at $t = 0$, which is convenient in cases where a singular endgame is invoked as $t \rightarrow 0$. As we will be studying in detail, the inclusion of the random number γ , sometimes called the “gamma trick,” allows the homotopy path to avoid branch point singularities with probability one. For each $t \in \mathbb{C}$, define $V(H(\cdot, t)) := \{u \in U \mid H(u, t) = 0\}$. To be more precise, for a properly defined homotopy, there are a finite number of $t \in \mathbb{C}$ where the Jacobian matrix $\frac{\partial H}{\partial u}(u, t)$ loses rank for some $u \in V(H(\cdot, t))$. By choosing θ at random, one in effect moves these branch points so that the probability of the corresponding ramification points lying on $(0, 1]$ becomes zero. Nevertheless, there is no guarantee about how close to this segment some may fall. If one is too close to this

segment, the ill-conditioning of the Jacobian in its neighborhood may cause a path tracker implemented in finite-precision floating point arithmetic to fail. The focus of this chapter is to examine how the branch points of several classes of polynomial systems are distributed and use this information to study how the probability of failure behaves in finite precision.

Equation (3.1) implicitly defines solution paths. One approach to computing them numerically is to choose a coordinate patch on U , say $u = u(q)$, for $q \in \mathbb{C}^N$, and then differentiate (3.1) with respect to t to obtain the Davidenko differential equation:

$$H_u \cdot \frac{\partial u}{\partial q} \cdot \frac{dq}{dt} + H_t = 0, \quad \text{where} \quad H_u = \frac{\partial H}{\partial u} \quad \text{and} \quad H_t = \frac{\partial H}{\partial t}. \quad (3.2)$$

For example, if u is a set of $N + 1$ homogeneous coordinates on \mathbb{P}^N , one may choose a patch $u = Aq$ where $A \in \mathbb{C}^{(N+1) \times N}$ is a full-rank matrix satisfying $\text{rank}(H_u A) = \text{rank}(H_u)$. This will be true for a nonempty Zariski-open subset of $\mathbb{C}^{(N+1) \times N}$, so a random choice will suffice with probability one [85]. However, one may improve numerical conditioning by adaptively switching patches as a path is tracked [57]. Similar constructions work when U is a product of projective spaces with an adjustment in the number of rows in A .

Starting from any initial solution u_0 such that $H(u_0, 1) = \gamma G(u_0) = 0$, standard numerical methods for solving differential equations allow one to move monotonically in t from 1 towards 0 along paths that are uniquely defined as long as H_u is nonsingular. For example, on the patch $u = Aq$, one may use a forward Euler predictor with step size $\Delta t < 0$, namely

$$u_{j+1} = u_j - [H_u(u_j, t_j)A]^{-1}H_t(u_j, t_j)\Delta t, \quad t_{j+1} = t_j + \Delta t$$

to move along t and, after incrementing $j \leftarrow j + 1$, correct the prediction using one

or more iterations of Newton's method,

$$u_j \leftarrow u_j - [H_u(u_j, t_j)A]^{-1}H(u_j, t_j)$$

to move (u_j, t_j) closer to the exact solution path. Although higher-order prediction methods are utilized in practice, such as Runge-Kutta methods [17] and Padé approximations [113], this does not change the gist of the discussion here. If the prediction is close enough and $H_u A$ is well-conditioned, the correction steps converge quadratically to the exact path. However, when H_u is ill-conditioned, the accuracy of the prediction decreases and may step outside the convergence zone for Newton's method. Even if the prediction is in the theoretical convergence zone, convergence of Newton's method may be lost if the digits of precision used are not enough to overcome ill-conditioning.

Failure near a branch point can happen in several ways, depending in part on how path tracking is implemented. One common failure mode is path crossing, due to the fact that branch points arise where solution paths cross. As t passes near a branch point, it may happen that the prediction lands within the convergence zone of another nearby path, ultimately causing the algorithm to omit from its list of solutions the endpoint of the original path. Alternatively, an implementation may include safeguards to prevent path crossing by adaptively taking smaller step sizes when it detects that the Jacobian is near-singular and halting if progress becomes too slow. Finally, as already mentioned, convergence of the corrector requires that enough digits of precision are used. In principal, as long as γ has been chosen such that there are no branch points for $t \in (0, 1]$, some combination of small enough step size in t with large enough precision will advance the path tracker past any close encounters with branch points and allow the path tracker to complete successfully. Failure occurs if this requires more resource in time or precision than have been

allocated.

An early experience motivating our interest in these matters was solving the nine-point path synthesis problem in [124]. Over thirty years ago, suspicious paths were recomputed in quadruple precision and symmetry checks were employed to assure a complete solution list. After the development of a path tracker with adaptive precision [14], the problem was revisited in [15] where it was found that 0.83% of paths required more than double precision for reliable tracking. The formulation used consists of 4 quadric and 8 quartic polynomials with a 2-homogeneous Bézout number (root count) of 286,720, which is the number of paths in the homotopy. Experience with many such systems shows that higher degrees and larger Bézout numbers tend to require higher precision, which leads us presently to investigate more deeply how these are related. Figure 3.1 illustrates the relationship between the condition number and presence of branch points. As suggested by this image, the need for higher precision based on ill-conditioning is associated with the presence of branch points. Therefore, we investigate here the number and distribution of branch points.

Previous work has addressed the influence of branch points on the path through adaptive strategies to improve efforts in homotopy step-size and precision [14, 113, 114], scaling coefficients with the SCLGEN algorithm [86], and Jacobian scaling [35, 57]. Certified path tracking methods take adaptivity a step further, using either alpha-theory or techniques from interval arithmetic to guarantee that the numerical approximations never leave the zone of convergence of the original path [20, 56, 70]. Although these aforementioned methods do not change the actual path tracked, monodromy techniques can be used to alter a homotopy path to circle around branch points before resuming along the original path [11]. These methods only provide a local look at the branch points near a given homotopy path and do not consider the location of branch points with regards to all possible homotopy paths.

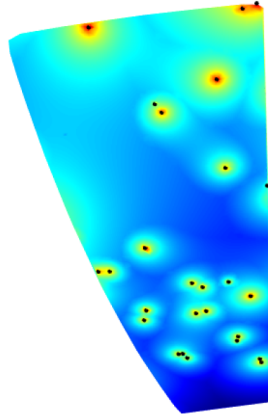


Figure 3.1. Illustrating on a small region the logarithm of the maximum condition number for each solution in relationship to the location of the ramification points (black). Proximity to ramification points increases the maximum condition number in the surrounding space resulting in “hot spots.”

For a single run of a homotopy, only the branch points close to the homotopy path matter. The novel aspect of this article is a global view of branch points. In particular, this article considers the distribution of all the branch points and studies how this impacts the probability of success or failure in tracking all the paths of the homotopy.

The rest of the chapter is organized as follows. Section 3.2 presents the mathematical formulations for defining a homotopy in projective space, mapping to the Riemann sphere, and visualization. Section 3.3 discusses how to compute branch points. Section 3.4 evaluates the distance from a branch point to a homotopy path and proposes a model of path tracking failure and endgame failure based on the closest corresponding ramification point. Section 3.5 provides examples of these analyses for quadratic systems in various number of variables and a four-bar path synthesis system. Finally, Section 3.6 summarizes our findings and presents an interesting question for further study.

3.2 Pencils, Branch Points, and Sphere Mappings

To aid in analysis and visualization, we reformulate homotopy (3.1) on projective space and apply a Riemann sphere mapping.

3.2.1 Projective space and pencils

While (3.1) is an appropriate formulation for running a single instance of a homotopy with $t \in (0, 1]$, to study the full set of possible homotopies for all possible choices of γ , it is more appropriate to recast the homotopy using projective space as

$$H(u, \tau) = H(u, [a, b]) = aG(u) + bF(u), \quad \tau = [a, b] \in \mathbb{P}^1. \quad (3.3)$$

When F and G are polynomial systems of the same class, H is said to be a *pencil* of that class.

Example 9 (N general quadrics with Bézout start system). To solve a system of N general quadrics in \mathbb{P}^N , one standard homotopy begins with start system G whose roots are roots of unity:

$$G(u) = \{g_1(u), \dots, g_N(u)\}, \quad g_j(u) = u_j^2 - u_0^2.$$

Let the target system $F(u)$ be a system of N general, complex quadrics in $N + 1$ variables. That is, $F(u) = \{f_1(u), \dots, f_N(u)\}$ where

$$f_i(u) = \underline{u} A_i \underline{u}^T, \quad \underline{u} = [u_0 \ u_1 \ \dots \ u_N] \in \mathbb{P}^N,$$

where each $A_i \in \mathbb{C}^{(N+1) \times (N+1)}$ is symmetric with general complex elements. For random instances, we choose each element in A_i uniformly within the box $[-1, 1] \times [-i, i] \subset \mathbb{C}$. Hence, with probability one, there are 2^N solutions in \mathbb{P}^N to both $G(u) =$

0 and $F(u) = 0$. The case with $N = 6$ will be the running example throughout.

3.2.2 Branch points

Let $\pi_\tau(u, \tau) = \tau$ be the natural projection of $U \times \mathbb{P}^1$ onto \mathbb{P}^1 . We assume that among the components of the algebraic set $V(h) := \{(u, \tau) \in U \times \mathbb{P}^1 \mid H(u, \tau) = 0\}$, there is a curve $X \subset U \times \mathbb{P}^1$ whose generic points have full rank, i.e., $\text{rank } H_u = N$, which implies that $\pi_\tau(X)$ is a D -sheeted cover of \mathbb{P}^1 for some $D \in \mathbb{Z}_{>0}$. This is the usual setup when H is a homotopy for solving system F by tracking D solution paths as $\tau \rightarrow [0, 1] \in \mathbb{P}^1$ along a continuous 1-dimensional real path $\gamma(t) \in \mathbb{P}^1$, $t \in [0, 1] \subset \mathbb{R}$. We call $\gamma(t)$ the *homotopy path* and $X \cap \pi_\tau^{-1}(\gamma(t))$ the set of *D solution paths*. Throughout this article, we assume that $\gamma(1) = [1, 0]$ and $\gamma(0) = [0, 1]$.

Let Z be the points in X where H_u drops rank. By our assumption regarding the generic nonsingularity of X , Z is a finite set. We may partition Z into three distinct subsets as

$$Z = Z_0 \sqcup Z_1 \sqcup Z_B, \quad \text{such that} \quad \pi_\tau(Z_0) = [0, 1], \quad \pi_\tau(Z_1) = [1, 0], \quad Z_B = Z \setminus (Z_0 \cup Z_1). \quad (3.4)$$

Accordingly, Z_0 is the singular set of $X \cap V(f)$, Z_1 is the singular set of $X \cap V(g)$, and Z_B are the *branch points* of X . Moreover, $B = \pi_\tau(Z_B)$ are the *ramification points* of X with respect to τ . In many cases, where H is a homotopy for solving F *ab initio* [18], G is a start system constructed to have no singularities, in which case $Z_1 = \emptyset$. For all homotopies considered here, the map $\pi_\tau : Z_B \rightarrow B$ is one-to-one, i.e., there is a unique branch point corresponding to each ramification point. The relationship between branch points and ramification points is studied in general in our companion paper [111]. Due to the one-to-one relationship and ease of viewing, we will plot ramification points. For example, Fig. 3.1 illustrates ramification points on a region in \mathbb{P}^1 as a proxy for branch points.

If the homotopy path passes through a ramification point, there are solution paths where the Davidenko differential equation (3.2) fails to define a unique solution path through the corresponding branch point. The singularities Z_0 and Z_1 present a different numerical problem since these correspond with endpoints and startpoints, respectively, of the solution paths. Since the value of τ is known *a priori* there, one may treat these using a local analysis based on the existence of a Puiseux series. A case where $Z_1 \neq \emptyset$ arises in polyhedral (a.k.a. BKK) homotopies [68, 119] where an analysis of the Newton polytopes of G provides the initial terms of the Puiseux series enabling the method to step off of $t = 1$. When $Z_0 \neq \emptyset$, that is, when F has singular solutions, endgame methods sample the solution paths in the vicinity of $t = 0$ to compute the endpoint value without needing to track all the way to the origin. These methods may approximate the initial terms of the Puiseux series directly [68, 92] or use the Cauchy integral theorem [91]. We will discuss endgames further in Section 3.4.3.

3.2.3 Riemann sphere

To help visualization, it is convenient to map $\tau = [a, b] \in \mathbb{P}^1$ to the Riemann sphere $(x, y, z) \in \mathbb{S}^2$, i.e., the unit sphere in \mathbb{R}^3 , using the following two charts:

$$b \neq 0 : \quad w = a/b, \quad (x, y, z) = (2\Re(w), 2\Im(w), 1 - ww^*)/(1 + ww^*), \quad (3.5)$$

$$a \neq 0 : \quad w = b/a, \quad (x, y, z) = (2\Re(w), -2\Im(w), ww^* - 1)/(1 + ww^*), \quad (3.6)$$

where $\Re(w)$ and $\Im(w)$ are the real and imaginary parts of w , respectively. One may confirm that these charts agree where they are both valid. Charts for mapping in the

inverse direction are

$$z \neq -1 : [a, b] = [x + yi, z + 1], \quad (3.7)$$

$$z \neq 1 : [a, b] = [1 - z, x - yi]. \quad (3.8)$$

These maps are bijective, so we may speak of a path in \mathbb{P}^1 and its image on the Riemann sphere as the same path, letting context determine which is applicable.

Substituting $[a, b] = [e^{\theta i} t, 1 - t]$ into both (3.5) and (3.6), one finds that the homotopy (3.1) follows a meridian—a great circle arc of constant longitude θ on the Riemann sphere—starting at $(0, 0, -1)$ corresponding with $t = 1$ and $\tau = [1, 0]$, and ending at $(0, 0, 1)$ corresponding with $t = 0$ and $\tau = [0, 1]$. We will refer to this great semicircle as the *homotopy path of longitude* θ .

The upshot of this reformulation of the problem is that the branch points of homotopy (3.3) are fixed and so are the ramification points in \mathbb{P}^1 and thereby on the Riemann sphere. Choosing θ at random picks the longitude of the arc that is tracked in executing the homotopy. Arcs that pass through a ramification point will result in a path-tracking failure, and in practical implementation, failures may also occur for near misses. Hence, the distribution of branch points, ramification points, and their distances to arcs of constant longitude become of vital interest.

In what follows, we will also refer to the latitude of branch points on the Riemann sphere. Measuring the angle in radians from $(x, y, z) = (0, 0, 1)$, the latitude is $\phi = \cos^{-1} z$.

3.2.4 Visualization of branch points

In Section 3.3 below, we will discuss how we compute branch points, but for the moment assume we already know them and we wish to visualize their distribution via the corresponding ramification points. For this purpose, we will use scatter plots,

heat maps, and histograms. The first step is to use (3.5) and (3.6) to map the ramification points to the unit sphere. Any single 2D image of this sphere shows only the forward facing hemisphere and has the drawback of exaggerating the apparent density of points near the boundary of that hemisphere. To overcome this, we make scatter plots of the points using polar coordinates using the following:

$$(r, \theta) = \begin{cases} (\sqrt{1+z}, \arctan2(-y, -x)), & z < 0, \\ (\sqrt{1-z}, \arctan2(y, x)), & z \geq 0, \end{cases} \quad (3.9)$$

where $\arctan2$ is the two-argument arctangent function. These maps produce two circular disks, one for each hemisphere divided by the equator, $z = 0$. We will present these by placing the map for $z \geq 0$ to the right and tangent to the one for $z < 0$, touching at the image of $(x, y, z) = (1, 0, 0)$. In this two-disk image, the great circle defined by $y = 0$, which represents real $[a, b]$, is a horizontal line segment. Its midpoint is the image of $(x, y, z) = (1, 0, 0)$ and both endpoints correspond to $(x, y, z) = (-1, 0, 0)$. The center of the left-hand disk corresponds to the start system G (i.e., $[a, b] = [1, 0]$) and the center of the right-hand disk corresponds to F (i.e., $[a, b] = [0, 1]$). Due to the area-preserving property of this map, even though distances are distorted near the perimeters of the disks, a uniform density of points on the sphere will produce a uniform density of points in these disks. Figure 3.2 shows the result for the homotopy constructed using $N = 6$ in Example 9, which has 1344 branch points and ramification points. Also shown in that figure is a heat map of ramification point density, wherein each pixel is colored according to how many ramification points are within a specified distance on the unit sphere. (In this paper, a distance of 0.08 rad is used throughout.) For larger N , where the number of branch points becomes large, a scatter plot of ramification points becomes too crowded and only the heat map is informative.

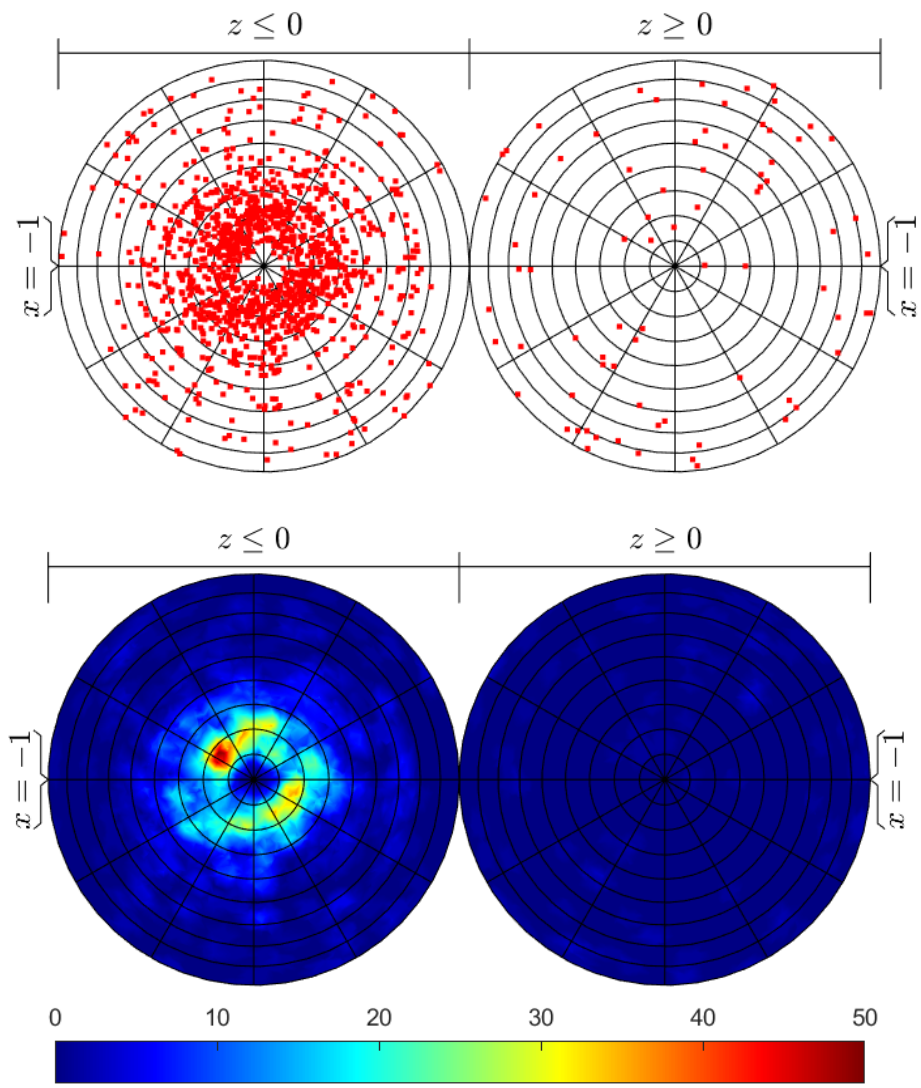


Figure 3.2. Ramification point scatter plot and heat map for $N = 6$ in Example 9.

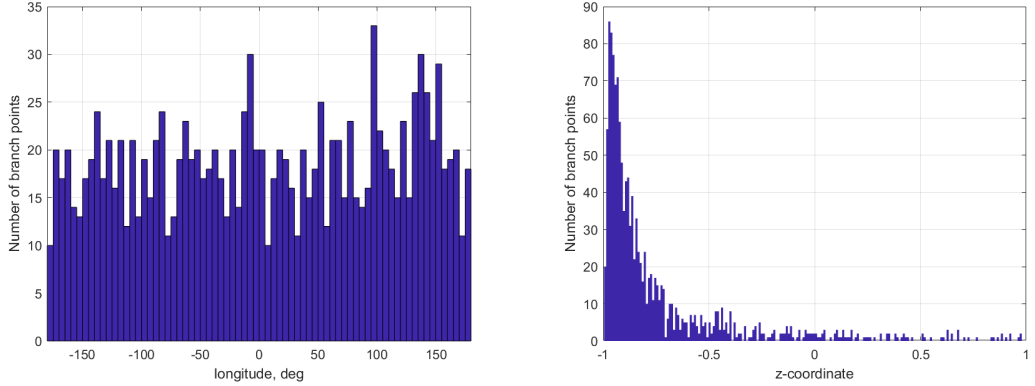


Figure 3.3. Histograms of longitude and z -coordinate for $N = 6$ in Example 9.

A third way to visualize the distribution of branch points is to plot histograms of longitude and z -coordinate of the ramification points. Dividing longitude into equal sectors divides the sphere into equal areas and the same is true for equal increments of the z -coordinate. Consequently, if the ramification points are uniformly distributed on the sphere, both these histograms will be flat within statistical variation. Figure 3.3 suggests uniformity with respect to longitude but not with respect to the z -coordinate for the running example.

We note that in this particular example, the ramification points are concentrated in a ring between 10° to 20° centered on $(0, 0, -1)$, which corresponds with the start system. Examples in Section 3.5 show a similar characteristic of the Bézout start system with a complete absence of branch points in a disk centered there, and an overconcentration of branch points just outside that disk.

3.3 Computing Branch Points

In order to employ the visualization techniques described in Section 3.2.4, one needs a method to compute the branch points. We begin by computing the set

$Z = X \cap V(\text{rank } H_u < N)$, and then we partition this into Z_0, Z_1, Z_B as in (3.4), with ramification points $B = \pi_\tau(Z_B)$. If $V(H)$ has solution components other than X , an intersection algorithm would be required to compute Z , but for the examples considered in this paper, the start system G is general enough that the only possible components of $V(H)$ other than X are singular components of the end point system, $H(u, 0) = F$. As for the right-hand element of the intersection, formulating algebraic conditions for the drop in rank of H_u in terms of determinants is inconvenient, particularly due to the possibly high degree. Instead, we may express the loss of rank condition as the existence of a null-space vector [16] either on the left or right. With these facts in mind, we can find the branch points by computing all isolated solutions of either

$$B_\ell(u, \tau, v) = \{H(u, \tau), v H_u(u, \tau)\} : U \times \mathbb{P}^1 \times \mathbb{P}^{N-1} \quad (3.10)$$

where v is a $1 \times N$ row of homogeneous coordinates, or as

$$B_r(u, \tau, v) = \left\{ H(u, \tau), \begin{bmatrix} H_u(u, \tau) \\ R \end{bmatrix} v \right\} : U \times \mathbb{P}^1 \times \mathbb{P}^{K-1} \quad (3.11)$$

where v is a column of K homogeneous coordinates, the number of which depends on how the compactification of U has been formulated. Matrix R is selected generically with the dimensions required to complete a square $K \times K$ matrix. If H_u is rank deficient, then so is this square matrix. Since the formulation of X ensures that there are a finite number of branch points, the right-null condition will intersect X transversely at these with probability one. However, the right-null condition allows extraneous roots where the rows of H_u are independent but R does not complete a full basis. For this reason, the right-null formulation requires a final filter that retains only the points where $\text{rank}(H_u) < N$, as can be checked numerically with a singular value decomposition. While the left-null formulation is more direct for computations,

the right-null formulation is useful for proving Theorems 10 and 12 below. In the particular case when $U = \mathbb{P}^N$ so u is a set of $K = N + 1$ homogeneous coordinates on \mathbb{P}^N , R is a generic $1 \times (N + 1)$ matrix and v lives on \mathbb{P}^N . When $U = \mathbb{P}^{N_1} \times \mathbb{P}^{N_2}$, u is a set of $K = N_1 + N_2 + 2$ coordinates, and it is sufficient to choose R generically of the form

$$R = \begin{bmatrix} R_1 & 0 \dots 0 \\ 0 \dots 0 & R_2 \end{bmatrix}$$

where R_k is a $1 \times (N_k + 1)$ row vector for $k = 1, 2$.

For each of the systems we treat below, we compute branch points using the *Bertini* software package [14, 18]. Since these computations themselves are numerical homotopies, path failures and path crossings are possible, which could mean that the resulting solution lists are incomplete. However, for the general complex pencils of Example 9, our computations yield exactly the number of branch points predicted by the following.

Theorem 10. *If H is a general pencil of N polynomials of degree $d \geq 2$ in \mathbb{P}^N , then there are at most $2\binom{N+1}{2}(d-1)d^{N-1}$ branch points. In particular, when $d = 2$, the number of solution paths for H is 2^N while the number of branch points is at most $\binom{N+1}{2}2^N$.*

Proof. First, the 3-homogeneous Bézout count for system B_r in (3.11) is the coefficient of $\alpha^N \beta \zeta^N$ in

$$(d\alpha + \beta)^N ((d-1)\alpha + \beta + \zeta)^N \zeta$$

which is $Nd^{N-1}((N+1)(d-1)+1)$. Of course, this also yields an upper bound on the number of branch points which would be sharp if B_r was generic with respect to the 3-homogeneous structure. However, B_r is structured and this bound accounts for both branch points as well as solutions resulting from Euler's homogeneous function theorem with $u = v$, i.e., $H(u, \tau) = 0$ implies $H_u(u, \tau)u = 0$. The 2-homogeneous

Bézout count for $\{H(u, \tau), Ru\}$, which is the coefficient of $\alpha^N \beta$ in $(d\alpha + \beta)^N \alpha$, is Nd^{N-1} . Due to genericity of H and R , this bound is sharp. Hence, the number of branch points is at most the difference of these two numbers, namely

$$Nd^{N-1}((N+1)(d-1)+1) - Nd^{N-1} = N(N+1)(d-1)d^{N-1} = 2 \binom{N+1}{2} (d-1)d^{N-1}.$$

Moreover, when $d = 2$, this becomes $2 \binom{N+1}{2} (2-1)2^{N-1} = \binom{N+1}{2} 2^N$. \square

Example 11. Section 3.2.4 considered $N = 6$ with $d = 2$ having 1344 branch points with Fig. 3.2 showing the 1344 ramification points. In this case, the bound from Theorem 10 is $\binom{6+1}{2} 2^6 = 1344$.

Theorem 12. *If H is a general pencil of $N_1 + N_2$ polynomials of bidegree (d_1, d_2) in $\mathbb{P}^{N_1} \times \mathbb{P}^{N_2}$, then there are at most*

$$2d_1^{N_1-1}d_2^{N_2-1} \binom{N_1+N_2}{N_1} \left(\binom{N_1+N_2+1}{2} d_1 d_2 - \binom{N_2+1}{2} d_1 - \binom{N_1+1}{2} d_2 \right)$$

branch points. In particular, when $d_1 = d_2 = 1$ and $N = N_1 = N_2$, the number of solution paths for H is $\binom{2N}{N}$ on $\mathbb{P}^N \times \mathbb{P}^N$ while the number of branch points is at most $2N^2 \binom{2N}{N}$.

Proof. This could be seen as a special case considered in our companion paper [111, § 3.1.2] where all polynomials in a multiprojective space have the same multidegree. On the other hand, this can be proved similarly to Theorem 10 as the multihomogeneous bound for the system minus counts of solutions resulting from Euler's homogeneous function theorem. In particular, the 4-homogeneous Bézout count corresponding with the coefficient of $\alpha_1^{N_1} \alpha_2^{N_2} \beta \zeta^{N_1+N_2}$ in

$$(d_1 \alpha_1 + d_2 \alpha_2 + \beta)^{N_1+N_2} ((d_1-1) \alpha_1 + d_2 \alpha_2 + \beta + \zeta)^{N_1} (d_1 \alpha_1 + (d_2-1) \alpha_2 + \beta + \zeta)^{N_2}$$

is

$$\binom{N_1 + N_2}{N_1} d_1^{N_1-1} d_2^{N_2-1} ((N_1 + N_2 + 1)(N_1 + N_2)d_1d_2 - N_2^2 d_1 - N_1^2 d_2). \quad (3.12)$$

In this case, one obtains two different types of solutions resulting from Euler's homogeneous function theorem, namely from \mathbb{P}^{N_1} and from \mathbb{P}^{N_2} . The coefficient of $\alpha_1^{N_1-1} \alpha_2^{N_2} \beta$ in $(d_1\alpha_1 + d_2\alpha_2 + \beta)^{N_1+N_2}$ is the count for \mathbb{P}^{N_1} , which is

$$\binom{N_1 + N_2}{N_1} N_1 d_1^{N_1-1} d_2^{N_2}. \quad (3.13)$$

Similarly, for \mathbb{P}^{N_2} , the count is

$$\binom{N_1 + N_2}{N_1} N_2 d_1^{N_1} d_2^{N_2-1}. \quad (3.14)$$

Thus, subtracting (3.13) and (3.14) from (3.12) yields

$$\begin{aligned} & \binom{N_1 + N_2}{N_1} d_1^{N_1-1} d_2^{N_2-1} ((N_1 + N_2 + 1)(N_1 + N_2)d_1d_2 - (N_2 + 1)N_2 d_1 \\ & \quad - (N_1 + 1)N_1 d_2) \end{aligned}$$

which is equivalent to the formula in the statement above. In particular, when $d_1 = d_2 = 1$ and $N_1 = N_2 = N$, this becomes

$$\binom{N + N}{N} ((N + N + 1)(N + N) - (N + 1)N - (N + 1)N) = \binom{2N}{N} (2N^2).$$

□

Example 13. For a bilinear system on $\mathbb{P}^3 \times \mathbb{P}^3$, the bound from Theorem 12 is $2 \cdot 3^2 \cdot \binom{2 \cdot 3}{3} = 360$.

A natural question is to determine the number of branch points for other types

of homotopies, such as when the polynomials are defined on multiprojective space with various multidegrees, which is considered in our companion paper [111]. In particular, results from [111] show that when the polynomials are general, then the exact theoretical predictions on the number of branch points in Theorems 10 and 12 are sharp. However, for particular systems, the exact number of branch points may not be known theoretically. If a few branch points have been missed in these cases, e.g., in Section 3.5.2, comparison to the general case shows that their number is small enough that it should have little impact on our analysis described in the next section.

3.4 Impact of Branch Points

After a choice of γ in (3.1), the path of $[a, b]$ in (3.3) when mapped to the Riemann sphere becomes a longitudinal meridian from south pole $(0, 0, -1)$ to north pole $(0, 0, 1)$. Numerical difficulties, or lack thereof, depend on how close this arc passes to a ramification point and on how widespread ill-conditioning is near the branch points. In this section, we present our approach to analyzing these issues given the set of branch points of a homotopy. We also consider what one may expect if the ramification points happen to be distributed uniformly on the Riemann sphere. Subsequently, Section 3.5 compares the results for specific examples with the expectations for a uniform distribution.

3.4.1 Distance to ramification points

Assume there are M branch points and an ordering assigned to the branch points and correspondingly to the ramification points. Suppose that the j^{th} ramification point is located at longitude θ_j and latitude ϕ_j . Then, the distance to the meridian

of longitude θ is $\delta_j \in [0, \pi/2]$ given by

$$\delta_j(\theta) = \begin{cases} \sin^{-1} (\sin \phi_j \sin |\theta - \theta_j|), & \text{if } |\theta - \theta_j| < \pi/2; \\ \phi_j, & \text{otherwise.} \end{cases} \quad (3.15)$$

In particular, $\delta_j(\theta)$ is nonnegative and is an even function of $(\theta - \theta_j)$ that is monotonic on intervals $[-\pi, 0]$ and $[0, \pi]$, and zero at $\theta - \theta_j = 0$. Moreover, the function is concave downward or constant everywhere except at its minimum point. For meridians close to the longitude of a ramification point, i.e., for small $(\theta - \theta_j)$, the first-order approximation to (3.15) is

$$\delta_j(\theta) \approx \sin \phi_j |\theta - \theta_j|, \quad |\theta - \theta_j| \ll 1. \quad (3.16)$$

Moreover, the periodic function

$$\delta_{\min}(\theta) = \min_{j=1, \dots, M} \delta_j(\theta) \quad (3.17)$$

touches zero at each $\theta = \theta_j$ and has a single maximum in each interval between adjacent values of θ_j . Figure 3.4 illustrates this on a small range of longitude. We will be especially interested in the range where (3.16) applies, which means that we have allocated enough digits of precision to enable solution paths to pass closely by branch points.

3.4.2 Probability of failure

We wish to investigate how the number of branch points and their distribution affects the probability of success in solving homotopy (3.1). In practice, this probability depends on many details, such as the scaling of F and G , how their evaluations are coded numerically, and implementation details of the path tracking algorithm.

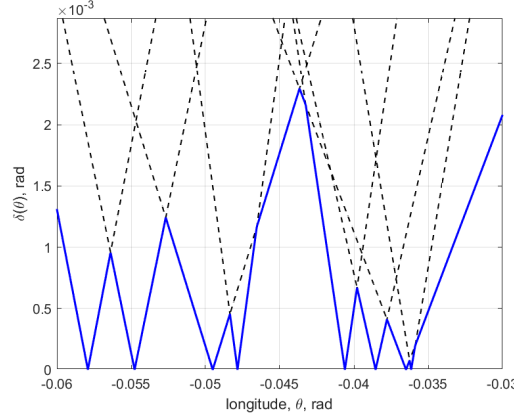


Figure 3.4. Detail of $\delta_j(\theta)$ and $\delta_{\min}(\theta)$ for $N = 6$ in Example 9. Here, several plots of $\delta_j(\theta)$ are shown as dashed V-shape centered at each longitude θ_j while $\delta_{\min}(\theta)$ is overlaid in solid blue.

The following definition is a severe simplification of the situation, but it captures the underlying cause of the most common mode of path-tracking failure. Let Z be the set of singular points of homotopy (3.3), which we partition into $Z = Z_0 \sqcup Z_1 \sqcup Z_B$ as in (3.4) using the projection $\pi_\tau(u, \tau) \mapsto \tau$.

Definition 14 (δ^* -Failure). Assume that there exists a $\delta^* > 0$ such that path tracking along one-real-dimensional path $\gamma \subset S$, where S is the unit Riemann sphere, succeeds on every solution path if and only if the distance between γ and the nearest singularity satisfies $\delta_{\min}(\theta) \geq \delta^*$. If $\delta_{\min}(\theta) < \delta^*$, the homotopy is said to experience δ^* -failure.

The δ^* -failure criterion is a proxy for failure due to ill-conditioning of the Jacobian matrix H_u . As $[a, b]$ in (3.3) approaches a branch point, the minimum singular value of H_u approaches 0 on at least one path. This induces a path-tracking failure when progress along the path requires the path tracker to exceed an upper limit set on the number of digits allowed in an adaptive-precision procedure or a lower limit on the forward progress in adaptive step size. Such limits are commonly set as hyperparameters, i.e., a parameter of the path-tracking algorithm, to prevent

excessive computation time on particularly difficult paths.

While δ^* -failure ignores some failure modes, it also sets a high bar for success in that we are declaring failure even if only one solution path among many fails.

Theorem 15. *Assume $H(u, \tau)$ has no rank deficient solutions at $\tau = [1, 0]$ or $\tau = [0, 1]$. Let $I_{<0}(x)$ be the indicator function that returns 1 if $x < 0$ and 0 otherwise. For θ uniformly distributed over $[-\pi, \pi]$, the probability of δ^* -failure is*

$$P_{\text{fail}}(\delta^*) = \frac{1}{2\pi} \int_{-\pi}^{\pi} I_{<0}(\delta_{\min}(\theta) - \delta^*) d\theta. \quad (3.18)$$

Moreover,

$$\frac{dP_{\text{fail}}}{d\delta^*}(0) = \frac{1}{\pi} \sum_{j=1}^M \frac{1}{\sin \phi_j} \quad (3.19)$$

Proof. Equation (3.18) is just expectation of the indicator for failure taken over a uniform distribution. The derivative at zero follows from the first-order approximation (3.16). \square

Equation (3.19) indicates that ramification points near the poles, i.e., those with smaller $\sin \phi_j$, are more deleterious than ones in the middle latitudes. That is because a point near a pole is close to a greater proportion of the meridians than a mid-latitude point.

For a given set of branch points, (3.18) together with (3.15) and (3.17) can be used to evaluate P_{fail} . This requires computing the branch points and determining the ramification points where different δ_j enter δ_{\min} . The approximation (3.19) is much simpler to apply and allows us to consider how δ^* -failure behaves when the ramification points follow a given probability distribution.

Corollary 16. *Suppose that M ramification points are distributed independently and uniformly over the Riemann sphere. Then, the expected initial slope of the δ^* -failure curve is $\mathbb{E} \left[\frac{dP_{\text{fail}}}{d\delta^*}(0) \right] = \frac{M}{2}$.*

Proof. The latitude ϕ of a point distributed uniformly on the sphere has a probability density function $pdf(\phi) = (\sin \phi)/2$ where $\phi \in [0, \pi]$. Using the initial slope of the failure curve from (3.19) in Theorem 15, one finds that its expectation is

$$\mathbb{E} \left[\frac{dP_{\text{fail}}}{d\delta^*}(0) \right] = \int_0^\pi \left(\frac{1}{\pi} \sum_{j=1}^M \frac{1}{\sin \phi_j} \frac{\sin \phi_j}{2} \right) d\phi = \frac{M}{2\pi} \int_0^\pi d\phi = \frac{M}{2}.$$

□

Naturally, a homotopy with more branch points and correspondingly more ramification points will have a higher probability of failure, but it is notable that the rate of increase is only linear in the total number M . Practical experience shows that homotopies with high total degree usually require the allocation of more digits of precision to achieve the same level of robustness as one observes for lower-degree homotopies. One explanatory factor for this observation is that high-degree homotopies tend to have more branch points as suggested by Theorems 10 and 12.

Since the slope given in Corollary 16 is just an expectation, samples of M randomly distributed points can have slopes different from this. Moreover, the actual distribution of ramification points in homotopies may have distributions far from uniform, as observed in Figs. 3.2 and 3.3.

It should be noted that the variance of the initial slope of P_{fail} is unbounded. This is attributable to the fact that a ramification point close to either pole makes an outsized contribution to the slope, with the contribution tending to infinity the closer it happens to land near a pole. Accordingly, under the assumption of uniform distribution, the average behavior is mild but outliers are expected.

Given a set of branch points and ramification points, we can compute $P_{\text{fail}}(\delta^*)$ from (3.18) and compare its limiting behavior to the prediction of a uniform distribution. For this purpose, it is useful to plot P_{fail} versus $\hat{\delta}^* = (M/2)\delta^*$ so that the expected slope for the uniform distribution is 1. This normalizes the plot when

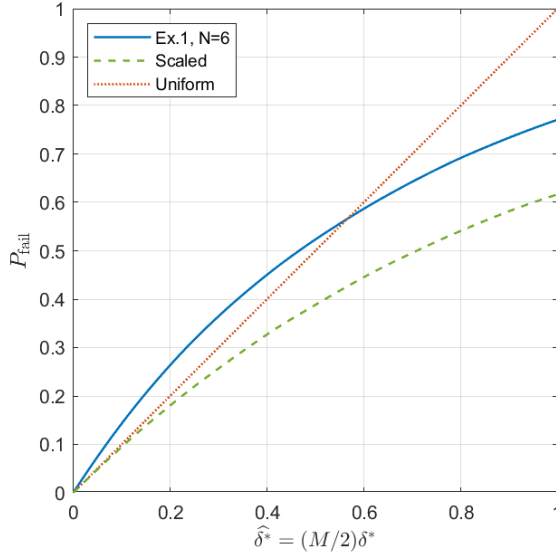


Figure 3.5. Probability of δ^* -failure, P_{fail} , versus normalized safe distance $\widehat{\delta}^*$ for Example 9 and its rescaled counterpart from Section 3.4.4. The diagonal line shows the slope expected from a uniform distribution of branch points.

we consider problems with a different number of branch points. The result for our running example is shown in Fig. 3.5, where we see that the actual distribution of the ramification points gives a steeper slope at the origin than expected from a uniform distribution. The actual slope is approximately 1305 compared to 672 expected for a uniform distribution. This is due to the fact that the ramification points for this example are concentrated in a ring near $z = -1$ as observed in Fig. 3.2. Even though the actual slope is higher than the uniform expectation, we see that they are of approximately the same order of magnitude.

Section 3.4.5 relates the distance to branch points and conditioning of the Jacobian, which in turn governs how close we may successfully pass by a branch point. For the moment, let us suppose that we have allocated enough digits of precision so that $\delta^* \approx 10^{-6}$, a reasonable number when working in double precision. Under that assumption, we see that the probability of δ^* -failure computed using Theorem 15 on the running example is quite low, only $1.3 \cdot 10^{-3}$. Of course, this can be made even

lower by using higher precision.

3.4.3 Endgame failure

It commonly happens that some of the solution paths of homotopy (3.3) end at singularities when $F(u)$ has a more special structure than the start system $G(u)$. To compute the endpoint singularities, one may employ a singular endgame, e.g., [69, 91, 92]. For any of these endgames to work reliably, τ must be close enough to $[0, 1]$ to enter the endgame operating zone [92, 109], whose outer radius is governed by the ramification point closest to $[0, 1]$. However, the endgame operating zone also has an inner void due to ill-conditioning near the singularity at $[0, 1]$. If too few digits of precision are used in computations, the inner void may be so large that the endgame operating zone is empty, that is, the endgame will fail.

To be more precise, we will limit our discussion to the “Cauchy endgame” of [91], although the behavior of endgames based on a fractional power series (i.e., Puiseux series) is similar. By the theory described in [91], the topology of curve X in the neighborhood of a singularity in Z_0 is a punctured disk, which can be described as follows. Let $\Gamma(\xi) = [\sin \phi e^{2\pi i \xi}, \cos \phi] \in \mathbb{P}^1$, $\phi < \pi$, $\xi \in [0, 1] \subset \mathbb{R}$, which maps to a circle of constant latitude ϕ on the unit Riemann sphere. Define the interior $\widehat{\Gamma}$ of Γ to be the cap of the sphere that contains $(0, 0, 1)$. Let $P = X \cap \pi_\tau^{-1}(\Gamma(0))$ be a set of points connected by monodromy in X around $\Gamma(\xi)$ and let $\#P$ denote the number of points in P . If $\widehat{\Gamma}$ does not contain a ramification point for X , then continuation in X from P along any path in $\widehat{\Gamma} \setminus \{[0, 1]\}$ is well-defined up to monodromy around $\tau = [0, 1] \in \mathbb{P}^1$, and the set of all such points with the usual topology in \mathbb{C} is topologically equivalent to a punctured disk. Moreover, there is a unique point, say P_0 , that completes the closure of the disk. Each coordinate of P_0 is given by a Cauchy integral circling $\#P$ times around $\Gamma(t)$. The computation of P_0 via such an integral is known as the “Cauchy endgame,” and $\#P$ is called the “winding number” or “cycle

number” of the endpoint. Of course, the path of the Cauchy integral does not have to be a circle, but sampling at equal intervals around a circle of constant latitude leads to a simple calculation since the trapezoidal rule for integration nets out to the average of the samples. As explained in [116], this approach has particularly nice computational properties. The endgame applies to both singular and nonsingular endpoints, but it is not usually deployed for nonsingular endpoints since they can be computed by path tracking all the way to $\tau = [0, 1]$.

By the construction above, each singular endpoint of the homotopy has an associated local disk that extends outward until the first branch point is encountered at the outer radius of convergence of the endgame. Call this the singularity’s local branch point (or possibly, branch points) and the corresponding ramification point the singularity’s local ramification point(s). For the endgame to succeed, the path of the Cauchy integral must stay close enough to the singularity to pass between it and the local ramification point(s), but path tracking near the singularity may fail if too few digits of precision are used. The following aims to capture this phenomenon.

Definition 17 (Endgame δ^+ -Failure). For a given working precision near a singular endpoint, there exists a $\delta^+ > 0$ such that path tracking fails for monodromy along a circle of constant latitude $\phi < \delta^+$. We say that the Cauchy endgame executed at latitude $\phi < \delta^+$ for a singular endpoint experiences δ^+ -failure.

Theorem 18. *Suppose that the radius of convergence for a singular endpoint is ϕ^* , and path tracking is subject to δ^* -failure near ramification points and δ^+ failure near the singularity. Then, the Cauchy endgame must fail if $\phi^* < \delta^* + \delta^+$.*

Proof. To succeed, the path of the Cauchy integral must pass between the ramification point at latitude ϕ^* and the singularity at latitude 0, staying δ^* from the former and δ^+ from the latter. If $\phi^* < \delta^* + \delta^+$, these forbidden zones overlap. \square

When $\phi^* > \delta^* + \delta^+$, the Cauchy endgame has an annular endgame operating

zone extending from latitude δ^+ to $\phi^* - \delta^*$. When the operating zone is narrow, the Cauchy endgame procedure may have trouble finding a latitude where it succeeds. In practice, the endgame is executed without knowledge of ϕ^* , so success is judged by computing the integral at several different latitudes, for example, at ϕ and at $\alpha\phi$ for $\alpha > 1$ which are both inside the operating zone. A criterion for success is that the convergence rate of the approximation has the expected dependence on ϕ . In such an approach, the procedure needs $\phi^* > \delta^* + \alpha\delta^+$.

The preceding discussion has concentrated on endpoint singularities and the endgame, but in general there could also be singularities at the start of the homotopy. In many applications, this is not an issue since the start system G is constructed to have all nonsingular roots. However, the start system for polyhedral (a.k.a. BKK) homotopies [68, 119] does begin with singularities, and initiation of path tracking from $\tau = [1, 0]$ depends on the convergence of a fractional power series there. To handle such cases, one may make the obvious adjustments to our discussion here, considering monodromy loops around $[1, 0]$ instead of around $[0, 1]$, and so on.

To analyze the endgame operating zone in detail, one would need to determine the local branch point and corresponding ramification point for each singularity. Lacking this knowledge, we can still say that if all ramification points are farther than $\phi_{\text{crit}} := \delta^* + \delta^+$ from $\tau = [0, 1]$, then the endgame will succeed on every endpoint. To get an idea of how probable this desirable outcome is, we consider the case where the ramification points are uniformly distributed on the sphere.

Proposition 19. *The cumulative distribution function (CDF) and the probability density function (PDF) associated with the minimum latitude of M points distributed*

independently and uniformly on the unit sphere are

$$cdf(\phi_{\min}) = 1 - 2^{-M} (1 + \cos \phi_{\min})^M, \quad pdf(\phi_{\min}) = \frac{M}{2^M} (1 + \cos \phi)^{M-1} \sin \phi, \quad (3.20)$$

$$\phi \in [0, \pi],$$

while the maximum likelihood value (MLE) is

$$mle(\phi_{\min}) = \arctan 2(\sqrt{2M-1}, M-1) \approx \sqrt{2/M}, \quad M \gg 1. \quad (3.21)$$

Proof. The z -coordinates of the M points are distributed independently and uniformly on $[-1, 1]$. Latitude $\phi = \cos^{-1} z$ is monotonic on $[-1, 1]$, so the point of minimum ϕ is the point of maximum z . Thus, order statistics, e.g., see [120, § 6.7], followed by a transformation yields (3.20). Equation (3.21) derives from setting the derivative of the pdf in (3.20) to zero and solving. \square

Corollary 20. *For large M and small ϕ_{crit} with $M\phi_{\text{crit}}^2 \ll 1$, the probability that the minimum latitude is less than ϕ_{crit} is*

$$P(\phi_{\min} \leq \phi_{\text{crit}}) = cdf(\phi_{\min}) \approx M\phi_{\text{crit}}^2/4. \quad (3.22)$$

Proof. This is the first term of a Taylor series for $cdf(\phi_{\min})$. \square

Theorem 21. *For M points distributed independently and uniformly on the unit sphere, the expected value of the minimum latitude is*

$$E_M := \mathbb{E}[\min(\phi_1, \dots, \phi_M)] = \frac{M}{2^M} \int_{-1}^1 (\xi + 1)^{M-1} \cos^{-1}(\xi) d\xi$$

$$= M \int_0^1 \xi^{M-1} \cos^{-1}(2\xi - 1) d\xi, \quad (3.23)$$

which, for large M , is approximately

$$E_M \approx \tilde{E}_M := \frac{M\Gamma(M)\sqrt{\pi}}{\Gamma(M + \frac{3}{2})} \quad (3.24)$$

$$\approx \sqrt{\pi/M}. \quad (3.25)$$

Proof. Letting $z_{\max} = \max(z_1, \dots, z_M)$, the first integral above is the expectation of the function $\phi(z_{\max}) = \cos^{-1}(z_{\max})$ using order statistics with z_j uniformly distributed on $[-1, 1]$ [120, § 6.7]. The second integral results from a change of variables arising from mapping $\xi \in [-1, 1]$ to $(2\xi - 1) \in [0, 1]$. For large M , the integrand is negligible except near $\xi = 1$, where we can approximate it as

$$\tilde{E}_M = M \int_0^1 \xi^{M-1} \cdot 2(1 - \xi)^{1/2} d\xi,$$

which leads to (3.24). Then, (3.25) follows from $\Gamma(M + 3/2) \approx M^{3/2}\Gamma(M)$. \square

The approximate formulas show that as M grows, the MLE and expected values of ϕ_{\min} approach zero slowly, with the expected value about 25% larger of the two. The slow descent of these values can be understood intuitively by considering that if we draw points at random sequentially, each new minimum establishes a lower probability that any subsequent draw will reduce it further.

The ramification point with the minimum latitude is not necessarily the local ramification point for a singularity, but we may pessimistically assume that it is. When that is so, Theorem 18 says that endgame failure occurs when $\phi_{\min} < \phi_{\text{crit}} = \delta^* + \delta^+$. Under the assumption of uniformly distributed ramification points, (3.22) shows that we may expect the probability of failure to grow proportional to the number of branch points, but the good news is that lowering ϕ_{crit} by allocating more digits of precision pays off quadratically, as is implied by the condition number analysis given below in Section 3.4.5.

Example 22 ($2k$ bilinear quadrics with Bézout start system). Let the target system $F(u)$ be a system of $2k$ bilinear, complex quadratics $F(u) = \{f_1, \dots, f_{2k}\}$ of the form

$$f_j = \underline{x} A_j \underline{y}^T, \quad \underline{x} = [1 \ x_1 \ \cdots \ x_k], \quad \underline{y} = [1 \ y_1 \ \cdots \ y_k], \quad u = (\underline{x}, \underline{y}) \in \mathbb{C}^{2k},$$

where each $A_j \in \mathbb{C}^{(k+1) \times (k+1)}$ with elements chosen uniformly within the box $[-1, 1] \times [-i, i] \subset \mathbb{C}$. Since F is a system of quadratics, one option for solving it is via a homotopy where G is a Bézout start system of the form

$$G(u) = \{g_1, \dots, g_{2k}\}, \quad g_j = u_j^2 - 1.$$

The corresponding homotopy (3.3) has 2^{2k} solutions at $\tau = [1, 0]$ which is the number of solution paths. At $\tau = [0, 1]$, bilinearity causes $V(F)$ to consist of only $\binom{2k}{k}$ non-singular roots. The difference, namely $2^{2k} - \binom{2k}{k}$, consists of solution paths that diverge to infinity. After homogenizing the homotopy via $\mathbb{C}^{2k} \hookrightarrow \mathbb{P}^{2k}$, we have

$$h(\underline{u}, \tau) = a\tilde{G}(\underline{u}) + b\tilde{F}(\underline{u})$$

$$\begin{aligned} \tilde{f}_j &= \underline{X} A_j \underline{Y}^T, \quad \underline{X} = [u_0 \ x_1 \ \cdots \ x_k], \quad \underline{Y} = [u_0 \ y_1 \ \cdots \ y_k], \\ \underline{u} &= [u_0 \ x_1 \ \cdots \ x_k \ y_1 \ \cdots \ y_k] \in \mathbb{P}^{2k}, \end{aligned}$$

with start system $\tilde{g}_j = u_j^2 - u_0^2$. For computations, we pick a random patch on \mathbb{P}^{2k} , which maps the divergent endpoints in \mathbb{C}^{2k} to finite points in \mathbb{P}^{2k} thus making them easily computable.

With $k = 3$, only $\binom{6}{3} = 20$ of $2^6 = 64$ solution paths end at finite solutions, while the other 44 diverge to infinity as $\tau \rightarrow [0, 1]$. The number of branch points is only 1176 compared to 1344 for a general pencil of 6 quadrics. However, the 44 endpoints at infinity are singular, so a singular endgame is required. A computation of the branch points for a random example gave $\phi_{\min} \approx 0.00118$ which is substantially

smaller than the maximum likelihood value of ≈ 0.041 . By (3.22), the probability of obtaining this minimum value or smaller in 1176 uniformly distributed trials is approximately 4.1×10^{-4} . This implies that a uniform distribution is not a good model for predicting the distribution of ramification points near $\tau = [0, 1]$ for this highly structured homotopy. Assuming that the branch point whose ramification is close to $\tau = [0, 1]$ marks the convergence zone of a singularity, the singular endgame will have to follow a circle of latitude inside that boundary. Enough digits of precision will need to be allocated to track that path as it passes between the ramification point and the singularity at $\tau = [0, 1]$.

Figures 3.6 and 3.7 show maps and histograms of the distribution of ramification points for this example. Despite the fact that one ramification point is unexpectedly close to $\tau = [0, 1]$, the general distribution is not skewed in that direction. In fact, most of the ramification points are in the left-hand disk, closer to $\tau = [1, 0]$ than $[0, 1]$.

Figure 3.8 shows P_{fail} for this same example. The presence of the ramification point near $[0, 1]$ shows up as a sharp jump to $P_{\text{fail}} = 1$ occurring at $\hat{\delta}^* = (M/2)\phi_{\min} \approx 0.69$ for $M = 1176$, $\phi_{\min} = 0.00118$. The initial slope of the failure curve in Fig.3.8 is 802 compared to an expectation of 588 for a uniform distribution. This higher failure rate is also due to the exceptional ramification point: according to (3.19), it contributes ≈ 270 to the slope. Note that this implies that the remaining 1175 ramification points actually contribute less than expected for a uniform distribution. This accords with our observation that the bulk of the ramification points are well away from either endpoint of the homotopy path.

3.4.4 Scaling

We mentioned in the Introduction that previous work has involved scaling, which can help in achieving a high success rate. In the running example, we have seen that

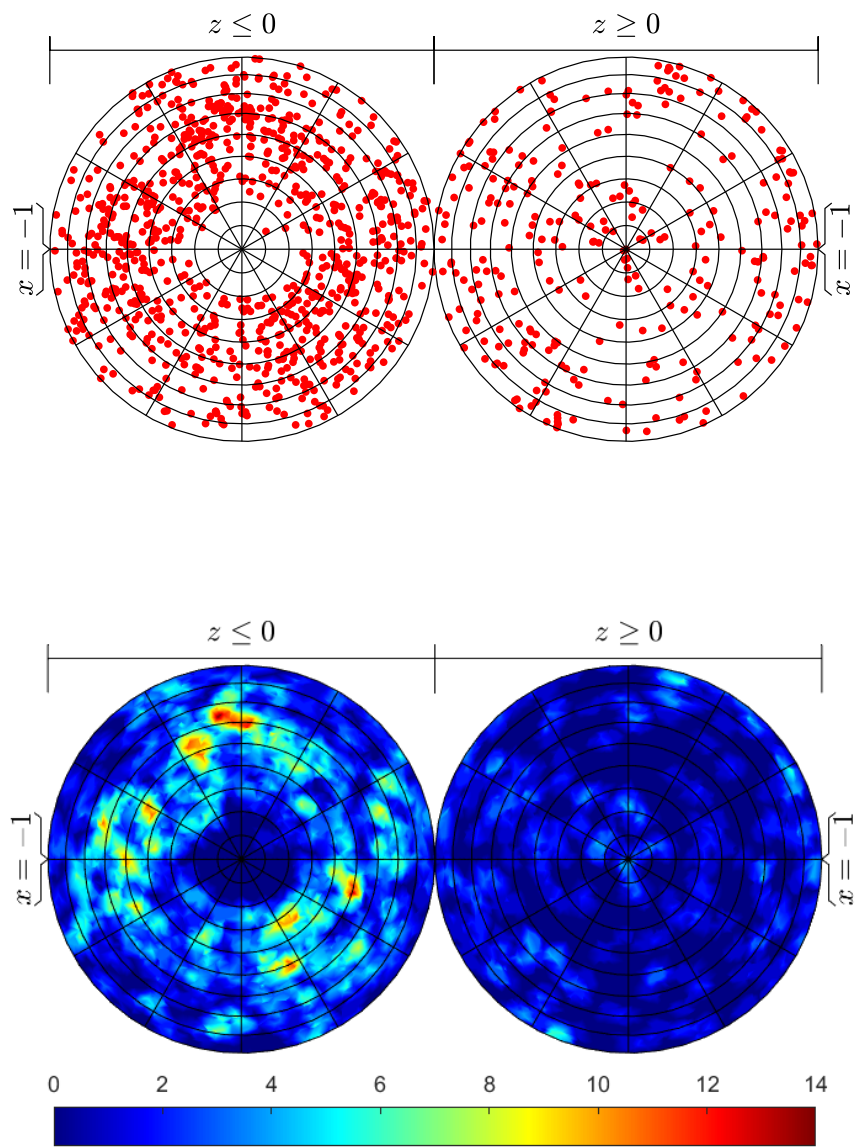


Figure 3.6. Ramification point scatter plot and heat map for $k = 3$ in Example 22.

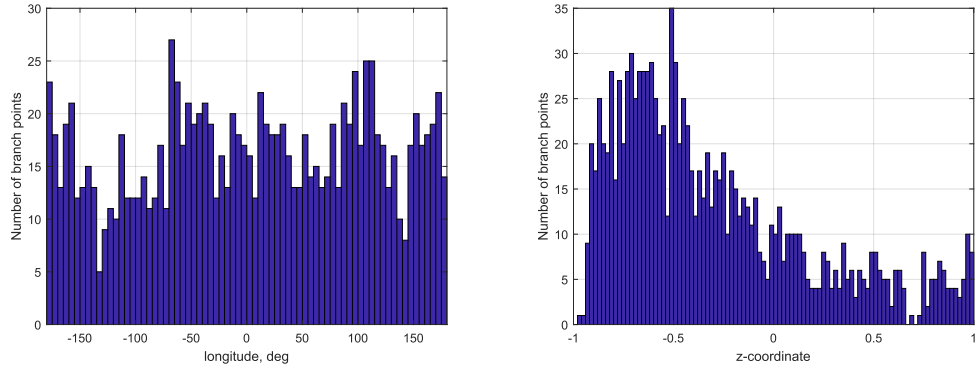


Figure 3.7. Histogram counts for number of ramification points for Example 22 with $k = 3$ along longitude $[0^\circ, \pm 180^\circ]$ (left) and the z -coordinate $[-1, 1]$ (right).

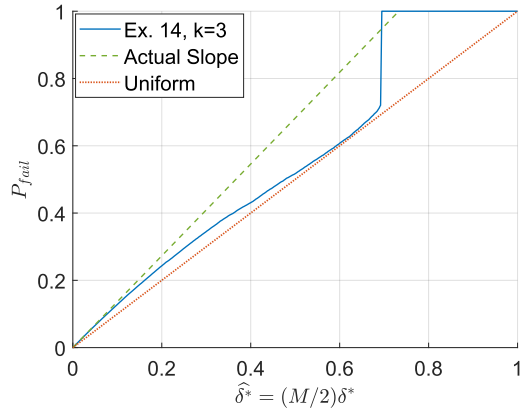


Figure 3.8. Probability of δ^* -failure, P_{fail} , versus normalized safe distance $\hat{\delta}^*$ for Example 22, $k = 3$. The diagonal red line shows the slope expected from a normal distribution of branch points. The green dotted line is the actual slope of P_{fail} , plotted in blue. The exceptional location of a ramification point close to the pole triggers $\hat{\delta}^*$ -failure at $\hat{\delta}^* \approx 0.69$.

the branch points are concentrated in an annulus centered on the start system. The radius of that annulus can be changed simply by scaling the start system. Indeed, changing the pencil to $H(u, [a, b]) = a(6G(u)) + bF(u)$, where F, G are the same as in Example 9, gives the branch point density shown in Fig. 3.9. This is a more uniform distribution than before scaling; compare it to Fig. 3.2. The upshot is an improved $P_{\text{fail}}(\delta^*)$, as is shown as the dashed curve in Fig. 3.5. In Example 9, the coefficients of F and G are commensurate, but since F is dense with $\binom{N+2}{2}$ terms and G is sparse with just 2 terms in each polynomial, F has a larger scale. The terms in F do not always align, so scaling G by N is sufficient to achieve balance. ($N = 6$ in our running example.)

The practical implication is not so important here since, although we have decreased the failure slope by a factor of 2.6, this is a weaker effect than increasing precision by just one bit, which would decrease δ^* by a factor of 4 (discussed next in Section 3.4.5). Moreover, whatever improvement scaling makes, it is limited in extent, whereas in principle, precision can be increased indefinitely. However, it does show that if the target system has significantly different scale than the start system, the ramification points will move towards one pole or the other with bad results in either reliability (if precision is fixed) or computation time (if precision is adaptive).

3.4.5 Condition number near branch points

The argument for using the δ^* -failure criterion is that distance to a branch point strongly correlates with the worst condition number among the solution paths as suggested by Fig. 3.1. Assume that $N \geq 2$ and that (u^*, τ^*) is a branch point of H . For the following analysis, we assume that this branch point arises as a quadratic singularity, which [111] shows is the generic behavior. Hence, $H_u(u^*, \tau^*)$ is rank deficient with $\|H_u(u^*, \tau^*)\| > 0$, i.e., the minimum singular value of $H_u(u^*, \tau^*)$ is zero while the corresponding maximum singular value is nonzero. Moreover, we are

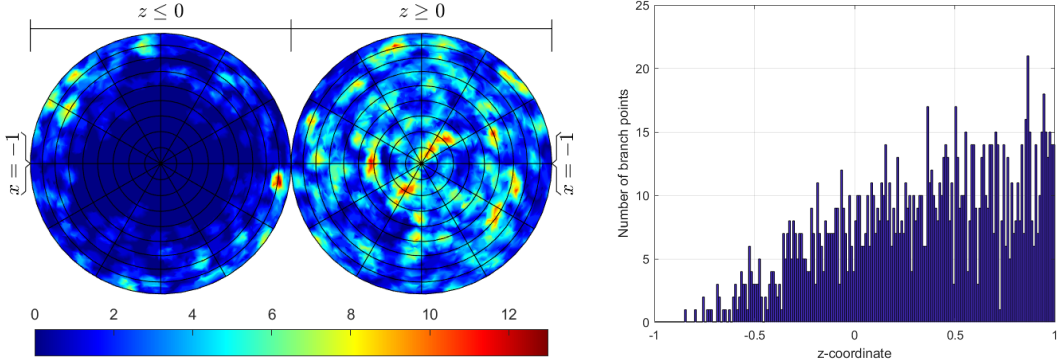


Figure 3.9. Ramification point density after scaling the start system of Example 9. Compare to Fig.s 3.2 and 3.3, and note change of scale in the color bar and the histogram counts.

assuming that along a solution path $u(\tau) \rightarrow u^*$ as $\tau \rightarrow \tau^*$, one has a first-order approximation of the form

$$\|u(\tau) - u^*\| \sim \|\tau - \tau^*\|^{1/2}, \quad \|\tau - \tau^*\| \ll 1. \quad (3.26)$$

A Taylor series expansion of $H_u(u(\tau), \tau)$ together with (3.26) shows that

$$\sigma_{\min}(H_u(u(\tau), \tau)) \lesssim \|\tau - \tau^*\|^{1/2}, \quad \|\tau - \tau^*\| \ll 1. \quad (3.27)$$

Moreover, $\|H_u(u^*, \tau^*)\| > 0$ yields that

$$\sigma_{\max}(H_u(u(\tau), \tau)) \approx \sigma_{\max}(H_u(u^*, \tau^*)), \quad \|\tau - \tau^*\| \ll 1. \quad (3.28)$$

Equations (3.27) and (3.28) show that the condition number of $H_u(u(\tau), \tau)$ behaves at most similar to $\|\tau - \tau^*\|^{-1/2}$ when $\|\tau - \tau^*\| \ll 1$.

Example 23. To experimentally verify this analysis, we randomly selected a branch point (u^*, τ^*) for the running example with $N = 6$ in Example 9 and randomly

selected one of the two paths $(u(\tau), \tau)$ converging to (u^*, τ^*) . Figure 3.10 plots the relationship between the logarithm of $\|\tau - \tau^*\|$ and the logarithm of the condition number $H_u(u(\tau), \tau)$. Since the slope of this line is approximately $-1/2$, this verifies that the condition number of $H_u(u(\tau), \tau)$ is similar to $\|\tau - \tau^*\|^{-1/2}$.

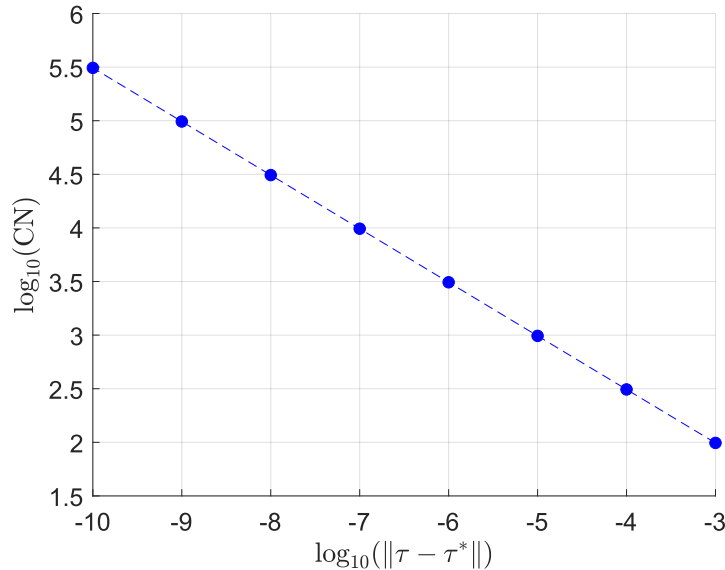


Figure 3.10. Log-log plot comparing $\|\tau - \tau^*\|$ with the condition number of $H_u(u(\tau), \tau)$ as $\tau \rightarrow \tau^*$ with the slope being approximately $-\frac{1}{2}$.

This analysis is not novel and has been observed in various contexts such as the front cover image of [18], [15, Fig. 2], and [53, Fig. 3.1]. However, the upshot is that, near a branch point, one expects the condition number to behave like the reciprocal of the square root of the distance to the corresponding ramification point. For the current context of successful path tracking, this square root is helping to keep the area of the ill-conditioned regions surrounding the branch points small. In particular,

if increasing the working precision by one bit doubles the condition number that one can tolerate, then this square root in the denominator leads roughly to a quartering of the probability of δ^* -failure for each additional bit of precision.

3.5 Examples

The following considers various quadratic systems (Section 3.5.1) and a four-bar precision point path synthesis problem (Section 3.5.2). For these problems, the branch points were computed using **Bertini** [14, 18]. When the target system has singular solutions, the corresponding bounds on the number of branch points are not sharp. In such cases, the number of branch points reported below is a lower bound on the actual number of branch points in light of the use of numerical computations.

3.5.1 Quadratic systems

Example 9 considered homotopies in \mathbb{P}^N between the Bézout start system and a target system of N general quadrics, while Example 22 changed the target system to N quadrics bilinear in two groups of $N/2$ variables each. This section considers these cases along with other related systems. In particular, we consider the following six scenarios in \mathbb{P}^N for $N = 6, 8, 10, 12$:

Case	Start system (G)	Target system (F)
1	\mathbb{C} -general quadrics	\mathbb{C} -general quadrics
2	\mathbb{R} -general quadrics	\mathbb{R} -general quadrics
3	Bézout	\mathbb{C} -general quadrics
4	Bézout	\mathbb{R} -general quadrics
5	Bézout	\mathbb{C} -general bilinears
6	Bézout	\mathbb{R} -general bilinears

Here \mathbb{C} -general and \mathbb{R} -general refers to the number field of the coefficients. Coefficients in \mathbb{C} are chosen independently and uniformly in the box $[-1, 1] \times [-i, i]$, while in \mathbb{R} the sample space is the interval $[-1, 1]$. Each start system has 2^N solutions and the first four cases have $\binom{N+1}{2}2^N$ branch points from Theorem 10 which is sharp in light of [111]. The following provides explicit values for $N = 6, 8, 10, 12$:

N	6	8	10	12
2^N	64	256	1024	4096
$\binom{N+1}{2}2^N$	1344	9216	56,320	319,488

Due to the highly structured nature for the last two cases, the number of branch points is expected to be less. The following provides the values computed using **Bertini** for these two cases:

N	6	8	10	12
# branch points	1176	8000	48,840	277,536

The ratio of the number of computed branch points to the generic count $\binom{N+1}{2}2^N$ is about 0.87 for $N = 6, 8, 10, 12$. Hence, there are roughly 13% fewer branch points than the generic case due to the presence of singularities created by targeting a bilinear system inside the family of quadrics.

Let's first consider the distribution of ramification points via histograms of their longitude and latitude. Figure 3.11 shows histograms of the longitude of the ramification points for the six cases when $N = 12$. In all cases with \mathbb{C} -general coefficients and Case 2 with \mathbb{R} -general coefficients, the longitudes are plausibly distributed uniformly. Cases 4 and 6 with \mathbb{R} -general coefficients show a marked excess of ramification points on the great circle corresponding to the real numbers (longitudes 0° and $\pm 180^\circ$), but are otherwise plausibly uniform.

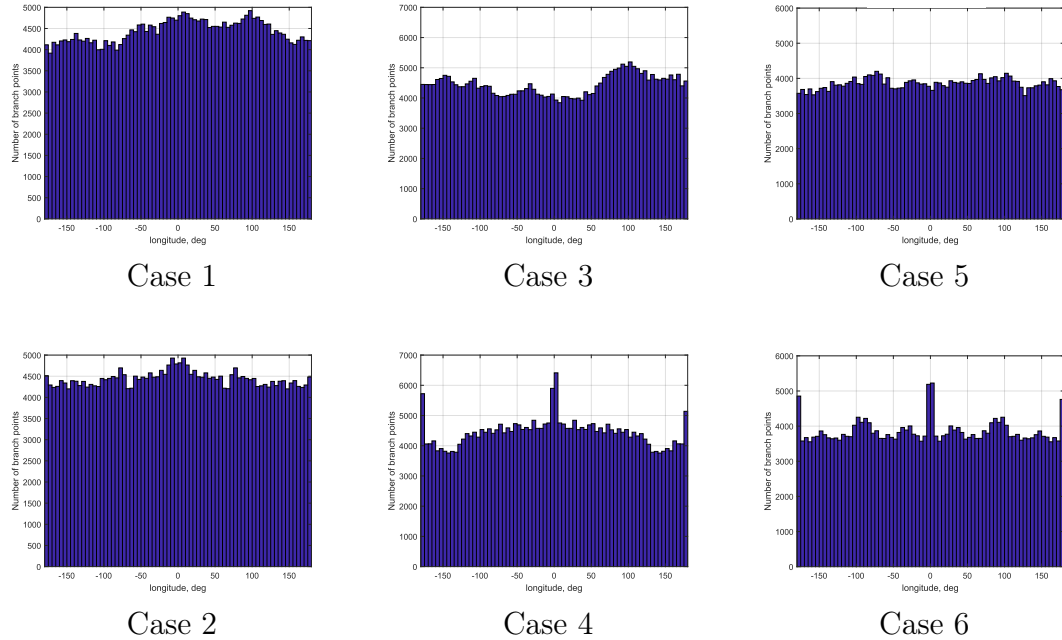


Figure 3.11. Histograms of the longitude of the ramification points for the six cases with $N = 12$

Figure 3.12 shows histograms of the z -coordinates of the ramification points. Cases 1 and 2, with general quadrics at the start and target are plausibly distributed uniformly on the Riemann sphere. In all the other cases, the Bézout start system results in a concentrated ring of ramification points near the start system, with a sparse hole immediately surrounding the start system, similar to the illustrations appearing in Section 3.2.4 for Case 3, $N = 6$. Barely visible in the histograms for Cases 5 and 6 is another ring, albeit smaller, of ramification points around the target system as the deformation from general quadrics to bilinear ones comes to completion.

The second comparison is to consider P_{fail} for the six cases with $N = 6, 8, 10, 12$. In Fig. 3.13, which shows plots of P_{fail} , the abscissa is $\widehat{\delta}^* = (M/2)\delta^*$, making the diagonal of the plot box the expected slope at $\delta^* = 0$ (solid line) for a uniform distribution, while the actual slopes are shown as dashed lines. The slopes and their expectations are tabulated in Table 3.1, where one sees that the actual slope is always of the same

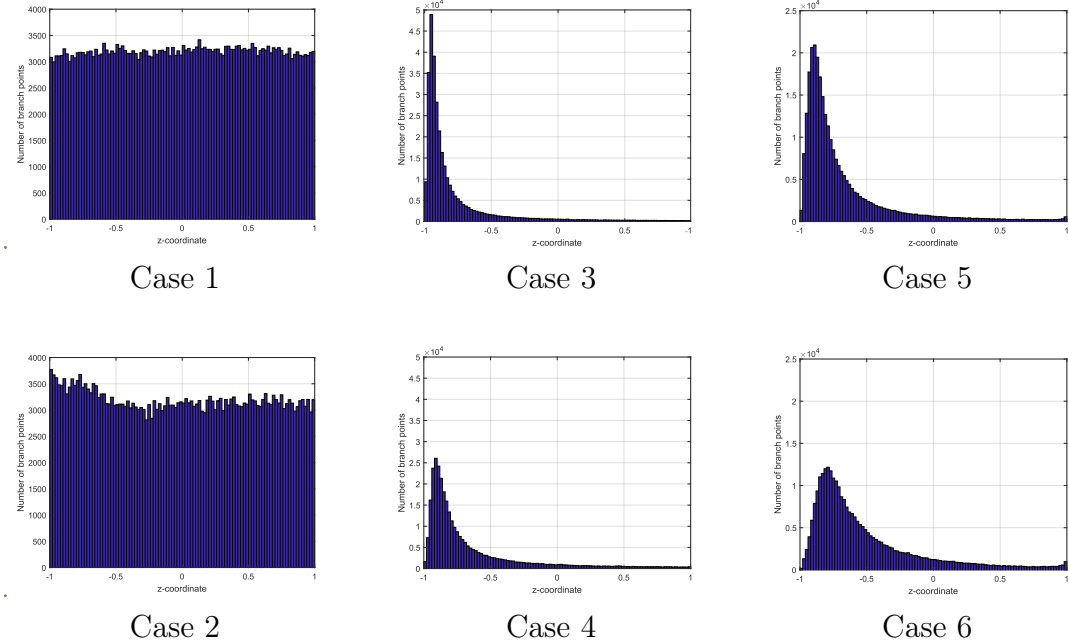


Figure 3.12. Histograms of the z -coordinates of the ramification points for the six cases with $N = 12$

order of magnitude as expected. Cases 1 and 2 show the tightest distribution around the expectation, while the largest deviation occurs for Case 3, $N = 12$, where the ratio $S/\mathbb{E}(S) = 1.57$.

The final comparison is to consider the minimum latitude for the six cases with $N = 6, 8, 10, 12$. Table 3.2 compares the minimum latitude among the ramification points, ϕ_{\min} , with the expectation from a uniform distribution, E_M , from (3.24). It also reports $cdf(\phi_{\min})$ from (3.20), which is the probability of drawing a sample with that minimum latitude or smaller if the M ramification points were distributed uniformly on the Riemann sphere. Small values of the CDF indicate that it is highly unlikely to have drawn a ϕ_{\min} so small, while values near 1 indicate that ϕ_{\min} was improbably larger than expected under the assumption of a uniform distribution. Each result is a single sample (we solved one system for each case and size). If one considers probabilities outside of the range $[0.05, 0.95]$ to be significant, one would

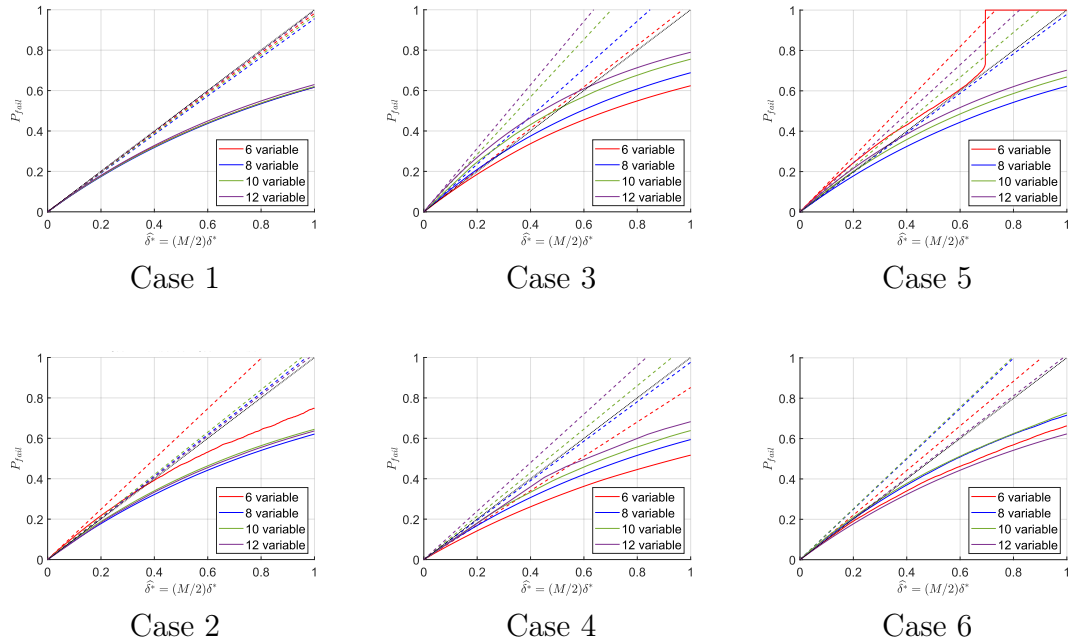


Figure 3.13. Comparison of P_{fail} for the six cases with $N = 6, 8, 10, 12$

flag 6 of 24 results as significantly low and 7 of 24 as significantly high. All of the significantly low results occur in Cases 5 and 6. Low values are associated to a greater likelihood of endgame failure, and these are precisely the two cases that have singular endpoints requiring an endgame.

3.5.2 Precision point path synthesis

As mentioned in the Introduction, the nine-point path synthesis problem for four-bar linkages motivated some early experiences with considering branch points of homotopies. Since computing branch points for the nine-point problem is currently beyond the available computational resources, we consider a related problem with fixing one pivot of the four-bar linkage and analyzing the seven-point path synthesis problem illustrated in Fig. 3.14.

Consider following the formulation in [124] using isotropic coordinates in which a

TABLE 3.1

PROBABILITY OF FAILURE SLOPES, $S = \frac{dP_{\text{fail}}}{d\delta^*}(0)$ FOR THE SIX CASES: EXPECTED VALUE, $\mathbb{E}(S)$; ACTUAL VALUE, S (ROUNDED OFF).

	$N = 6$		$N = 8$		$N = 10$		$N = 12$	
Case	$\mathbb{E}(S)$	S	$\mathbb{E}(S)$	S	$\mathbb{E}(S)$	S	$\mathbb{E}(S)$	S
1	672	660.	4608	4403.	28160	27306.	159744	158649.
2	672	836.	4608	4749.	28160	29578.	159744	162689.
3	672	693.	4608	5435.	28160	40045.	159744	250959.
4	672	572.	4608	4499.	28160	30280.	159744	191509.
5	588	802.	4000	3917.	24420	27153.	138768	168656.
6	588	650.	4000	4991.	24420	30744.	138768	140745.

real point $(a_x, a_y) \in \mathbb{R}^2$ is mapped to the complex vector $(a, \bar{a}) = (a_x + a_y i, a_x - a_y i) \in \mathbb{C}^2$. The two pivot locations are $A = (a, \bar{a})$, which is assumed fixed, and $B = (b, \bar{b})$. Two sides of the coupler triangle are given by $X = (x, \bar{x})$ and $Y = (y, \bar{y})$. To reduce the total degree of the system, auxiliary variables (n, \bar{n}) and (m, \bar{m}) are introduced along with four conditions:

$$n - a\bar{x} = \bar{n} - \bar{a}x = m - b\bar{y} = \bar{m} - \bar{b}y = 0 \quad (3.29)$$

We translate the coordinate system to place its origin at the first precision point, $D_0 = (0, 0)$, and we construct the four-bar with its coupler point at the origin as well. This satisfies the requirement to interpolate D_0 . Thus, the coupler curve passes

TABLE 3.2

MINIMUM LATITUDE FOR THE SIX CASES: NUMBER OF BRANCH
 POINTS, M ; EXPECTED MINIMUM LATITUDE, E_M ; ACTUAL
 MINIMUM LATITUDE, ϕ_{\min} ; AND $cdf(\phi_{\min})$.

Case	$N = 6$				$N = 8$			
	M	E_M	ϕ_{\min}	cdf	M	E_M	ϕ_{\min}	cdf
1	1344	0.0483	0.0531	0.61	9216	0.0185	0.0285	0.85
2	1344	0.0483	0.0619	0.72	9216	0.0185	0.00580	0.075
3	1344	0.0483	0.0689	0.80	9216	0.0185	0.0672	1.00
4	1344	0.0483	0.168	1.00	9216	0.0185	0.0106	0.23
5	1176	0.0517	0.00118	0.0004	8000	0.0198	0.00968	0.17
6	1176	0.0517	0.00437	0.006	8000	0.0198	0.000367	0.0003

Case	$N = 10$				$N = 12$			
	M	E_M	ϕ_{\min}	cdf	M	E_M	ϕ_{\min}	cdf
1	56320	0.00747	0.0150	0.96	319488	0.00314	0.00136	0.14
2	56320	0.00747	0.00272	0.099	319488	0.00314	0.00462	0.82
3	56320	0.00747	0.0207	1.00	319488	0.00314	0.0349	1.00
4	56320	0.00747	0.0299	1.00	319488	0.00314	0.00916	1.00
5	48840	0.00802	0.0103	0.73	277536	0.00336	0.000725	0.036
6	48840	0.00802	4.7e-5	2.7e-5	277536	0.00336	0.000277	0.0053

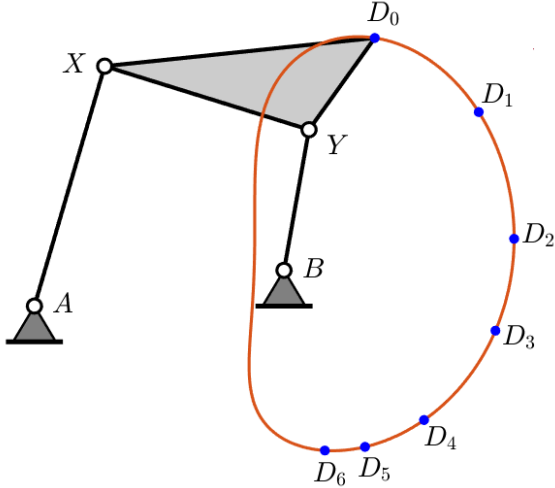


Figure 3.14. The seven-point path synthesis problem is to find all four-bars (one of which is drawn) whose coupler point passes through the precision points D_0, \dots, D_6 . Ground pivot A is given, but pivot B and the lengths of the five segments composing the mechanism are variables to be found.

through each of the other six points, say $(d, \bar{d}) \in \{D_1, \dots, D_6\}$, provided that

$$C_{(d, \bar{d})} = \rho_{(d, \bar{d})}\bar{\rho}_{(d, \bar{d})} + \rho_{(d, \bar{d})}\rho_{(d, \bar{d})}^0 + \bar{\rho}_{(d, \bar{d})}\rho_{(d, \bar{d})}^0 = 0 \quad (3.30)$$

where

$$\begin{aligned} \rho_{(d, \bar{d})} &= \det \begin{bmatrix} n - d\bar{x} & d(\bar{a} - \bar{x}) + \bar{d}(a - x) - dd\bar{d} \\ m - d\bar{y} & d(\bar{b} - \bar{y}) + \bar{d}(b - y) - dd\bar{d} \end{bmatrix}, \\ \bar{\rho}_{(d, \bar{d})} &= \det \begin{bmatrix} d(\bar{a} - \bar{x}) + \bar{d}(a - x) - dd\bar{d} & \bar{n} - \bar{d}x \\ d(\bar{b} - \bar{y}) + \bar{d}(b - y) - dd\bar{d} & \bar{m} - \bar{d}y \end{bmatrix}, \text{ and} \\ \rho_{(d, \bar{d})}^0 &= \det \begin{bmatrix} \bar{n} - \bar{d}x & n - d\bar{x} \\ \bar{m} - \bar{d}y & m - d\bar{y} \end{bmatrix}. \end{aligned}$$

With pivot $A = (a, \bar{a})$ fixed, the natural 2-homogeneous structure among the variables is given by $\{x, \bar{x}, n, \bar{n}\}$ and $\{b, \bar{b}, y, \bar{y}, m, \bar{m}\}$ with (3.29) consisting of two polynomials

of bidegree $(1, 0)$ and two polynomials of bidegree $(0, 2)$. The polynomial $C_{(d, \bar{d})}$ has bidegree $(2, 2)$. For the 7-point path synthesis problem, with precision points $D_j = (d_j, \bar{d}_j)$, $j = 1, \dots, 6$, the system becomes

$$\begin{aligned} F(x, \bar{x}, n, \bar{n}, b, \bar{b}, y, \bar{y}, m, \bar{m}) = \\ \{n - a\bar{x}, \bar{n} - \bar{a}x, m - b\bar{y}, \bar{m} - \bar{b}\bar{y}, (C_{(d_j, \bar{d}_j)}, j = 1, \dots, 6)\} \end{aligned} \quad (3.31)$$

which consists of two polynomials of bidegree $(1, 0)$, two polynomials of bidegree $(0, 2)$, and six polynomials of bidegree $(2, 2)$ with 2-homogeneous Bézout bound of 3840. Using [111], the generic number of branch points using a homotopy with this bidegree structure is 351,744. For generic data, $F = 0$ has 486 isolated solutions, which arise in cognate pairs, and mechanically-degenerate positive-dimensional components. Due to the positive-dimensional components, the generic number of branch points is expected to be smaller than 351,744.

Consider using two different start systems with the same bidegree structure. First, we used a start system constructed with the first four polynomials being $n - 1, \bar{n} - 1, m^2 - 1, \bar{m}^2 - 1$ and the remaining 6 polynomials being linear products of bidegree $(2, 2)$ with dense linears in $\{x, \hat{x}\}$ and $\{b, \hat{b}, y, \hat{y}\}$, and general coefficients. Second, we used a dense start system with the same bidegree structure having general coefficients. In both start systems, all coefficients were chosen independently and uniformly on the unit circle in the complex plane, i.e., $z \cdot \text{conj}(z) = 1$. Afterward, to establish scale, both F and G were evaluated at a point with each variable chosen at random on the complex unit circle. Then, G was re-scaled to cG using single constant, $c = \|F\|/\|G\|$.

Our computations found 305,806 branch points for the linear product start system and 313,760 branch points for the dense start system. As suggested in the Section 3.3, these may not be the exact number of branch points, but since we expect fewer than the upper bound of 351,744, it is reasonable to believe that not many were missed.

As long as none were missed extremely close to the start or end, the following analysis and illustrations would not change substantially.

For homotopies using the two start systems, Fig. 3.15 shows P_{fail} , longitude, and z -coordinate while Fig. 3.16 shows the ramification point density using a smoothing radius of 0.08 rad. A comparison of these plots shows two different behaviors on the distribution of ramification points. When using a linear product, high density regions of ramification points were clustered around both the start and target systems as well as the point corresponding to infinity. These give a slope of the P_{fail} curve approximately $31(M/2)$. When using a dense multihomogeneous start system, the ramification points were more uniformly distributed with a high density region only near the target system. Eliminating branch points near the start would seem to give the dense system an advantage, but a few points very near the end ruin this, giving a slope of approximately $65(M/2)$ for the P_{fail} curve. For points distributed uniformly on the Riemann sphere, the expected minimum latitude in both cases is $E_M \approx 3.2 \cdot 10^{-3}$, while the actual minima were $1.9 \cdot 10^{-6}$ and $4.4 \cdot 10^{-8}$. These ramification points close to the end of the homotopy path have an outsize influence on the failure slope. In the case of the dense start system, the one extremely close point contributes $46(M/2)$ of the total slope of $65(M/2)$.

Although the linear product start system shows a minor advantage in the failure slope, its main advantage over using a dense system is the ease of computing the start points.

3.6 Conclusion and Discussion

We have considered the number and distribution of branch points for homotopies for solving systems of polynomial equations. After mapping the associated ramification points to the Riemann sphere, we look at how the distribution of these points impact the success of path tracking where “success” means that *every* path is tracked

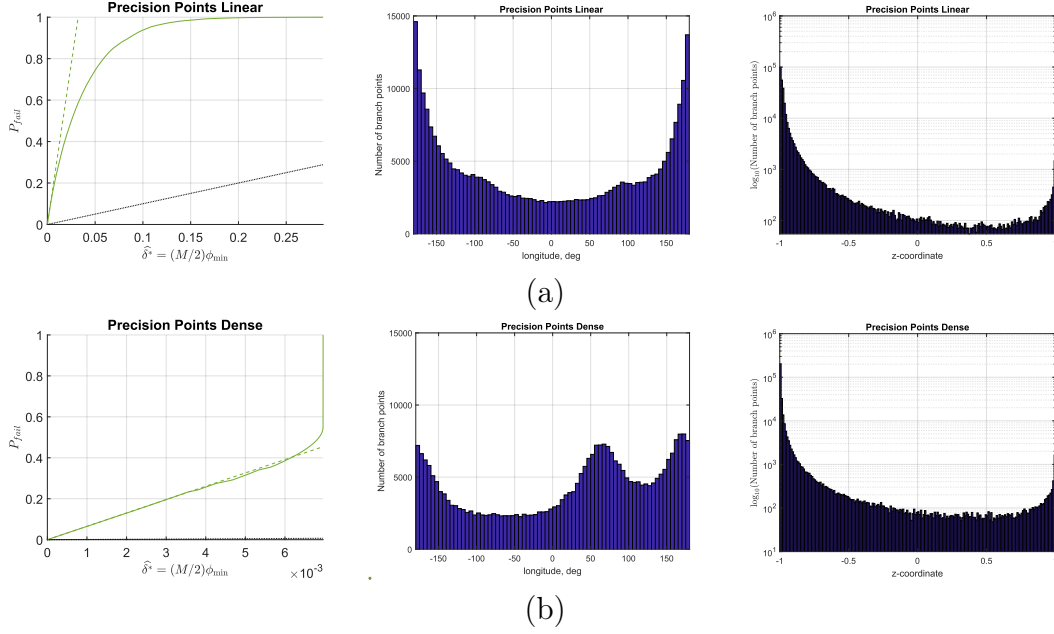


Figure 3.15. Comparison of solving 7-point problem with one fixed pivot using (a) linear product start system and (b) dense start system. The scaling pushes ramification points towards the start system, resulting in a highly skewed z -coordinate histogram. To visualize this, the histogram plot of the z -coordinate on the right uses a logarithmic (\log_{10}) vertical axis.

successfully to completion. We present several ways of visualizing the distribution of the ramification points and show how the impact can be summarized as a failure curve $P_{fail}(\delta^*)$, defined as the probability that a randomly selected homotopy path will pass within a distance of δ^* to a ramification point, measured on the Riemann sphere. The slope as $\delta^* \rightarrow 0$ is of special interest, as this directly relates to how much floating-point precision must be allocated to achieve a desired success rate. Furthermore, if the target system has singular endpoints, then the success or failure of the singular endgame, here assumed to be based on a Cauchy integral, depends on the location of the branch points of the paths leading to singularities. The endgame requires tracking paths around a monodromy loop that must pass between the end of the homotopy path and the nearest ramification point. If this gap is narrow,

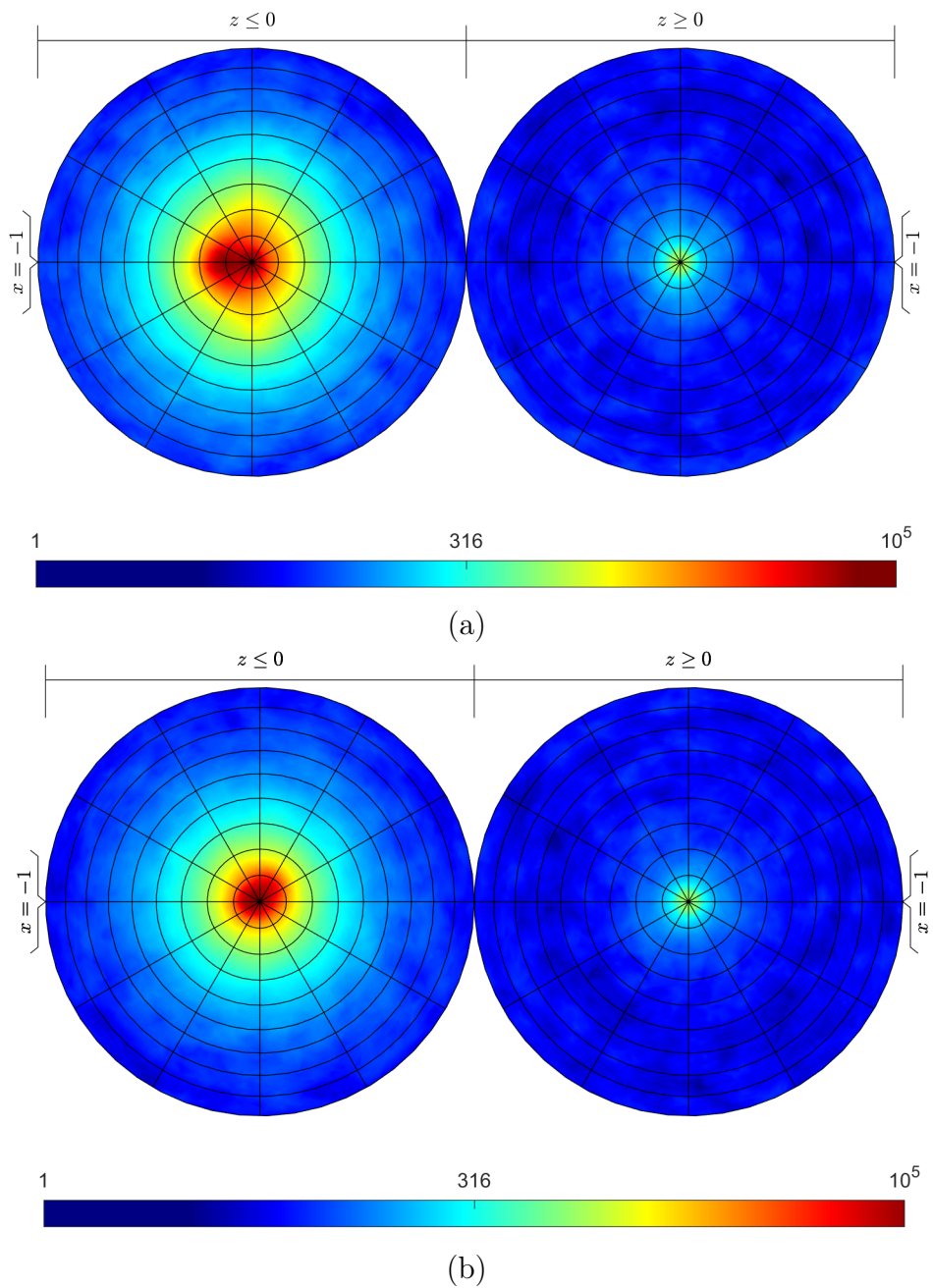


Figure 3.16. Ramification point density for solving 7-point problem with one fixed pivot using (a) linear product start system and (b) dense start system.

numerical ill-conditioning must be expected.

One should understand that numerical difficulties are due to ill-conditioning of the solution paths which arise from the inverse image of the homotopy path on the Riemann sphere. In general, each ramification point represents the crossing of just two solution paths at the associated branch point (see [111]). Perturbing the homotopy path from one that passes through a ramification point results in two solution paths passing near the branch point. These two paths will be the ones encountering the greatest numerical difficulties for the perturbed homotopy path. If one uses an adaptive precision algorithm, high precision can be invoked only as necessary. In some applications, such as the path synthesis problem, one may elect to save computation by simply discarding a few problematic solution paths; endpoints that are singular or near singular are often useless as a solution to an engineering problem. In contrast, our definition of success in this article assumes that a complete solution list is paramount.

The actual distribution of branch points is studied on examples where the start and target systems are systems of quadrics and an example from kinematics concerning four-bar path synthesis. We find that when the start and target systems are general quadrics with coefficients in \mathbb{C} , the ramification points appear to be uniformly distributed on the Riemann sphere. This largely remains true also for coefficients in \mathbb{R} , except for the presence of real ramification points appearing on the corresponding great circle on the sphere. Systems of quadrics with a Bézout start system, by which we mean one with polynomials of the form $g_j = z_j^2 - z_0^2$ for $j = 1, \dots, N$, have a notable departure from uniform distribution: although the longitude of the ramification points seems to be distributed uniformly, the same does not appear to hold for latitude. In particular, there appears to be an empty disk centered on the start system with a ring of concentrated ramification points around its perimeter. Such analysis on the distribution of ramification points is particularly important when

using monodromy to compute solutions of polynomial systems.

Despite departures from having a uniform distribution, the net effect on the initial failure slope, $\frac{dP_{\text{fail}}}{d\delta^*}(0)$, is minimal. The expected slope for a uniform distribution is $M/2$ (Theorem 16), where M is the number of branch points. For the systems of quadrics, the largest deviation from this expectation was $1.57(M/2)$, while for the path synthesis example it was a more substantial departure of $65(M/2)$. Based on these examples, we posit that $M/2$ is a good rule of thumb for the failure slope that should apply more generally. Establishing this more firmly, either by further experiments or preferably through a suitably developed theory, is an interesting question for further study. The slope is heavily influenced by the ramification points closest to the start or end of the homotopy path, and the largest departures from $M/2$ were for systems whose homotopies had singular endpoints due to the special structures of their target systems. If this is indeed a general phenomenon, then understanding how singular endpoints induce nearby branch points might lead to the construction of more reliable homotopies.

The distribution of the latitude of ramification points is directly affected by the relative scaling of the start and target systems, as illustrated by the example treated in Section 3.4.4. Re-scaling the start system from G to αG for $|\alpha| > 1$ automatically pushes the ramification points towards the end while $|\alpha| < 1$ pulls them to the start. Bad scaling in either direction will result in a system that requires the use of higher precision than would otherwise suffice.

Theorem 10 provided an upper bound on the number of branch points when all polynomials are general of the same degree and Theorem 12 refined this for the case where all polynomials defined on a product of two projective spaces are general and have the same bidegree. An enumeration of branch points for more types of homotopies, e.g., homotopies where the polynomials have different degrees and are defined on products of several projective spaces, is considered in [111].

CHAPTER 4

COMPLETE SOLUTION SETS OF FOUR-BAR APPROXIMATE PATH SYNTHESIS

The approximate path synthesis of four-bar linkages has been framed and solved with many different optimization techniques. Here we present a polynomial objective that is invariant to the number of approximate design positions selected, and a solution technique capable of finding all minima. The invariance property caps compute time despite increasing the size of input task specification data. This is performed by collecting a variable amount of task data into an invariable number of polynomial coefficients, called *moments*, before numerical optimization begins. The minima are found by applying the method of random monodromy loops to the zero gradient polynomial system of the aforementioned objective. This procedure finds all critical points, including the local and global minimum, and provides an in-process estimate of the percentage of critical points found. We applied our methodology to four-bar path synthesis problems of various computational scales by altering dimensional pre-specifications. The most general case was estimated to have $1,820,238 \pm 3810$ critical points, while pre-specification of one or two ground pivots yielded 26,052 and 503 roots, respectively, as validated by a trace test. The results are applied to a variety of examples.

4.1 Introduction

The approximate path synthesis of linkages is often formulated and solved as an optimization problem. Algorithms constructed from the current selection of opti-

mization techniques can be used to find (1) one design option, (2) several stochastically generated design options, or (3) a Pareto front of design options. Apart from the choice of optimization technique, the choice in how to construct an objective(s) yields widely varying results. In this work, we aim to compute nearly *complete* solutions to approximate kinematic synthesis problems. That is, we form nonconvex polynomial objectives and then apply polynomial homotopy continuation to first-order conditions to compute critical points. Our work is primarily advantageous over past research in that it removes guesswork over the superiority of local minima, can find minima with small regions of attraction, and, since it aims to find all minima, we can cross-compare them over auxiliary considerations neglected by the objective.

In a sense, our approach is basic in that we outright compute all stationary points from first-order conditions. However, such computations have been prohibitive in the past due to the scale of the computation. The enabling technology is the new algorithms and advances in polynomial homotopy continuation [109], notably, the method of random monodromy loops [7, 8, 39, 60, 63]. Although computational power has increased dramatically over the past decades, without the algorithmic advances of homotopy continuation, there would be no route forward to solving the problems approached in this paper.

The problems solved in this paper are related to path synthesis for the four-bar linkage (schematically shown in Fig. 4.2). In such a problem, a planar path is prescribed for a point connected to the coupler link of a four-bar to trace. The goal is to compute the dimensions of a four-bar which can approximately reproduce this path. The scale of the computation required to *completely* solve such an optimization problem can be varied by installing simplifications in the form of pre-specified dimensions, which essentially reduce the dimension of the design space. In this vein, we form three different optimization problems: approximate path synthesis for a four-bar with (1) no dimensions pre-specified, (2) one ground pivot pre-specified, and (3)

both ground pivots pre-specified. The first uses the most computational resources while the last requires the least. For each of these problems, we conduct an *ab initio* computation to estimate the generic number of critical points each optimization problem has. This is performed by forming numerically general versions of the first-order conditions and solving them with the method of random monodromy loops. The size of these finite root sets are analyzed statistically to place confidence bounds on its accuracy [60] and, if possible, certified to be complete using a trace test [25, 59]. The resulting numerically generic finite root datasets can be applied as starting points with *parameter homotopies* [89] to solve for practical (not numerically generic) engineering design problems. Such parameter homotopies track fewer paths and thus use less computational resources. We demonstrate this functionality for a variety of examples in this paper.

4.1.1 Literature review

If all dimensions of a four-bar are set to be design variables, then it can be shown that the four-bar can move a coupler point exactly through nine prescribed points generically. Wampler et al. [124] applied homotopy continuation to this problem and found the relevant polynomial system to generically have 8,652 finite roots which naturally has a 2-way symmetry from relabeling and a 3-way symmetry from Roberts' cognates [100]. Hence, there are 1,442 distinct four-bar coupler curves that pass exactly through nine prescribed points generically thereby solving Alt's problem [3]. If the two ground pivots of a four-bar are pre-specified and the rest of the dimensions are set to be design variables, then it can be shown that the four-bar can move a coupler point exactly through five prescribed points. Several authors [90, 112, 117] applied homotopy continuation to this problem and found the relevant polynomial system to generically have 36 nondegenerate, finite roots. In this work, we address analogous problems but applied to the approximate case, that is, N -point approximate

synthesis.

By alleviating the exactness requirement on the coupler trace, approximate synthesis techniques allow for a greater number of prescribed task points. These formulations lead to nonlinear optimization problems with many local minima. Examples of nonlinear programming techniques that find only a single minima include [45, 76]. As a slight improvement, the initial guess of the nonlinear program could be varied systematically [21] or randomly [73] to hopefully discover more minima. Similar to this work, other authors [101] have considered working directly with the first-order necessary conditions, and Rao algorithms [99] explore the solution population through iterative updates to ultimately find the optimal solution.

Metaheuristic algorithms [28, 29, 41, 72, 84, 102, 105, 106] are less prone to settling on an inferior local minimum. Additionally, these algorithms need no derivative information, no initial guess (usually), and are capable of generating a Pareto front to accommodate multiple objectives. Combining heuristics in trajectory synthesis affords suitable and optimum solutions even in up to 14-bar linkage mechanisms [52].

However, metaheuristic algorithms are stochastic in nature, require hyper-parameter tuning, and do not necessarily guarantee one will find a global minimum or a complete view of the optimization landscape.

Approximate synthesis techniques accommodate the approximate nature of most practical design problems. Exact synthesis methods are often criticized as few practical design problems require such exactness. However, their appeal comes in the form of their deterministic nature and, assuming complete solutions are obtained, their ability to generate multiple design options of diverse forms. This paper aims to bring that aspect of completeness to approximate synthesis. Rather than using the approximate points directly in the formulation, our approach formulates an objective based off the moments of path points. Setting its gradient equal to zero leads to a square polynomial system in the design variables. Since this polynomial system is

highly nonlinear, it possesses many roots, indicating the locations of critical points and potential minima. Polynomial homotopy continuation [18] is applied to a numerically general version of this system in order characterize the size of its solution set and compute start points for later parameter homotopies. Statistical estimates [60] yield confidence bounds on the root count and, when possible, a trace test [25, 59] is applied to certify the root counts from the previous step. Our work up until this point is numeric but nonetheless generic and conclusive. Parameter homotopies are used to compute results for specific design problems.

In the proceeding, we formulate synthesis equations and describe our numerical methods in Section 4.2. Next, we approach three four-bar path synthesis problems with various simplifications installed. We consider approximate path synthesis when no dimensions are pre-specified (Section 4.3), when one ground pivot is pre-specified (Section 4.4), and when both ground pivots are pre-specified (Section 4.5). In each case, we present practical design scenarios to showcase the utility of our approach. Section 4.7 summarizes the contribution.

4.2 Mathematical Formulation

4.2.1 Approximate synthesis equations

Consider the four-bar linkage shown in Fig. 4.2. Let A and B be the ground pivots of the linkage, and let l_1 , l_2 , l_3 be the moving link lengths as shown with angular displacements, measured counter-clockwise from the x -axis, as ϕ_1 , ϕ_2 , ϕ_3 , respectively. The coupler trace point is represented as P in the local frame of the coupler.

We introduce a vector variable Q such that

$$Q = \frac{P}{l_2},$$

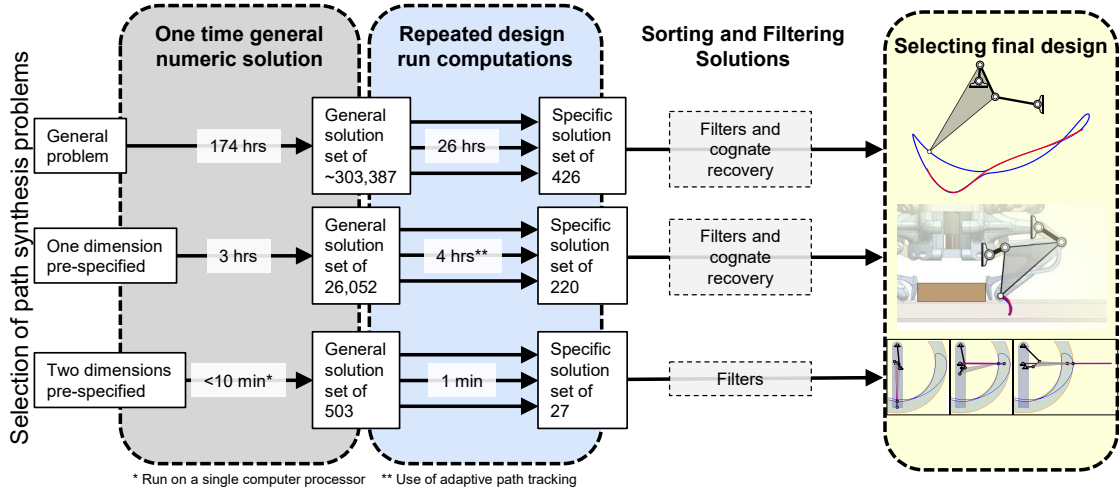


Figure 4.1. Graphical summary of the proposed method for solving the approximate path synthesis design problem.

which represents the vector P normalized by the coupler base, l_2 in the local frame. The coupler trace point in the global frame is denoted with the vector X . The use of isotropic coordinates with complex variable/parameter and its respective conjugate rather than Cartesian scalar coordinates afford simpler mathematical descriptions among other advantages.

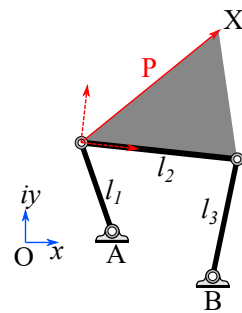


Figure 4.2. Schematic of a four-bar linkage for path synthesis.

However, one can always linearly transform between the two coordinate representations [122]. The transformation of real-valued Cartesian coordinates to isotropic is given by

$$z = x + yi, \quad \bar{z} = x - yi$$

Where x and y are real values and z is a complex value and \bar{z} is its conjugate. The transformation from isotropic to Cartesian is given by

$$x = \frac{z + \bar{z}}{2}, \quad y = \frac{z - \bar{z}}{2i}$$

Denote $\Phi_k = e^{\phi_k i}$ for $k = 1, 2, 3$ be the 2D rotation operators. Then, the vector loop equations for the left and right dyads are, respectively,

$$A + l_1\Phi_1 + l_2Q\Phi_2 = X, \tag{4.1a}$$

$$B + l_3\Phi_3 + l_2(Q - 1)\Phi_2 = X. \tag{4.1b}$$

Since we are working in isotropic coordinates, the conjugate relationship of the vector loops must be upheld. We denote conjugates with $*$ and note that the conjugate of a rotation operator is its reciprocal. That is, for a complex value $z = a + bi$, its conjugate is $z^* = a - bi$, and for a rotation operator θ , its conjugate is $\theta^* = \frac{1}{\theta}$. Additionally, since the link lengths are real-valued, they have no imaginary component and $l_k^* = l_k$ for $k = 1, 2, 3$. Hence, the conjugate loop equations are

$$A^* + l_1\frac{1}{\Phi_1} + l_2Q^*\frac{1}{\Phi_2} = X^*, \tag{4.2a}$$

$$B^* + l_3\frac{1}{\Phi_3} + l_2(Q^* - 1)\frac{1}{\Phi_2} = X^*. \tag{4.2b}$$

The rotation operators are not final design specifications, so they can be eliminated from the loop equations. Eliminating Φ_1 between Eq. 4.1a and Eq. 4.2a results in the equation

$$l_2Q^*(A - X) + (XX^* - A^*X - AX^* - l_{1s})\Phi_2 + l_2Q(A^* - X^*)\Phi_2^2 = 0, \quad (4.3)$$

where $l_{1s} = l_1^2 - l_2^2QQ^* - AA^*$. Likewise, we eliminate Φ_3 between Eq. 4.1b and Eq. 4.2b to obtain the second equation

$$l_2(Q^* - 1)(B - X) + (XX^* - B^*X - BX^* - l_{3s})\Phi_2 + l_2(Q - 1)(B^* - X^*)\Phi_2^2 = 0, \quad (4.4)$$

where $l_{3s} = l_3^2 - l_2^2(Q - 1)(Q^* - 1) - BB^*$.

To eliminate Φ_2 , we take note that the operator appears in both Eq. 4.3 and Eq. 4.4 quadratically and define a Sylvester's matrix representation using the previous two polynomials:

$$\begin{aligned} \eta(\mathbf{d}; X, X^*) = & \\ & \left| \begin{array}{cccc} Q^*(A - X) & g(X, X^*) & l_2Q(A^* - X^*) & 0 \\ 0 & l_2Q^*(A - X) & g(X, X^*) & Q(A^* - X^*) \\ (Q^* - 1)(B - X) & h(X, X^*) & l_2(Q - 1)(B^* - X^*) & 0 \\ 0 & l_2(Q^* - 1)(B - X) & h(X, X^*) & (Q - 1)(B^* - X^*) \end{array} \right| \end{aligned} \quad (4.5)$$

where $g(X, X^*) = XX^* - A^*X - AX^* - l_{1s}$ and $h(X, X^*) = XX^* - B^*X - BX^* - l_{3s}$. Note that l_2 is a common nonzero factor to columns 1 and 4, therefore we drop it from

the matrix expression. We capitalize on the further numerical advantages provided by substituting $l_{2s} = l_2^2$ in the expanded form of Eq. 4.5.

The determinant of the Sylvester's matrix eliminates Φ_2 and describes a polynomial representation of the coupler trace of a four-bar linkage with the variables $\mathbf{d} = \{A, A^*, B, B^*, l_{1s}, l_{2s}, l_{3s}, Q, Q^*\}$. This determinant is also known as a *tri-circular sextic curve* because, in addition to being real-valued, it is of degree six in (X, X^*) . Each X and X^* only appear with degree up to 3, implying a circularity of three [122].

This tri-circular sextic determinant condition is upheld for all four-bar linkages and their respective Roberts' cognates [100]. We denote this determinant condition as $\eta(\mathbf{d}; \mathbf{p}_j)$ where \mathbf{d} is the set of design variables as previously defined and $\mathbf{p}_j = (X_j, X_j^*)$ are the design parameters, the positions in space through which we intend our determinant curve to intersect. We intend to minimize the sum of squares of a function residual rather than the distance between specified and synthesized points. It is important to note there are other ways to formulate an objective for approximate synthesis depending on the error one wishes to minimize [51].

From here on, we will denote the determinant curve with specified design positions as $\eta_j = \eta(\mathbf{d}; \mathbf{p}_j)$.

Consider the path generation problem for positions (X_j, X_j^*) for $j = 1, \dots, N$ where N is the number of positions. It is well known that Alt's problem [3] for $N = 9$ generic points is equivalent to solving the nine-dimensional square system $\eta_j = 0$ for $j = 1, \dots, 9$. When $N > 9$ and the design positions are generic, the exact path synthesis problem has no solutions; therefore, one must describe a formulation for an approximate path synthesis.

Our method of approximation minimizes the residuals of the coupler-trace equation previously described based on an \mathbf{L}_2 -norm measure. This sum-of-squares measure preserves the system's polynomial nature and is real-valued. That is, one aims to solve the unconstrained optimization problem $\min \sum_{j=1}^N \eta_j^2$ by computing all solutions

to the respective first-order optimality conditions:

$$\sum_{j=1}^N \eta_j \frac{\partial \eta_j}{\partial \mathbf{d}} = \mathbf{0}. \quad (4.6)$$

This problem can, and has been, solved at face value, by preserving the use of design positions as the system's parameters [9].

There theoretically is no limit to the specified number N of design positions in this formulation. However, using as many as up to $N = 20$ positions introduces additional parameter terms into already verbose expressions, thus increasing computational costs. Since these design positions appear nonlinearly in η_j , we propose an alternative parameterization that instead works with the essential information of the design positions.

The essential information is captured by the *moments* of the data. Recall that moments mathematically provide descriptive measurements of data. For example, the first moment of a probability distribution is the mean which describes the center of probability mass. By expanding the objective function in (4.6), and collecting coefficients on the sum of design positions, one observes that the determinant curve depends linearly upon 47 moments of the monomials of (X_j, X_j^*) for $j = 1, \dots, N$ that appear within the coupler equation. These moments are of the form

$$\frac{1}{N} \sum_{j=1}^N X_j^a X_j^{*b} \quad (4.7)$$

where $0 \leq a, b \leq 6$, because, recall that the coupler curve is tri-circular sextic, X, X^* can be at most degree six. In theory, there are $7 \cdot 7 = 49$ moments; however, $(a, b) = (0, 0)$ is a constant value of 1 and $(a, b) = (6, 6)$ does not appear in the expansion, so we retain $49 - 2 = 47$ moments.

Let $\mathbf{g} = \{g_1, g_2, \dots, g_{47}\}$ be the set of the moment parameters with

$$g_1 = \frac{1}{N} \sum_{j=1}^N X_j, \dots, g_{47} = \frac{1}{N} \sum_{j=1}^N X_j^6 X_j^{*5}.$$

Each moment in \mathbf{g} depends on the exponents (a, b) as in (4.7). For the general case with no pre-specified dimensions, the 47 moments correspond with the exponents (a, b) in Table 4.1. When one or both pivot locations are pre-specified, the 41 moments correspond with the exponents (a, b) in Table 4.2. Note that the lesser number of moments between the no pre-specified dimensions and one and two pre-specified dimensions cases is a consequence of defining a pivot location at the origin, which was assigned to pivot $B = B^* = (0, 0)^T$ without loss of generality.

In particular, the pre-specification of the B and B^* pivot location results in the original monomials corresponding to $g_5 = (0, 5), g_6 = (0, 6), g_{13} = (1, 6), g_{35} = (5, 0), g_{42} = (6, 0)$, and $g_{43} = (6, 1)$ vanishing in this new set of 41 moments.

TABLE 4.1

EXPONENTS (a, b) FOR THE 47 MOMENTS IN THE GENERAL CASE

1 = (0,1)	8 = (1,1)	15 = (2,1)	22 = (3,1)	29 = (4,1)	36 = (5,1)	43 = (6,1)
2 = (0,2)	9 = (1,2)	16 = (2,2)	23 = (3,2)	30 = (4,2)	37 = (5,2)	44 = (6,2)
3 = (0,3)	10 = (1,3)	17 = (2,3)	24 = (3,3)	31 = (4,3)	38 = (5,3)	45 = (6,3)
4 = (0,4)	11 = (1,4)	18 = (2,4)	25 = (3,4)	32 = (4,4)	39 = (5,4)	46 = (6,4)
5 = (0,5)	12 = (1,5)	19 = (2,5)	26 = (3,5)	33 = (4,5)	40 = (5,5)	47 = (6,5)
6 = (0,6)	13 = (1,6)	20 = (2,6)	27 = (3,6)	34 = (4,6)	41 = (5,6)	
7 = (1,0)	14 = (2,0)	21 = (3,0)	28 = (4,0)	35 = (5,0)	42 = (6,0)	

TABLE 4.2
 EXPONENTS (a, b) FOR THE 41 MOMENTS WHEN ONE OR BOTH
 GROUND PIVOTS ARE PRE-SPECIFIED

1 = (0,1)	7 = (1,2)	13 = (2,2)	19 = (3,1)	25 = (4,0)	31 = (4,6)	37 = (5,6)
2 = (0,2)	8 = (1,3)	14 = (2,3)	20 = (3,2)	26 = (4,1)	32 = (5,1)	38 = (6,2)
3 = (0,3)	9 = (1,4)	15 = (2,4)	21 = (3,3)	27 = (4,2)	33 = (5,2)	39 = (6,3)
4 = (0,4)	10 = (1,5)	16 = (2,5)	22 = (3,4)	28 = (4,3)	34 = (5,3)	40 = (6,4)
5 = (1,0)	11 = (2,0)	17 = (2,6)	23 = (3,5)	29 = (4,4)	35 = (5,4)	41 = (6,5)
6 = (1,1)	12 = (2,1)	18 = (3,0)	24 = (3,6)	30 = (4,5)	36 = (5,5)	

With this new formulation, one have an equivalent representation of the objective function we denote as

$$\psi(\mathbf{d}; \mathbf{g}) = \sum_{j=1}^N \eta(\mathbf{d}; \mathbf{p}_j) \quad (4.8)$$

which is linear in \mathbf{g} . The first-order optimality conditions yield $\nabla_{\mathbf{d}}\psi(\mathbf{d}; \mathbf{g}) = \mathbf{0}$, which are also linear in \mathbf{g} .

When moving to a different representation, it is a natural question to consider the image of the map between the two spaces. Namely, if the number of solutions is preserved between spaces. This can be addressed using [61, Lemma 3] which yields the following.

Proposition 24. *The image of the map from the design positions to the 47-dimensional moment space is full dimensional for sufficiently large N . In fact, this is guaranteed when $2N > 47$.*

The image from design positions to the moment space is dense. Hence, a sufficient

condition for the generic number of roots using the moment-formulation and the design position-formulation agree when $2N > 47$.

However, it is not a necessary condition. One only needs to ensure $N > 9$ for optimal synthesis, but heuristically a lesser N will still admit an equivalent number of solutions between formulations.

Furthermore, by using a moment formulation, one can consider moments defined by discrete design position points or continuous families of design positions. For example, for a family $(X(s), X^*(s))$ with $s_0 \leq s \leq s_1$, one can replace (4.7) with

$$\frac{\int_{s_0}^{s_1} X(s)^a X^*(s)^b ds}{\int_{s_0}^{s_1} ds}. \quad (4.9)$$

Finally, although the moment parameters bear little physical meaning, their linear appearance improves both the local conditioning of the system and the solving of the system via random monodromy loops.

4.2.2 Random monodromy loops

A random monodromy loop (RML) is a numerical continuation technique that starts with an initial seed set of solutions given defined parameters, applies monodromy action, and ends the loop at the original set of parameters. In our RML method, the solution paths travel to pre-defined intermediary yet generic systems. The solution paths are not guaranteed to return to the original solution from which their path had started, so consequently the set of solutions the RML ends with can consist of both previously known solutions and new, valid solutions. Through iterative applications of RML and compilation of unique starting solutions, one efficiently computes the the system solutions.

First, we fixed a randomly selected set of moment parameters \mathbf{g}_s and obtained the respective variable solutions such that $\psi(\mathbf{d}; \mathbf{g}_s) = 0$. Since we are aiming to

solve for the generic solution set of our system, this seed solution does not need to satisfy the conjugate relationship. Additionally, such a seed solution can be obtained using a local method such as Newton’s method or a Newton homotopy. With this seed, we employed RML along a triangular “loop” in the parameter space with our starting system at the vertex defined by the parameter set \mathbf{g}_s and the other two vertices defined by two intermediary generic system parameters, $\mathbf{g}_1, \mathbf{g}_2$, respectively. Since the parameters are linear, and a triangle is topologically equivalent to a circle, our RML consists of three applications of a straight-line homotopy along the three vertices of the triangle.

$$\begin{aligned} H_1(\mathbf{d}; t) &= \psi(\mathbf{d}; \mathbf{g}_s)t + \psi(\mathbf{d}; \mathbf{g}_1)(1-t), & t \in [0, 1], \\ H_2(\mathbf{d}; t) &= \psi(\mathbf{d}; \mathbf{g}_1)t + \psi(\mathbf{d}; \mathbf{g}_2)(1-t), & t \in [0, 1], \\ H_3(\mathbf{d}; t) &= \psi(\mathbf{d}; \mathbf{g}_2)t + \psi(\mathbf{d}; \mathbf{g}_s)(1-t). & t \in [0, 1]. \end{aligned} \quad (4.10)$$

Thus we accumulated a solution set to our system as defined by the parameter set \mathbf{g}_s . Starting from one seed solution, perfect tracking would leave 2 solutions after completing the first loop, 4 solutions after the second, 8 solutions after the third, and so on. While this iterative action increases the number of paths tracked and leads to improved rate of solution set saturation, it comes at a computational cost as we double the number of paths we track each loop. We note that our formulation, $\psi(\mathbf{d}; \mathbf{g})$ and the corresponding solution paths are invariant under Roberts’ cognates. So we apply a cognate check between loops to ensure we track only one member per cognate group as the respective Roberts’ cognate designs can be recovered through known transformations applied in post-processing of the solutions. This provides great efficiency in computing solutions to larger systems.

4.2.3 Schnabel estimator

Since the number of isolated solutions is finite, such a doubling process in the collection of solutions can not continue indefinitely. Thus, by comparing the number of new solutions obtained with the number of repeated solutions per RML, one can obtain statistical estimates on the total number of solutions using a probabilistic “catch and release” model [60]. One such model is the Schnabel model.

When applied to biological populations, the Schnabel model relies on data from previous marks and captures to yield an estimator on the total number of a wild specie’s population. In this paper, the population of interest and unknown size is the number of solutions to the *ab initio* solve of our experiments. We used a window size of three; the Schnabel estimator of the total solution count is dependent on data from the current and two previous RML applications.

The expressions of the Schnabel estimator, β , and its variance over the moving window size three as well as the 95% confidence interval bounds, respectively, are

$$\begin{aligned}\beta &= \frac{\sum_{k=1}^3 \#S^{(k)} \cdot \#E^{(k)}}{\sum_{k=1}^3 \#(S^{(k)} \cap E^{(k)})}, \\ \text{var}(\beta^{-1}) &= \frac{\sum_{k=1}^3 \#(S^{(k)} \cap E^{(k)})}{(\sum_{k=1}^3 \#S^{(k)} \cdot \#E^{(k)})^2}, \\ &\left((\beta^{-1} - 1.96\sqrt{\text{var}(\beta^{-1})})^{-1}, (\beta^{-1} + 1.96\sqrt{\text{var}(\beta^{-1})})^{-1} \right).\end{aligned}\tag{4.11}$$

Where $\#S$ is the number of solutions with which we start one RML application, $\#E$ is the number of solutions with which we end the RML application, and $\#(S \cap E)$ is the number of “repeat” solutions that belong to both sets S and E .

4.2.4 Trace test

Although the number of compiled solutions and the Schnabel estimate provide confidence on the total number of solutions, one may wish to verify that all solu-

tions have indeed been found. This can be accomplished via a 2-homogeneous trace test [59]. The 2-homogeneity arises from the design variables \mathbf{d} and the moment parameters \mathbf{g} . With such a test, one needs to collect two solution sets. The first set is computed as described previously with the moment parameters fixed. In the second set, one selects a design variable to be a parameter and selects a moment parameter to be a variable, and repeats the solving process as above. By using these two solution sets, the 2-homogeneous trace test [59] can determine if the solution sets are complete or not.

For the computations in this paper, we employed the second derivative trace test from [25, § 2.3] to avoid tracking additional paths. In particular, this *local trace test* approach simply relies upon computing local Jacobian and Hessian information of ψ to perform the trace test.

The following three sections utilize the aforementioned techniques on three formulations: the general case with no pre-specified dimensions, pre-specification of one ground pivot, and pre-specification of both ground pivots, respectively. Each problem was first solved in an *ab initio* run using random monodromy loops with the size of the solution set tested using either a statistical probabilistic model on the RML iterations or a trace test computation, or both. Finally, in each of these three formulations, we present a real-world example application. All computations were run using *Bertini*[12] in parallel mode on a four node dual 192 core machine at the University of Notre Dame’s Center for Research Computing.

4.3 The General Case (No Pre-specification of Dimensions)

4.3.1 Ab initio computation

Following Section 4.2, the general case has design variables $\mathbf{d} = \{A, A^*, B, B^*, l_{1s}, l_{2s}, l_{3s}, Q, Q^*\}$ and moment parameters $\mathbf{g} = \{g_1, \dots, g_{47}\}$ as

listed in B.1. With Roberts' cognates and relabeling, the solutions arise in groups of 6 with formulas listed in B.1. With this setup, the RML procedure was used to determine the generic root count. Figure 4.3 shows the ratio of repeated solutions for the iterations and the Schnabel estimates with the 95% confidence interval based on groups of solutions, i.e., one-sixth of the total number.

We note that to further improve the conditioning of the system when performing the random monodromy loops, we redefined the grouping of the system's variables for the homotopy. Additionally, for paths that failed between intermediary systems, we applied cognate transformations and reran the homotopy on those paths until we achieved a 100% path success rate or we exhausted each of the cognate transforms. This resulted in improving path success rate of approximately 95-97% per iteration. However, this came at an increase in the computational cost with the total time taking approximately 174 hours (7.25 days) for the *ab initio* solve.

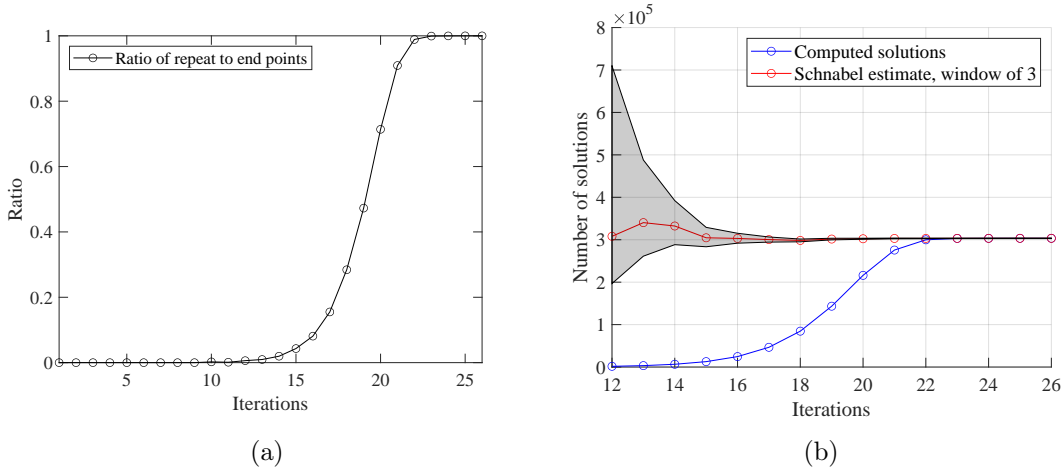


Figure 4.3. Computational summary of the *ab initio* solving for the general case formulation showing (a) the ratio of repeat solutions per RML iteration and (b) the Schnabel estimates with 95% confidence intervals.

Figure 4.3 shows 26 iterations of RML for the moment-parameterized system. The final count of distinct solution groups after the 26 RML iterations was 303,387 yielding $6 \cdot 303,387 = 1,820,322$ solutions in total. One can see in Fig. 4.3(a) that the initial RML iterations find almost exclusively new points while later iterations find almost no new points. For example, iterations 23-26 only produced 87 new solutions, hence there is strong confidence we have found $\sim 99.8\%$ of the solution set.

4.3.2 Solution set validation

From Fig. 4.3(b), one observes that the 95% confidence interval shrinks quickly for the Schnabel estimate with a moving window of size 3 as the number of iterations increases. In particular, at iteration 26, the 95% confidence interval for the Schnabel estimate is $6 \cdot (303,373 \pm 635) = 1,820,238 \pm 3,810$ solutions. This is within a rather tight bound when regarding the size of the system, and the RML computation count from the previous section lies within this bound. The total isolated solution count is estimated to be upwards of approximately two million solutions, cognate transformations included [9].

We did not employ a trace test on this system for two reasons. First, the set of known solutions is probably not complete and thus more iterations would be needed. Also, solving for the switched variable-parameter systems poses an equally arduous challenge. Therefore, for this problem, we rely upon the statistical estimates to provide that the solution set is nearly complete.

4.3.3 Applied example

As an illustration of using this *ab initio* computation to solve an applied problem, we consider approximately replicating the curve in [104, Fig. 6]. This curve is traced by a Stephenson III six-bar mechanism with a torsion spring link. The mechanism is a locomotive hopping machine with three main trajectory phases: stance phase

without spring activation, stance phase with spring activation, and swing phase.

The mechanism consists of three ground pivots, A, B, O , where the remaining pivot locations, C, D, E, F, P are described by the leg lengths

$OC, AD, CE, DE, EF, BF, EP$, and FP . The torsion spring has an additional link OS , but, for simplicity, we assumed the torsion spring leg, described by the parameter OC , to be a constant length. The triangle formed between the pivots $OCAD$ that describes the location of pivot E has an internal angle of $\kappa_1 = -59.46^\circ$ and the triangle formed between the links $OCFB$ that describes the location of the coupler point P has an internal angle of $\kappa_2 = -18.63^\circ$.

The six-bar mechanism and coupler curve from which we extracted design positions to compute the 47 continuous moment parameters is shown in Fig. 4.4.

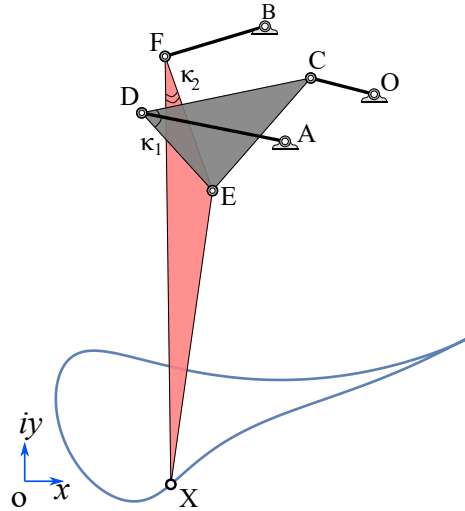


Figure 4.4. The six-bar mechanism and coupler curve used for the applied example of the general case.

Using the following parameters for the mechanism, we computed the 6-bar kine-

matics and obtained the coupler curve from [104, Fig. 6]. Note the pivot O is at the origin, so $O = O^* = 0 + 0i$.

$$\begin{aligned} A &= -3.81 - 2.02i, \quad A^* = -3.81 + 2.02i, \\ B &= -4.67 + 2.91i, \quad B^* = -4.67 - 2.91i \\ |OC| &= 2.8, \quad |AD| = 6.25, \quad |CE| = 6.40, \quad |DE| = 4.50 \\ |EF| &= 6.10, \quad |BF| = 4.46, \quad |EP| = 12.71, \quad |FP| = 18.34 \end{aligned}$$

We then extracted over a hundred sample points from the computed curve that belonged to the stance phases with and without spring activation as well as a subset of the swing phase to mimic the lift-off trajectory of the mechanism foot's from the ground. We re-parameterized the sample points to be equally spaced, rescaled them to the unit plane, generated an interpolating function, and used numerical integration to compute the continuous form of the 47 moment parameters needed for our parameter homotopy, as defined by Eq. 4.9. The numerical values of the continuous moments are given in Table B.1 in B.3.

The parameter homotopy tracked 303,387 paths from the generic parameters of the *ab initio* solve to the physically meaningful system. Using only double precision path tracking in about 26 hours of computational time, 108,008 successfully tracked to nonsingular solutions. Of these, 71 corresponded to physically meaningful designs. Due to cognate transformations, listed in B.1, we computed the cognates of the 71 unique solutions and filtered for duplicate designs. As there were no duplicates, this resulted in a total of $6 \cdot 71 = 426$ potential physically meaningful solutions. Of the 71 distinct solutions, 2 are local minima and 69 are saddle points.

Of the physically meaningful coupler curves, many had sections of their coupler curve that traced the design positions extremely well. However, these solutions faced either the issue of branch defects in the curve based on which pivot was actuated or impractical cognate design dimensions. One can see such cognate designs in Figs. 4.5.

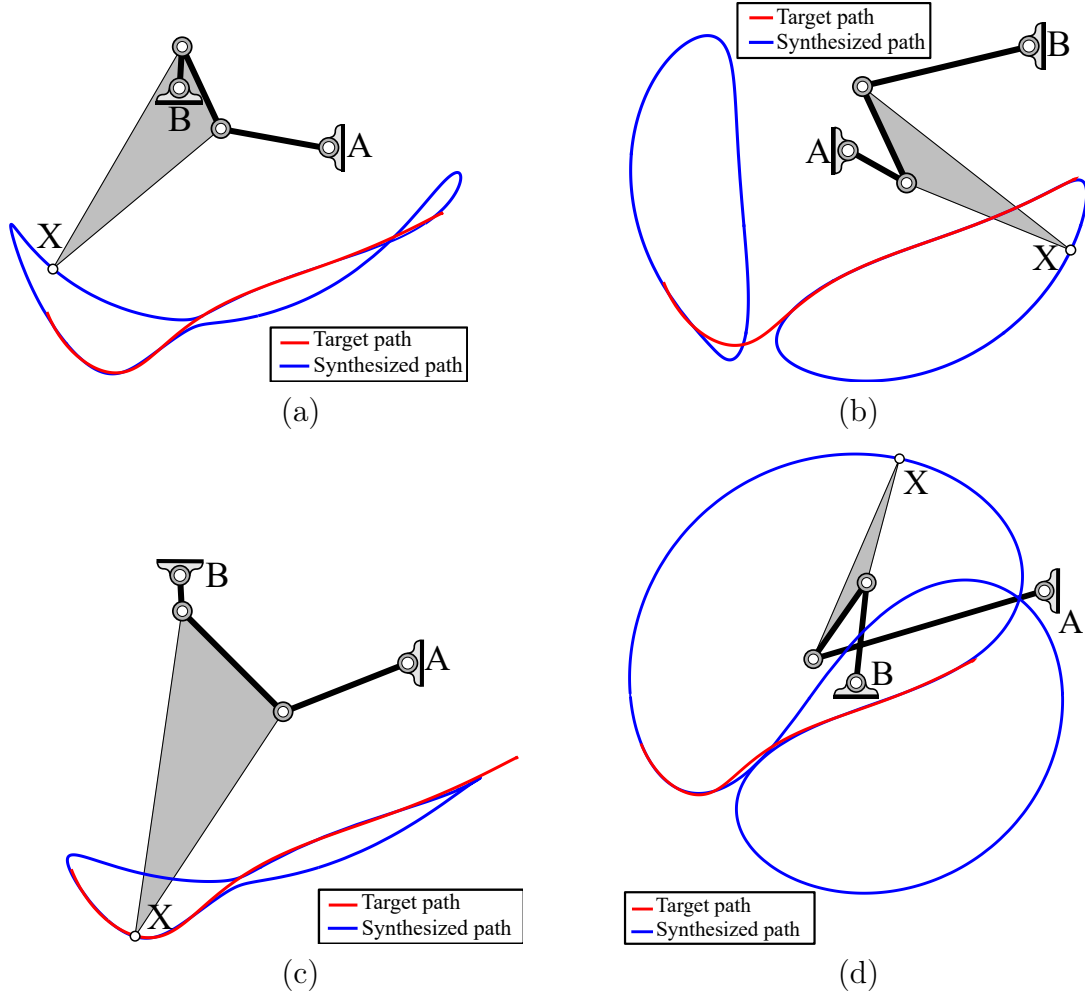


Figure 4.5. Example solutions of applied problem for the general case formulation that exhibit branch and circuit defective behavior.

The synthesized coupler curve is shown in blue. Note that different actuation on pivots can result in branch defects on the coupler curve. Therefore, we present visualizations of only the curve and a cognate group member solution.

Table 4.3 gives the dimensions of the solutions presented in Fig. 4.5 as well as two error metrics - the value of the cost function and the maximum Euclidean distance, or maximum deviation (Max Dev in solution tables), between target points and their respective nearest point on the synthesized path. This example and the results suggest that the general case formulation is not computationally effective and one

TABLE 4.3

TABLE OF FIG 4.5 SOLUTIONS AND THEIR DIMENSIONS AND
ERROR METRICS.

	Fig 4.5(a)	Fig 4.5(b)	Fig 4.5(c)	Fig 4.5(d)
A	-0.04055-0.3039 <i>i</i>	-0.2168-0.3701 <i>i</i>	0.3065-0.2725 <i>i</i>	-0.01113-0.2719 <i>i</i>
A^*	-0.04056+0.3039 <i>i</i>	-0.2168+0.3701 <i>i</i>	0.3065+0.2725 <i>i</i>	-0.01113+0.2719 <i>i</i>
B	-0.2985-0.1947 <i>i</i>	0.08195-0.1943 <i>i</i>	-0.08198-0.4600 <i>i</i>	-0.3620-0.1379 <i>i</i>
B^*	-0.2985+0.1947 <i>i</i>	0.08195+0.1943 <i>i</i>	-0.08198+0.4600 <i>i</i>	-0.3620+0.1379 <i>i</i>
l_1	0.1897	0.1102	0.5006	0.2054
l_2	0.1594	0.1802	0.1981	0.2222
l_3	0.06938	0.2866	0.2086	0.05237
Q	-0.6140+2.3195 <i>i</i>	-1.2155-1.1248 <i>i</i>	2.2589+0.4626 <i>i</i>	-0.3771+1.8417 <i>i</i>
Q^*	-0.6142-2.3195 <i>i</i>	-1.2155+1.1248 <i>i</i>	2.2589-0.4626 <i>i</i>	-0.3771-1.8417 <i>i</i>
Cost	$4.9846 \cdot 10^{-8}$	$2.008746 \cdot 10^{-8}$	$2.8040 \cdot 10^{-7}$	$7.3460 \cdot 10^{-8}$
Max Dev	0.1149	0.2075	0.1813	0.09704

would benefit from working with a smaller problem, such as the system resulting from the designation of specifications on one or both ground pivots on the four-bar final design.

4.4 Pre-specification of One Ground Pivot

4.4.1 Ab initio computation

Consider the approximate synthesis problem obtained by specifying the ground pivot $B = B^* = 0$ with design variables $\mathbf{d} = \{A, A^*, l_{1s}, l_{2s}, l_{3s}, Q, Q^*\}$. Due to the designation of the one ground pivot at the origin, some moments have a zero coefficient and thus disappear within the computation. Thus, with this pre-specification, the system admits 41 moment parameters which are provided in Table 4.2. Note that Proposition 24 still holds when $2N > 41$ for this reduced list of moments.

Using the RML procedure as previously described, the system reached convergence in 22 iterations to a final total solution count of 26,052 solutions as shown in Fig. 4.6 with a computation time of approximately 8.5 hours. The long computation time is attributed to the lack of stopping criteria on the RML code. The RML terminated after a set number of 30 iterations to ensure the total solution set was computed. Hence, there are superfluous iterations that were not essential to recovering the solution set. Had a different termination criteria be utilized, the computation time would be much faster.

Due to the specification of one ground pivot, solutions to this system come in cognate member groups of size 2 for 13,026 distinct solution groups with formulas listed in B.2. When using this cognate reduction to only track one path in each group as a check on our RML procedure and resulted in the same number of solutions, $2 \cdot 13,026 = 26,052$, that took approximately 100 minutes to compute.

4.4.2 Solution set validation

As observed in Fig. 4.6(b), the Schanbel estimates with a moving window of size 3 quickly tighten with the estimate after the 23rd iteration being $26,052 \pm 193$ solutions. With the tight Schnabel confidence interval and multiple runs that admitted the same number of solutions, this prompted using a trace test validation.

To utilize the 2-homogeneous trace test as summarized in Section 4.2.4, one needs to perform another solve where we switched the variable-parameter pair l_{1s} and g_1 . The resulting system produced 14,792 solutions and the 2-homogeneous trace test was then successfully applied to a total of $26,052 + 14,792 = 40,844$ solutions. Thus, this trace test confirmation shows that 26,052 is indeed the precise solution count.

4.4.3 Applied example

This system was applied to a gripping mechanism inspired by the solution present in [98, Fig. 5]. The original positions were chosen from [98] and fitted to a polynomial interpolation in order to define additional points for a total of $N = 20$ positions. The original pivot locations of the applied example are

$$A = -3.0432 + 4.5214i, \quad B = -0.5609 + 3.1702i$$

The other two joint dimensions are $C = 0.8155 + 2.008853i$ and $D = 1.09927 + 1.6694i$. To align this solution design with our pivot specification that $B = B^* = 0$, the B pivot of [98] was translated to the origin, and each real design position, including the additional interpolated points, was shifted by a difference of $-0.56 - 3.17i$ for B and $-0.56 + 3.17i$ for B^* . The shifted points were then divided by 3 so that their moments were within approximately unit magnitude. The shifted design positions are provided in B.3. After computing the corresponding moments, a parameter homotopy tracked 26,052 solutions in adaptive precision to the new system.

The total computation time for this parameter homotopy was approximately four hours and resulted in the successful path tracking to 25,540 nonsingular solutions. Of those nonsingular solutions, 216 obeyed the physically meaningful complex-conjugate condition. Recall that in addition to these real solutions, their respective cognates are also solutions. Since the B and B^* pivots are fixed at the origin, the valid cognate transformations must obey this pivot specification with formulas presented in B.2. We computed the cognates of these solutions, filtered for repeats, and filtered to retain one member per cognate group. This resulted in a total of 110 distinct coupler curves corresponding to physically meaningful solutions, or $2 \cdot 110 = 220$ total solution designs. Within these 110 distinct solutions, 20 are classified as minima and 90 are saddle points.

One such solution design and its respective synthesized path is presented in Fig. 4.8, the prototype mechanism based on that design is presented in Fig. 4.7(a) and Fig. 4.7(b). A model of the prototype of the gripping mechanism using legs with the selected four-bar design to pick up a small block is shown in Fig. 4.7(c).

The solution dimensions for this chosen design are given in Table 4.4. Note that this design is an saddle point, and this solution was chosen qualitatively through a visual inspection of the solutions. The coupler solution and mechanism dimensions exhibited potential use that was not seen in solutions pertaining to the lowest objective costs. For reference, the ten solutions with the lowest costs are provided in Table B.5 in B.4.

4.5 Pre-specification of Both Ground Pivots

4.5.1 Ab initio computation

The last problem under consideration is when both ground pivots are pre-specified. Consider fixing $A = A^* = 1$ and $B = B^* = 0$ so that the resulting variable list

TABLE 4.4
 NUMERICAL VALUES OF THE FINAL CHOSEN DESIGN SOLUTION
 FOR THE ONE DIMENSION PRE-SPECIFIED APPLIED EXAMPLE.

A	$0.8773 + 0.4991i$
A^*	$0.8773 - 0.4991i$
B	0
B^*	0
l_1	0.4931
l_2	1.01719
l_3	0.3090
Q	$1.1648 + 0.8395i$
Q^*	$1.1648 - 0.8395i$
Cost	12.6198
Max Dev	0.1322

is $\mathbf{d} = \{l_{1s}, l_{2s}, l_{3s}, Q, Q^*\}$. Since we retain B, B^* at the origin like the pre-specification of one ground pivot formulation in Section 4.4, this system also has 41 moment parameters listed in 4.2. For this simplified system, the RML procedure computed all 503 solutions within 13 iterations and the path tracking success rate using double precision was 99%. Using only a single processor, the total computation time was approximately three minutes. Figure 4.9 shows the ratio of number of repeats per iteration.

Since this system is small, it can be solved directly using standard homotopy continuation techniques without the use of RML in **Bertini**, a method not feasible for the other systems. This direct solve also resulted in 503 solutions from 7,362 tracked paths and took approximately ten minutes on a single processor. These 503 solutions are all distinct as the designs come in cognate groups of size one due to the pre-specified pivots.

4.5.2 Solution set validation

With such a small system that can be solved repeatedly and consistently reported 503 solutions, a statistical validation of the RML iterations was not necessary. Moreover, this solution count can be confirmed using the 2-homogeneous trace test summarized in Section 4.2.4. By switching the variable-parameter pair l_{1s} and g_{41} , the resulting system produced 129 solutions which can be directly computed with **Bertini**. The 2-homogeneous trace test was then successfully applied to a total of $503 + 129 = 632$ solutions confirming that 503 is indeed the precise solution count.

4.5.3 Applied example

We consider the application of a wing folding mechanism as shown in Fig 4.11. The wing is made up of a planar 2R chain OCD with a proximal link OC and a distal link CD . The proximal link is connected to the fuselage using a rotary joint at O .

Note that the 2R chain is by itself a two DoF system. For the folding this wing, three design configurations must be met, namely, a stowed configuration, an intermediate configuration, and a deployed configuration. The objective of this design challenge is to size a four-bar linkage (shown in black) with given ground pivot locations A and B , respectively, such that a chosen guide point X in the distal link of the 2R chain is guided approximately along the design positions, indicated in starred points, in a constrained manner.

We used the following specifications:

$$\begin{aligned} A &= 0.01 + 1.051i, \quad A^* = 0.01 - 1.051i, \\ B &= 0.137 - 0.211i, \quad B^* = 0.137 + 0.211i, \\ O &= 0, \quad |OC| = 2.563, \quad |CD| = 3.4, \quad |CX| = 0.34. \end{aligned}$$

The design positions to be met approximately are as listed in B.3. Note that the design positions specified are largely restricted to be within the reachable workspace of the guide-point X defined by the annular region as shown in Fig. 4.11. The desired curve is expected to intersect the workspace boundary in the stowed configuration and be tangential to it in the intermediate and deployed configurations.

Starting from 503 start points found during the *ab initio* run, a parameter homotopy run is carried out to the target system which represents the design problem of deployable wing mechanism. The successful paths yielded a subset of 27 physical solutions, of which 7 are local minima and 20 are saddle points. One of the local minima is found to be particularly effective in terms of packaging the system in the stowed configuration, which is shown in Fig. 4.11 at the three significant configurations of interest. For this plot, some minor corrections to the link dimensions of the overall system was made to ensure that the tangency conditions between the four-bar coupler curve and the workspace boundary of the wing guide-point X are met exactly at the intermediate and deployed configurations. The original solution computed from

the parameter homotopy, before minor corrections, is presented in Fig. 4.10. This solution is the ninth-lowest cost, the dimensions are shown in Table B.7, with a cost value of 146.1838 and a maximum deviation of 0.7273.

4.6 Discussion

The approach used in this paper forms stationarity conditions for unconstrained kinematic optimization problems and deploys a root-finding algorithm that strives for completeness in finding the zeros (critical points) associated with these conditions. The concept of solving optimization problems this way is not new, but the contribution of this paper stems from the scale of the problems confronted. Specifically, this paper computes an unconstrained problem of $\approx 1,820,238$ roots, pushing the limits the authors' available compute power.

In this paper, we did not consider optimization constraints. Equality constraints were handled in the past with homotopy-based optimization [94], but we foresee the combinatorics associated with active/inactive inequality constraints posing a challenge in computational tractability. Solving the fully generic (no pivots specified) approximate four-bar path synthesis problem alongside several inequality constraints would not be tractable with the computers used in this paper. Today's current methods already easily incorporate inequality constraints using local [45, 76] or stochastic [28, 29] optimization techniques. Our approach is neither local (sensitive to initial guess) nor stochastic (non-deterministic), laying the groundwork for potentially more complete design space exploration. Inequality constraints conveniently enforce design requirements, such as ensuring that a pivot stays within a certain region or that a link stays less than a certain length. To incorporate inequality constraints using the methods of this paper, simplifying assumptions would need to be made, such as assuming the location of one (Section 4.4) or two (Section 4.5) ground pivots. This lack of inequality constraints does not prevent our solution set from admitting

branch or circuit defective solutions. In the meanwhile, filtering the solutions after the computations adequately satisfies the requirements a designer may enforce on pivot locations and linkage lengths as well as remove the defective solutions.

This paper did not investigate the incorporation of inequality constraints. However, before such a challenge can be surmounted, the unconstrained problem needs to be investigated and characterized, which is the contribution of this paper. Our investigation discovered that the largest problem, the general case, required a large amount of computational resources, diminishing its practicality. Therefore, we included in our investigation two simplified cases (Sections 4.4 and 4.5) which trade-off generality for tractability, yielding more practical methods. Scaling up the methods of this paper to more complex multi-loop linkages, like a six-bar linkage, would not be tractable when considering the fully general (all dimensions unknown) synthesis problems. However, with the right pre-specifications, the unconstrained methods of this paper are extensible, e.g. consider converting the modular RR chain synthesis methods of [108] from exact to approximate. Furthermore, the coupler curve of any four-bar path generator can be translated anywhere in the plane by the inclusion of two more links [78, 79, 80], converting it into a six-bar. If this concession is made, the utility of inequality constraints discussed above diminishes.

4.7 Conclusions

Approximate kinematic synthesis is an appealing technique to find optimal designs of linkages. Previous optimization frameworks and solvers face the problem of settling on inferior local minima that may or may not depend on the initial solution guess and do not present a full set of the minima. Essentially, these methods fail to identify the landscape of the optimization problem. This paper presents a polynomial objective formulation to the approximate synthesis problem that can be solved via the polynomial homotopy continuation technique of random monodromy loops.

The one-time solve for the critical points of this formulation, known as the *ab initio* solve, provides a starting solution set for which parameter homotopies can be applied to physically meaningful systems of interest. To produce a linearly parameterized system, we employed a first-moment formulation of the design parameters. The resulting system was solved for three cases: no pre-specifications on design dimensions (general case), a pre-specification on one ground pivot, and a pre-specification on both ground pivots. In each case, the resulting solutions sets were used as the basis from which we computed parameter homotopies to real design application examples. The resulting total generic solution set count for the general case, pre-specification of one ground pivot, and pre-specification of both ground pivots formulations are approximately $1,820,238 \pm 3810$, and exactly 26,052 and 503 points, respectively.

4.8 Acknowledgment

Thank you to Notre Dame Aerospace and Mechanical Engineering undergraduate students Nicholas Deluca, Gabrielle Myers, and Katie Pala for construction of the gripper prototype, shown in Fig. 4.12, and thank you to Dr. Charles Wampler for his helpful comments.

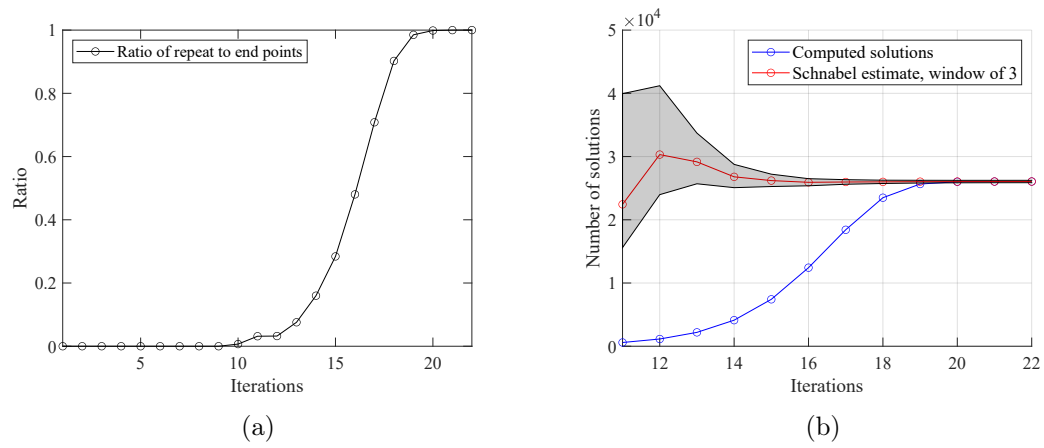
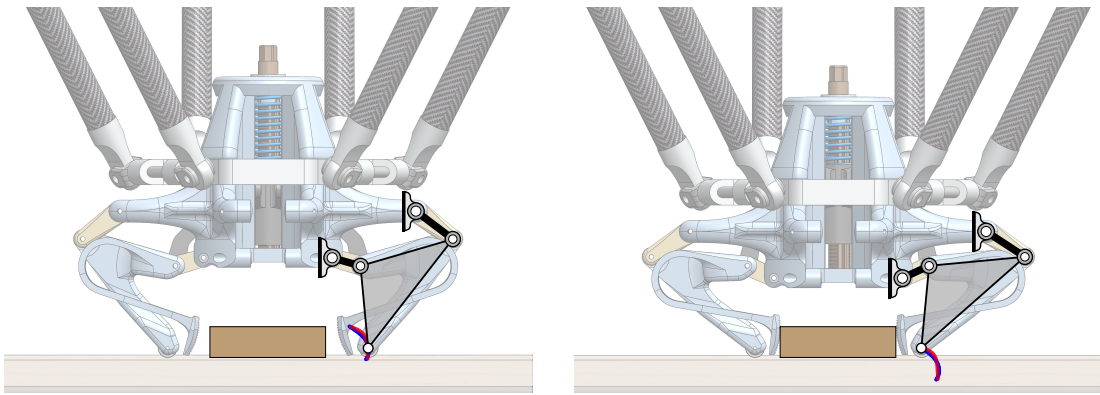
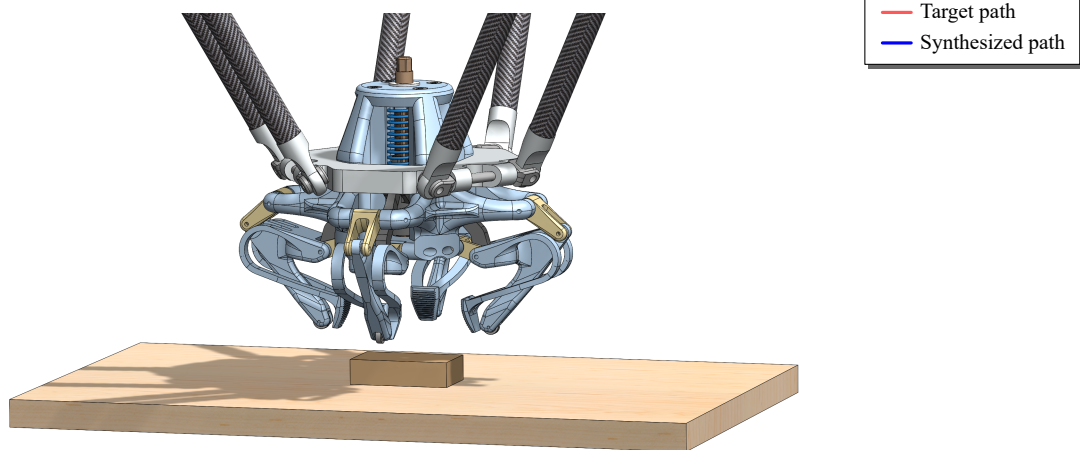


Figure 4.6. Computational summary of the *ab initio* solving when one ground pivot is pre-specified showing (a) the ratio of repeat solutions per RML iteration and (b) the Schnabel estimates with 95% confidence intervals.



(a) Contact with work surface

(b) Contact force pushes end into workpiece



(c) A gripper composed of two pairs of opposing halves

Figure 4.7. A candidate design from the pre-specification of one ground pivot computation. (a) After making contact with the work surface. (b) Said surface pushes the gripper end up, relative to itself, and into a workpiece to be gripped. Contact with the work surface actuates the gripper, and the four-bar linkage guides its end into the workpiece. (c) Such a gripper might comprise of two pairs of opposing halves.

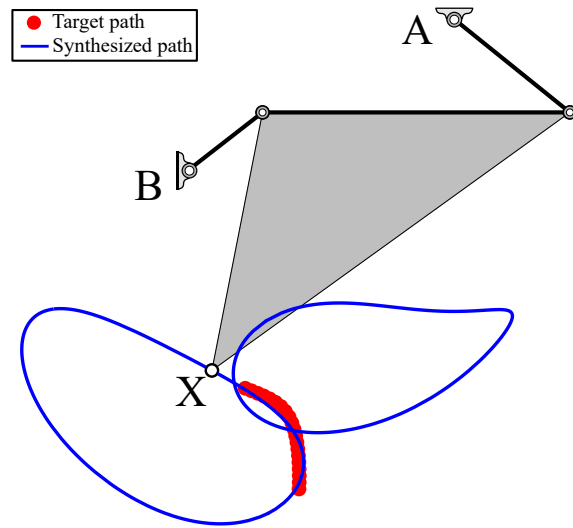


Figure 4.8. The solution design exhibiting preferred design characteristics for the one dimension pre-specified example.

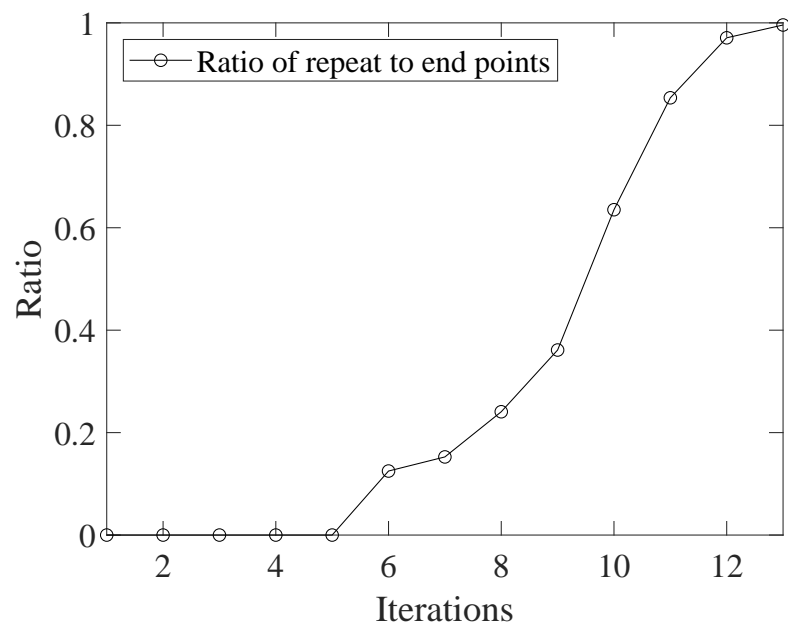


Figure 4.9. Ratio of repeat solutions per RML iteration when both ground pivots are pre-specified.

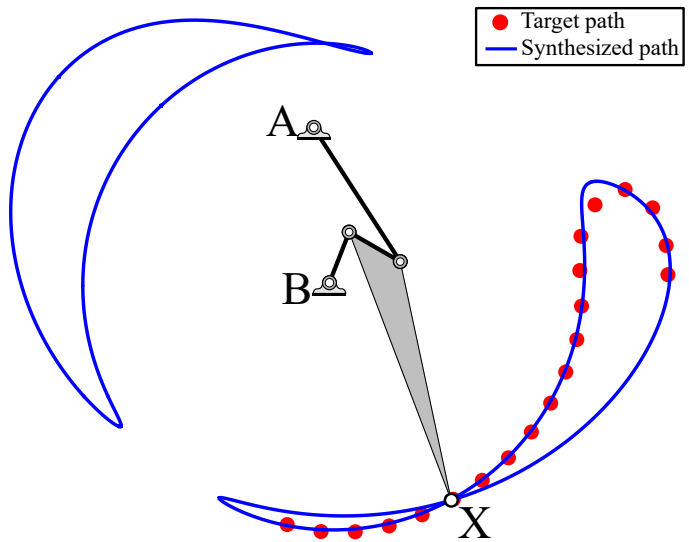


Figure 4.10. The chosen solution from which the final design was derived.

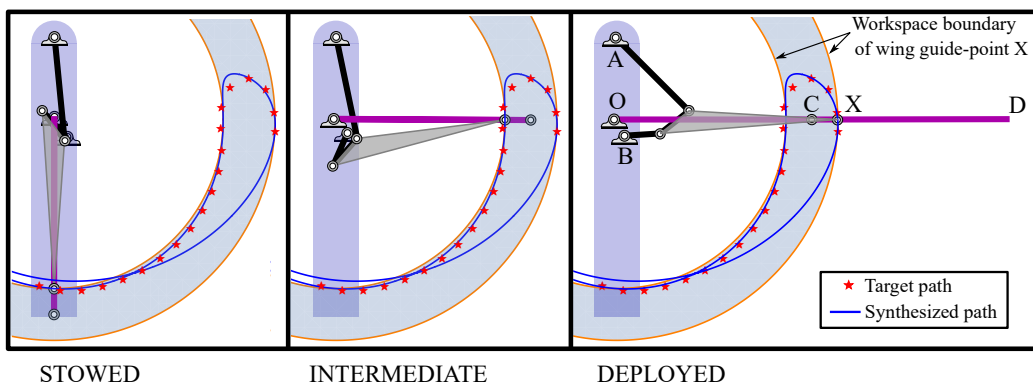


Figure 4.11. Three snapshots, namely, a stowed configuration, an intermediate configuration and a deployed configuration, of deployable aircraft wing mechanism.

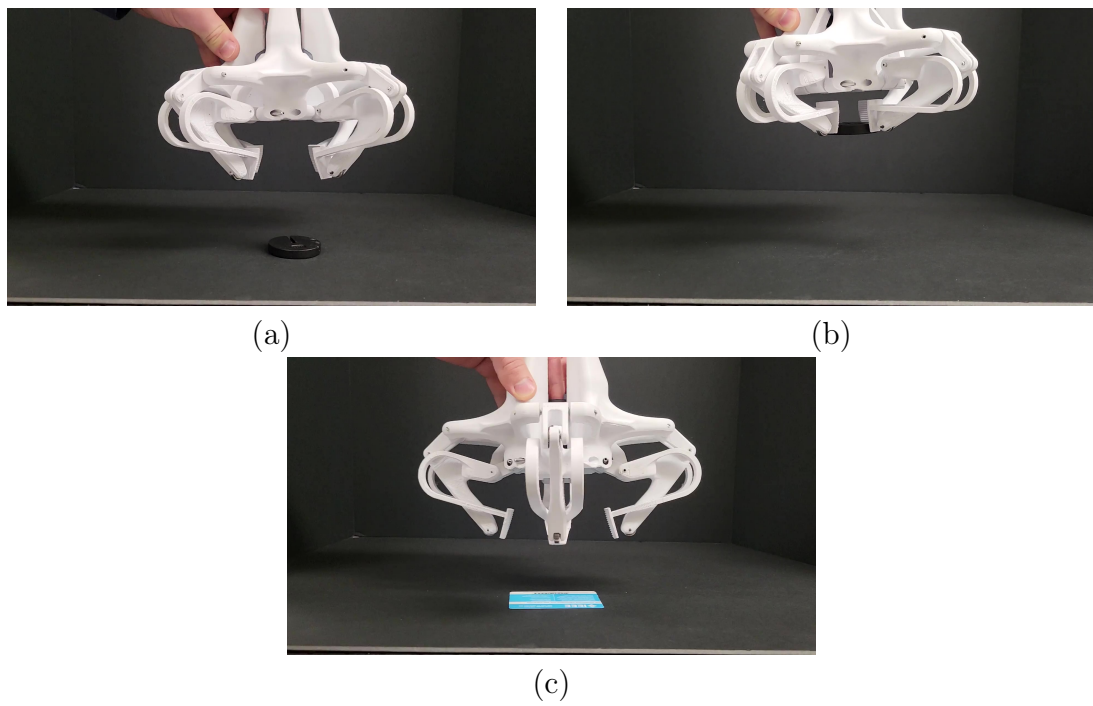


Figure 4.12. (a) The gripper prototype in action. (b) Lifting a 100g weight.
(c) From a side view, preparing to grab a plastic card.

CHAPTER 5

OUTPUT MODES OF A FIVE-BAR MECHANISM

The configuration spaces of parallel manipulators exhibit more nonlinearity than serial manipulators. Qualitatively, they can be seen to possess extra folds. Projection onto smaller spaces of engineering relevance, such as an output workspace or an input actuator space, these folds cast edges that exhibit boundary behavior. For example, inside the global workspace bounds of a five-bar linkage appear several local workspace bounds that only constrain certain output modes of the mechanism. The presence of such boundaries, which manifest in both input and output projections, serve as a source of confusion when these projections are studied exclusively instead of the configuration space itself. Particularly, the design of nonsymmetric parallel manipulators has been confounded by the presence of exotic projections in their input and output spaces. In this paper, we represent the configuration space with a radius graph, then weight each edge by solving an optimization problem using homotopy continuation to quantify transmission quality. We then employ a graph path planner to approximate geodesics between configuration points that avoid regions of low transmission quality. Our methodology automatically generates paths capable of transitioning between non-neighboring output modes, a motion which involves osculating multiple workspace boundaries (local, global, or both). We apply our technique to two nonsymmetric five-bar examples that demonstrate how transmission properties and other characteristics of the workspace can be selected by switching output modes.

5.1 Introduction

The workspaces of parallel mechanisms are more complicated than their serial counterparts. Their interiors generically contain inner bounds of different sorts: either favorable or unfavorable transmission characteristics, or locations where it is possible to transition between different modes of the mechanism. Dealing with such complexity is a burden, but provides opportunity for kinematical advantages. For example, at a single output point, parallel mechanisms can assume a larger selection of configurations that afford more choice of directional transmission characteristics.

More precisely, consider the case where a mechanism’s configuration space is implicitly defined as the set of mechanism parameters which satisfy a set of nonlinear constraints. Various subsets of “singular” configurations which exhibit atypical kinematic characteristics may subsequently be defined as satisfying additional equations. The main challenge reduces to computing paths for transitioning between different modes which avoid problematic configurations, and more generally between any two mechanism configurations. The path planning problem, even polynomial constraints, has time complexity that grows exponentially in the number of parameters (e.g., [10, 31]). Despite this, considerable interest in the problem has correspondingly resulted in a number of proposed methods for singularity-free path planning and analyzing configuration spaces with singularities removed in practical situations, see [22, 23, 32, 64, 82, 93] for a non-exhaustive list. The automatic methods in this list approximate the singularity-free configuration space of a mechanism in various ways, and share a requirement for a user-supplied input sometimes called a *resolution*. The resolution controls how closely the configuration space’s geometry is approximated during path planning. Typical theoretical guarantees show that a method is resolution-complete: “[...] it always returns a path if one exists at a given resolution, or returns ‘failure’ otherwise” [22].

We present here a proof of concept path planning method which integrates recently

developed numerical algebraic geometry [18, 109] approaches to compute geometric feature sizes [38, 43], dense samples [37, 40], and Euclidean distance to singular sets [55]. This yields a deterministic path planner with stronger guarantees than resolution-completeness. For a given input space, there is a correct resolution at which our path planner returns a path if one exists, reports that no path exists otherwise, and the method automatically estimates this resolution in a principled way.

The resulting output is a weighted graph whose nodes are points in the configuration space and edges are weighted by distance in the ambient space. Building a global graph-based model in this fashion is currently more computationally expensive than other proposals. Our approach’s most novel elements however, namely feature size and Euclidean distance-to-singularity computations, are fast and can be integrated with other proposals. The graph models we compute are effective, allowing us to compute shortest paths that closely estimate configuration space geodesics and make repeated queries to investigate the geometry of different modes.

5.2 Background

Let us compare the serial 2R mechanism (Fig. 5.1, left) to a parallel five-bar (Fig. 5.1, right). The workspace of the 2R is an annulus. It can assume two different configurations for every point within its x - y workspace. To transition between these points, the end-effector point must travel to a workspace bound and come back. Placing a rotary actuator at each joint, there are no points in the workspace where the linkage is incapable of exerting a force in any direction. At each point, the selection of configurations and velocity ellipses [81] available are reflections of one another, see Fig. 5.1.

The workspace bounds of a five-bar is a union of two circular arc segments and two four-bar coupler curves. Despite having two degrees-of-freedom, its configuration

space cannot be fully visualized with only two parameters. Therefore, viewing the x - y projection of its configuration space seemingly shows additional interior workspace bounds. To add to the confusion, each internal curve of Fig. 5.1 is relevant only to certain output modes and irrelevant to others. Some of these bounds indicate holes analogous to the annulus while others indicate bounds of specific output modes which serve as places of transition between modes. Scattered within its configuration space are curves at which this linkage loses its ability to exert forces in a direction. These curves as well are only relevant to some output modes but not others. For a regular workspace point, the linkage can assume two or four different configurations, with each exhibiting a different velocity ellipse. To study these configuration spaces, we use the terms *input singularities*, *output singularities*, *input modes*, and *output modes*.

Input singularities. Input singularities are the singular solutions to the forward kinematics problem. They serve as *local* bounds of motion in the input space, e.g. the ϕ - ψ plane (Fig. 5.1). At these bounds, one of the semi-axis lengths of the velocity ellipse in output space tends toward infinity. It is in that direction that the linkage cannot transmit any force at the end-effector no matter the torque exerted by the actuators. Because of this loss of control authority, input singularities are generally considered to have **transmission problems** and should be avoided. For a five-bar linkage, the geometric condition for an input singularity is that points C , D , F , are collinear (Fig. 5.2). The literature also uses the terminology *type II singularity* [48] and *DKP* (direct kinematic problem) *singularity* [118]. *Input singularity* is used in [23], or *forward singularity* to include cases induced by a nonsmooth configuration space.

Output singularities. Output singularities are the singular solutions to the inverse kinematics problem. They serve as *local* bounds of motion in the output space, e.g. the x - y plane (Fig. 5.1). At these bounds, the semi-axis of the velocity ellipse normal to these curves collapses to zero. It is in that direction that the linkage

can sustain any force at the end-effector with zero torque from the actuators. In this way, there are **no transmission problems** at output singularities from the vantage of torque exerted by the actuators. It is at these configurations that the linkage is able to transition output modes. For a five-bar linkage, the geometric condition for an output singularity is that either points A, C, P , or points B, D, F , are collinear (Fig. 5.2). The literature also uses the terminology *type I singularity* [48] and *IKP* (inverse kinematic problem) *singularity* [118]. *Output singularity* is used in [23], or *inverse singularity* to include cases induced by a nonsmooth configuration space.

Input modes. The separated regions that result after partitioning the configuration space by its input singularities are called its input modes. Note that if input singularities do not exist, there may still be more than one input mode, depending on the connectivity of the unpartitioned configuration space. An input mode is a maximal continuous region of configurations whereby a path can be formed between any two regular interior members without passing through an input singularity. The term *assembly mode* appears frequently in past literature. An *input mode* is not an *assembly mode*. As defined in the past, the total number of assembly modes is equal to the number of solutions to the forward kinematics problem, implying the solutions uniquely identify all assembly modes. The total number of input modes could be less than, equal, or greater than the number of assembly modes. One way that it may be less is when a path exists between two forward kinematics solutions that does not pass through an input singularity, hence they are part of the same input mode. Such cases are well documented and illustrate the shortcomings of the term *assembly mode* [65]. The number of input modes is greater than the number of assembly modes when the unpartitioned configuration space already consists of disconnected regions which are further divided by the presence of input singularities.

Output modes. Similarly to input modes, the separated regions that result after partitioning the configuration space by its output singularities are called its output

modes. Note that if output singularities do not exist, there may still be more than one output modes, depending on the connectivity of the unpartitioned configuration space. An output mode is a maximal continuous region of configurations whereby a path can be formed between any two regular interior members without passing through an output singularity. The term *working mode* appears frequently in past literature. An *output mode* is not a *working mode*. As defined in the past, the total number of working modes is equal to the number of solutions to the inverse kinematics problem, implying the solutions uniquely identify all working modes. The total number of output modes could be less than, equal, or greater than the number of working modes. One way that it may be less is when a path exists between two inverse kinematics solutions that does not pass through an output singularity, hence they are part of the same output mode. The number of output modes is greater than the number of working modes when the unpartitioned configuration space already consists of disconnected regions which are further divided by the presence of output singularities.

5.3 Method

Let $C \subset \mathbb{R}^n$ denote the d -dimensional configuration space which is a manifold¹ in the n -dimensional ambient space such that C is defined by the system of $n - d$ polynomial equations $F(z) = 0$ where $z \in \mathbb{R}^n$. Suppose that the set of input singularities I in the configuration space is defined by the polynomial equation $g(z) = 0$ where $z \in C$. For instance, consider the five-bar mechanism as depicted in Fig. 5.2. The dimensions are given by $a_x, a_y, b_x, b_y, l_1, l_2, l_3, l_4, p, q$. For canonical representation, $a_x = a_y = b_y = 0$ can be assumed without loss of generality. The configuration

¹Recall that manifolds do not have self-intersections, cusps, or other geometric singularities.

space is defined by $F(z) = 0$:

$$\begin{aligned}
& x^2 + y^2 - 2l_1(xc_\phi + ys_\phi) + l_1^2 - p^2 - q^2 = 0, \\
& l_2^2(x^2 + y^2) + l_1^2((l_2 - p)^2 + q^2) + (b_x^2 + l_3^2 - l_4^2)(p^2 + q^2) \\
& - 2l_2l_3(p(xc_\psi + ys_\psi) - q(xs_\psi - yc_\psi)) - 2b_xl_2(px + qy) \\
& + 2l_1l_3((l_2p - p^2 - q^2)(c_\phi c_\psi + s_\phi s_\psi) + 2b_xl_3(p^2 + q^2)c_\psi) \\
& + 2b_xl_1((l_2p - p^2 - q^2)c_\phi + l_2qs_\phi) - 2l_1l_2l_3q(c_\phi s_\psi - s_\phi c_\psi) \\
& + 2l_1l_2((p - l_2)(xc_\phi + ys_\phi) - q(xs_\phi - yc_\phi)) = 0, \\
& c_\phi^2 + s_\phi^2 - 1 = 0, \quad c_\psi^2 + s_\psi^2 - 1 = 0,
\end{aligned}$$

where the variables are $z = (x, y, c_\phi, s_\phi, c_\psi, s_\psi)$ with c_ϕ, s_ϕ and c_ψ, s_ψ being the cosine and the sine of ϕ and ψ in order, respectively. Consider our work to take a characteristic length [4] of unity. The replacement of angles with their corresponding cosine and sine along with the Pythagorean identity is a standard approach to yield polynomials and it avoids redundancy related to the periodicity of angles. In particular, other than an increased number of variables and equations, this does not impact the results of path planning.

Let F_1 and F_2 be the first two polynomial functions above. For the five-bar, the set of input singularities I is defined by

$$g(z) = \det \begin{pmatrix} \frac{\partial F_1}{\partial x} & \frac{\partial F_1}{\partial y} \\ \frac{\partial F_2}{\partial x} & \frac{\partial F_2}{\partial y} \end{pmatrix} = 0 \quad \text{for } z \in C.$$

A first measure of the geometric complexity of I is its degree in the ambient space. Generically, for the five-bar, I is a union of two irreducible curves of degree 6. Note that these two curves arise from two four-bar coupler curves.

5.3.1 Sampling and graph construction

The graph construction will follow a straightforward radius graph approach. For $v \in \mathbb{R}^n$, let $\|v\|$ denote the standard Euclidean distance. For $r > 0$, the r -radius graph on a finite set $\hat{C} \subset \mathbb{R}^n$, denoted $G_r(\hat{C})$, is the undirected graph with node set \hat{C} and an edge $e = (c_0, c_1)$ that is weighted by distance $\|c_0 - c_1\|$ for every pair of distinct points $c_0, c_1 \in \hat{C}$ such that $\|c_0 - c_1\| \leq r$.

To model the configuration space C with a radius graph, we require an appropriate finite sample² $\hat{C} \subset C$ and also an appropriate radius $r > 0$. To be more precise regarding the sample, our method first determines an appropriate “resolution” $\epsilon > 0$ and then computes an ϵ -sample of C , \hat{C} , such that every point $c \in C$ is within distance ϵ of a point in \hat{C} .

We can associate to C two geometric feature sizes: the *reach* of C [44], denoted $\text{reach}(C)$, and the *weak feature size* of C [34, 50], denoted $\text{wfs}(C)$. These are numbers which, roughly speaking, quantify the size of the geometric features in C . They are related by $0 < \text{reach}(C) \leq \text{wfs}(C)$. See, e.g., [38, Sec. 2] for an expanded discussion. One can show (e.g., [38, Thm 2.11]) that if $2\epsilon < \text{wfs}(C)$, \hat{C} is an ϵ -sample of C . Moreover, if $r(\epsilon) = 4\epsilon$, then any path of edges in the radius graph $G_{r(\epsilon)}(\hat{C})$ maps continuously onto a path in C and $G_{r(\epsilon)}(\hat{C})$ has the same number of connected components as C . Additionally, if $2\epsilon < \text{reach}(C)$, then for any edge $(c_0, c_1) \in G_{r(\epsilon)}(\hat{C})$, there is a path in C between c_0 and c_1 where the distance $\|c_0 - c_1\|$ is a good estimate for the length of the path. The shortest path graph distance between two points in $G_{r(\epsilon)}(\hat{C})$ is subsequently a good estimate for the shortest path distance in C between the points.

Numerical algebraic geometry methods which use the polynomial system F to de-

²In fact, we can easily relax the requirement $\hat{C} \subset C$ to allow the set \hat{C} to consist of points which are at most distance $\delta > 0$ from C for small δ . For the sake of clarity, we discuss the case where $\delta = 0$.

termine the reach and weak feature size of C have recently been developed [38, 43], as have methods which produce an ϵ -sample of C from F [37, 40]. One advantage of the latter method over, e.g., random sampling, is that we can use geometric subsampling methods to mitigate oversampling while maintaining an appropriate resolution. Verifiably computing feature sizes remains relatively expensive, but there are principled early stopping criteria to estimate³ $\text{wfs}(C)$ inexpensively. In summary, we construct a graph to model C as follows:

1. Compute an estimate W for $\text{wfs}(C)$ using the polynomial system F as input.
2. Compute an ϵ -sample of C , \hat{C} , where $W = 2\epsilon$, using the polynomial system F as input.
3. Construct the radius graph $G_{r(\epsilon)}(\hat{C})$.

5.3.2 Singularity avoidance

An edge in this constructed graph corresponds with a path between two points in the configuration space. To avoid input singularities, one only needs, in theory, to remove edges which correspond to paths that cross the input boundary. Since we cannot check this directly, we instead compute the distance in the ambient space between the set of input singularities and the straight-line segment connecting an edge's two endpoints. This is justified by the heuristic that the straight-line segment between the two points can be taken as a reasonable approximation of the geodesic in the configuration space connecting the two points.

As a brief remark, alternative methods typically use the function $g : \mathbb{R}^n \rightarrow \mathbb{R}$, the determinant defining I , for singularity avoidance directly rather than the distance-to-singularity function. A distinct advantage of using Euclidean distance is that it is, in mathematical terms, 1-Lipschitz continuous. Denoting the function by $d_I : \mathbb{R}^n \rightarrow \mathbb{R}$, we have $|d_I(z_1) - d_I(z_2)| \leq \|z_1 - z_2\|$ for any $z_1, z_2 \in \mathbb{R}^n$. The function g is continuous,

³Following the terminology of [38], we compute only the geometric 2-bottlenecks of C .

but in contrast can easily send nearby inputs to very different values.

Let $c_0, c_1 \in C$ so that the straight-line segment connecting them is $c(t) = (1 - t)c_0 + tc_1$ for $t \in [0, 1]$. Hence, $c(0) = c_0$ and $c(1) = c_1$. We aim to solve

$$\min\{\|c(t) - w\|^2 : w \in I, 0 \leq t \leq 1\}. \quad (5.1)$$

Utilizing the Fritz John first-order necessary conditions, one obtains the polynomial system $J(w, t, \lambda)$ equal to

$$\begin{bmatrix} F(w) \\ g(w) \\ \lambda_0 \nabla_{w,t} (\|c(t) - w\|^2) + \sum_{i=1}^d \lambda_i \nabla_{w,t} (F_i(w)) \\ + \lambda_{d+1} \nabla_{w,t} (g(w)) + \lambda_{d+2} \nabla_{w,t} (t) + \lambda_{d+3} \nabla_{w,t} (1-t) \\ \lambda_{d+2} t \\ \lambda_{d+3} (1-t) \end{bmatrix}$$

where $\lambda \in \mathbb{P}^{d+3}$ and $\nabla_{w,t}(f(w, t))$ is the gradient vector of $f(w, t)$ with respect to w and t for any function f .

Since we aim to solve $J = 0$ for various choices of c_0 and c_1 , we employ a parameter homotopy [87] with c_0 and c_1 as parameters. Thus, the first step is perform an *ab initio* solve of $J = 0$ for generic values of the parameters. Note that the system J has a natural two-homogeneous structure with variables groups (w, t) and λ . Hence, a multihomogeneous homotopy or a multihomogeneous regeneration [59, 62] can be employed for this *ab initio* solve. Then, a parameter homotopy simply deforms from the generic values of the parameter to the given values of c_0 and c_1 . The number of solution paths tracked in this parameter homotopy is precisely the generic number of solutions to $J = 0$. For the five-bar, the two-homogeneous Bézout count of J is 1152 while the actual generic number of solutions to $J = 0$ is 84.

The endpoints of the parameter homotopy correspond with critical points of (5.1) for the given values of c_0 and c_1 . Hence, one can solve (5.1) by sorting through the critical points to determine real critical points on the line segment, i.e., for $t \in [0, 1]$, and selecting the corresponding minimum distance. Moreover, by considering the last two polynomials in J , which correspond to the complimentary slackness condition, one can actually break the computation into three separate pieces: at $t = 0$, at $t = 1$, and along the interior of the line segment, i.e., for $0 < t < 1$. Corresponding parameter homotopies would track 24, 24, and 36 paths, respectively, with $24 + 24 + 36 = 84$. Since many edges in the graph can have the same node, one advantage of breaking this computation into these three separate pieces is to avoid recomputing the same information for repeated nodes.

Performing this computation for every edge e in the constructed graph results in a minimum distance $D(e)$ along that edge to the input singularity and a distance $D(c)$ for every configuration c in the node set \hat{C} . To use the graph for singularity avoidance, i.e., to model the space $C \setminus I$, we then choose a distance threshold T and remove all edges from the graph with $D(e) < T$. Any remaining nodes with no edges are also removed. In principle, one would like to compute a threshold T such that the reduced graph has as many connected components as input modes. This would require a distinct and currently infeasible feature size computation for I as a subspace of the manifold C . At the present, we instead choose $T = r(\epsilon)$ based on simple geometric heuristics. Note, however, that we can also choose T based on engineering considerations. Singularity-avoiding path planning queries can be subsequently performed by shortest path computations in this graph, e.g., with A^* path planning [54] using the Euclidean distance in ambient space between two configurations as a heuristic.

5.3.3 Computational considerations

A full computational complexity analysis is beyond the scope of this work, but we include here some heuristics for consideration as well as order-of-magnitude timing information from an implemented version of the method applied to the two examples in Section 5.4. Most computations were performed on a 24 CPU Intel Xeon E5-2680 at 2.50GHz.

Estimating $\text{wfs}(C)$. This is a homotopy continuation computation with costs one expects to increase based on the number of variables n , codimension $n - d$ of C , and degree of the polynomials in F increase. In Section 5.4, $n = 6$ with codimension 4 and degree of the polynomials is 2. Estimating $\text{wfs}(C)$ for Example 2 in Section 5.4 with 24 cores required approximately 6 minutes. These computations are easily parallelizable and so can readily utilize additional CPUs.

Computing an ϵ -sample. This procedure relies upon homotopy continuation methods that also scale in the number of variables, codimension of C , and degree of the polynomials in F . Costs also increase with the number of sample points. Heuristically, one expects the number of sample points to scale with $(\frac{\text{vol}_d(C)}{W})^d$ where $\text{vol}_d(C)$ is the d -dimensional Hausdorff measure of C . For additional experimental results regarding the number of points, see [37]. With 24 CPU cores, the examples in Section 5.4 required approximately a day of computation. Subsequently, computing a radius graph from the sample required on the order of minutes.

Computing the input boundary distance $D(e)$. For a single edge e , computing $D(e)$ is a homotopy continuation computation with similar considerations to those previously discussed. For example, using a single core, a typical edge computation for Example 2 in Section 5.4 required 0.8 seconds. The implementation used for this manuscript computes $D(e)$ for every edge e in the computed radius graph, which scales with the number of points in the sample. Computations for each edge can easily be done in parallel. Moreover, the same example required approximately 11.75

hours to compute $D(e)$ for 3.2×10^6 edges using 6 servers, each with either 24 or 32 CPUs. Note that, after an initial step computing minimum distances from the graph nodes to the singularity set, one may use that information to forego computing $D(e)$ for any edge e with endpoints sufficiently far away from I relative to the singularity avoidance threshold T .

5.4 Results

The methodologies described above were applied to two examples of nonsymmetric five-bar linkages. Their parameters are listed in Table 5.1 with Table 5.2 summarizing the size of the graphs computed. Both examples involve traversing across non-neighboring output modes while maintaining the same input mode. In other words, output singularities are crossed and input singularities are not.

5.4.1 Perpendicular velocity ellipses at an x - y point

The first example five-bar possesses a point in its workspace where two of the four IKP solutions exhibit velocity ellipses with a 4:1 aspect ratio that are perpendicular to each other. Its dimensions were found using the method reported in [97]. The direction of the short axis benefits from $4\times$ larger force transmission while the direction of the long axis can achieve $4\times$ greater speeds. The configurations corresponding to these perpendicular velocity ellipses are housed in different output modes. The path planning challenge is to approximate the geodesic from one to the other, which in this case involves transitioning through at least two output singularities. A feasible path designed using our methodology for this challenge is shown in Fig. 5.4.

At the computed singularity avoidance threshold, the graph model of the configuration space estimated 6 input modes, 5 output modes, and 7 input/output modes (maximal regions bounded by both input and output singularities). Due to the numerical threshold, our counts generally do not match the true number of regions, as

they partition the configuration space with a thicker kerf, so to say. In some respects, this is more practical as input singularities should be avoided by a margin of safety. To give some idea of the space's extrinsic curvature, the distance in ambient space between the two configurations of interest is 2.11, the shortest path in the configuration space estimated by our method without input singularity avoidance is 2.66, and the shortest point with input singularity avoidance is 2.74.

5.4.2 A ceiling and a floor

The second example five-bar possesses an output mode where there exists an arc that serves as a local upper bound for the y -coordinate of the end-effector, referred to as a *ceiling*. The same five-bar also possesses another output mode where there exists another arc, nearly on top of the first arc, but now functioning as a local lower bound for the y -coordinate of the end-effector, referred to as a *floor*. The path planning challenge is to transition from the output mode with a ceiling to the output mode with a floor. This could be useful because, at an output bound, the mechanism is able to support large loads in the bound's normal direction without any actuator effort. However, as it is a bound, regular motions can only take place on one side, locally. By transitioning between a ceiling and a floor, the side of regular motion becomes selectable. Figure 5.6 shows a feasible path designed using the methodology presented for this example.

Our method estimated 5 input modes, 3 output modes, and 12 input/output modes. The ambient distance between the configuration in Fig. 5.6 was 2.61 and the path distance both with and without input singularity avoidance was 4.82. The two paths distances are the same since the computed path does not come particularly close to an input singularity.

5.5 Conclusions

This paper presented a motion planning technique for transitioning between points in the configuration space of a five-bar manipulator. This is a challenging task since the input and output singularities of parallel manipulators appear in a complicated manner. To overcome this, we constructed a radius graph to represent the workspace with edges weighted by nearness to input singularities. The graph is partitioned into input modes and a path planner is employed to approximate geodesics between start and final points that avoid input singularities. The resulting algorithm is able to traverse through multiple output modes in a smooth manner as demonstrated with two examples.

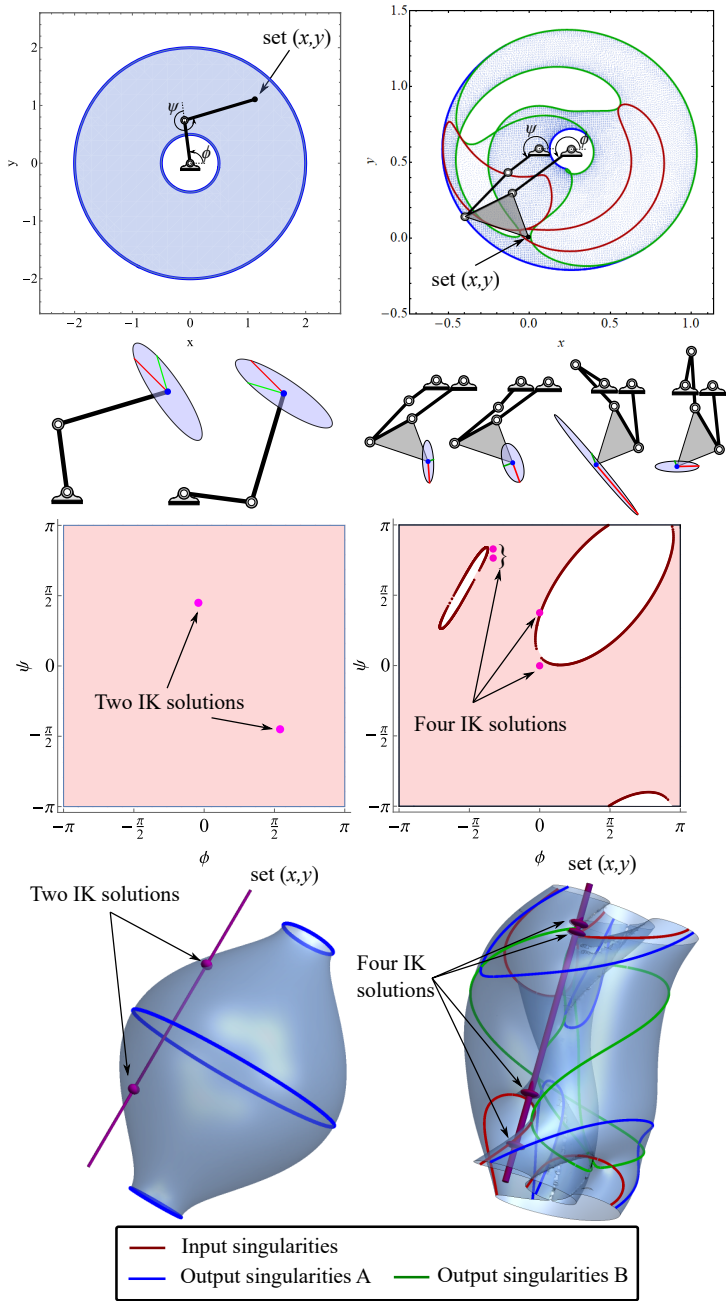


Figure 5.1. Views of the configuration spaces of a serial 2R (left) and a parallel five-bar (right). 1st row: The output workspace for each manipulator. 2nd row: The 2R admits two IK solutions, the five-bar admits four. 3rd row: The input actuator space for each manipulator, with holes visible for the five-bar. 4th row: An (x, y, ψ) view of the configuration manifold. The skewering line shows the locations of the IK solutions for a set (x, y) .

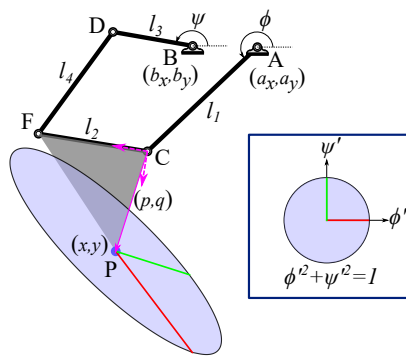


Figure 5.2. Schematic of a five-bar mechanism. The velocity ellipse with respect to the input angles ϕ and ψ is shown at its end-effector (x, y) .

TABLE 5.1
FIVE-BAR DIMENSIONS FOR THE TWO EXAMPLES

Example	a_x	b_x	p	l_1	l_2
1	0.259	0.060	0.049	0.465	0.349
2	0.066	-0.642	0.298	0.775	0.832

Example	a_y	b_y	q	l_3	l_4
1	0.586	0.590	0.328	0.249	0.411
2	0.815	0.845	1.304	0.291	0.522

TABLE 5.2
SUMMARY OF THE RADIUS GRAPHS FOR THE TWO EXAMPLES

Example	# pts in graph	# edges in graph
1	82,581	2.3×10^6
2	121,667	3.2×10^6

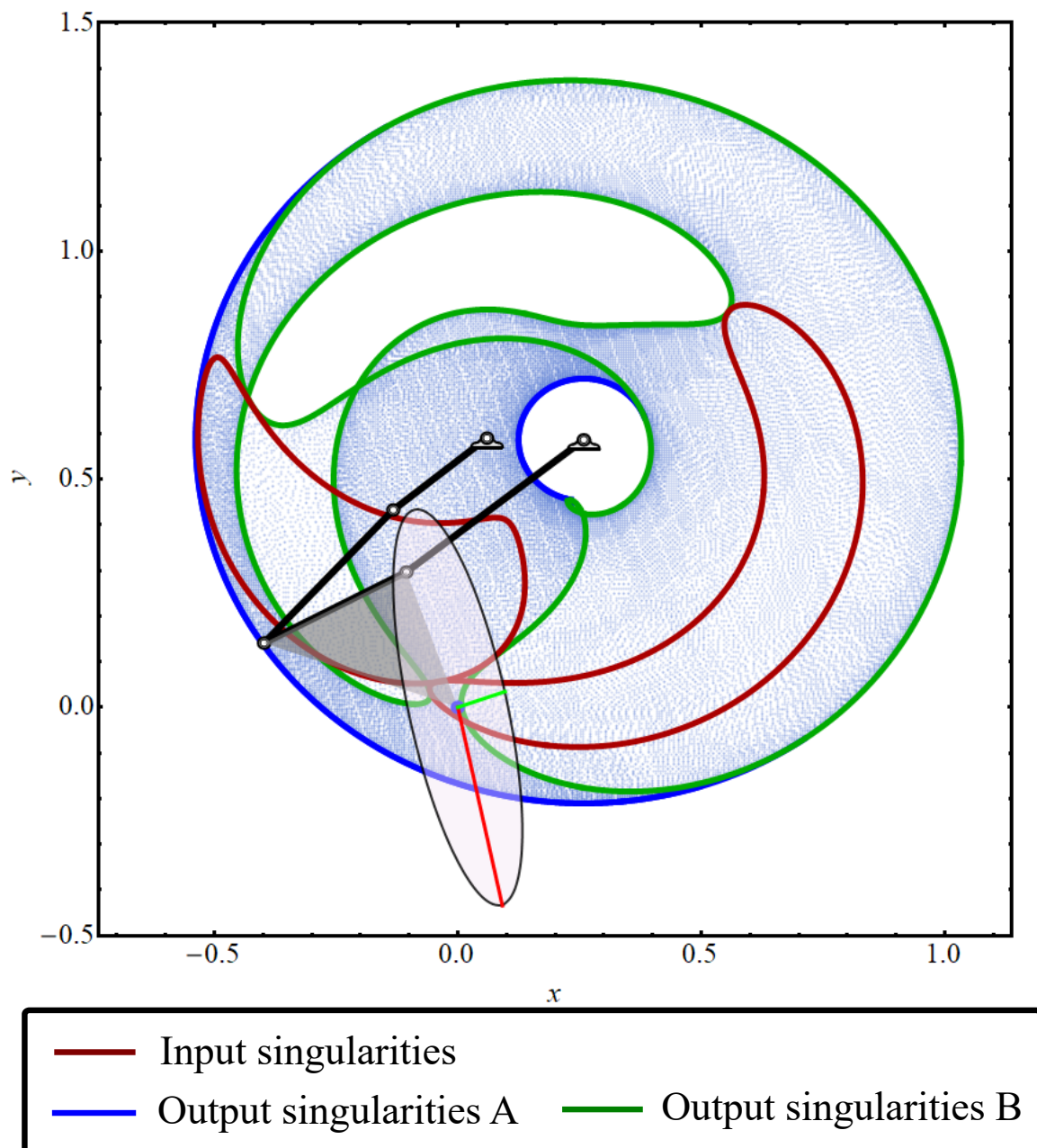


Figure 5.3. Example 1: At the x - y point shown, there exists another configuration with a velocity ellipse perpendicular to the one displayed.

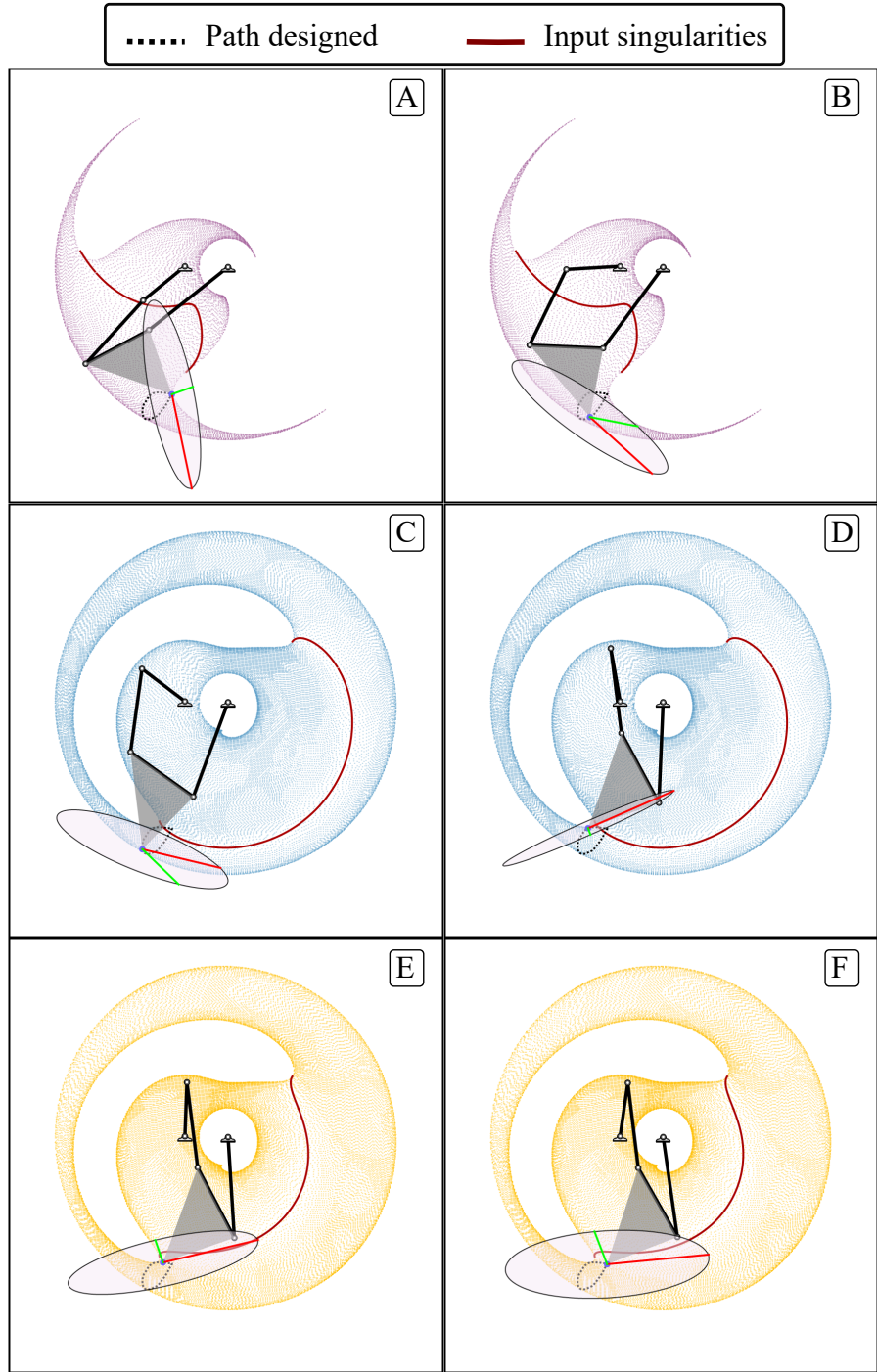


Figure 5.4. Example 1: A feasible path marked with six snapshots, marked alphabetically from A to E, to switch between the configurations corresponding to two perpendicular velocity ellipses. The workspace and the input singularity curves shown correspond to the output mode to which each configuration belongs. Output modes are distinguished by color.

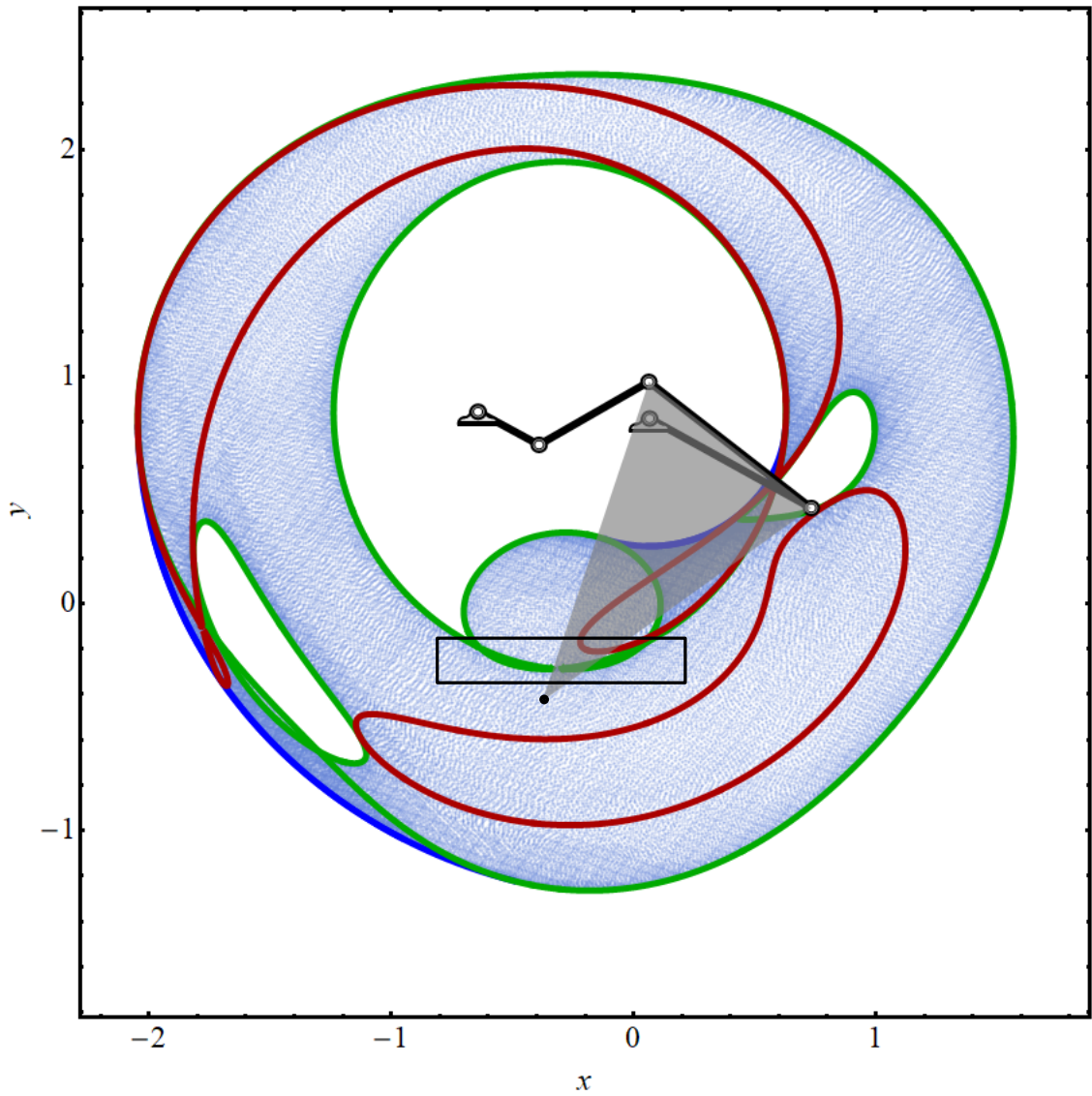


Figure 5.5. Example 2: The portion of the output bound which functions as a ceiling or floor is indicated with a box.

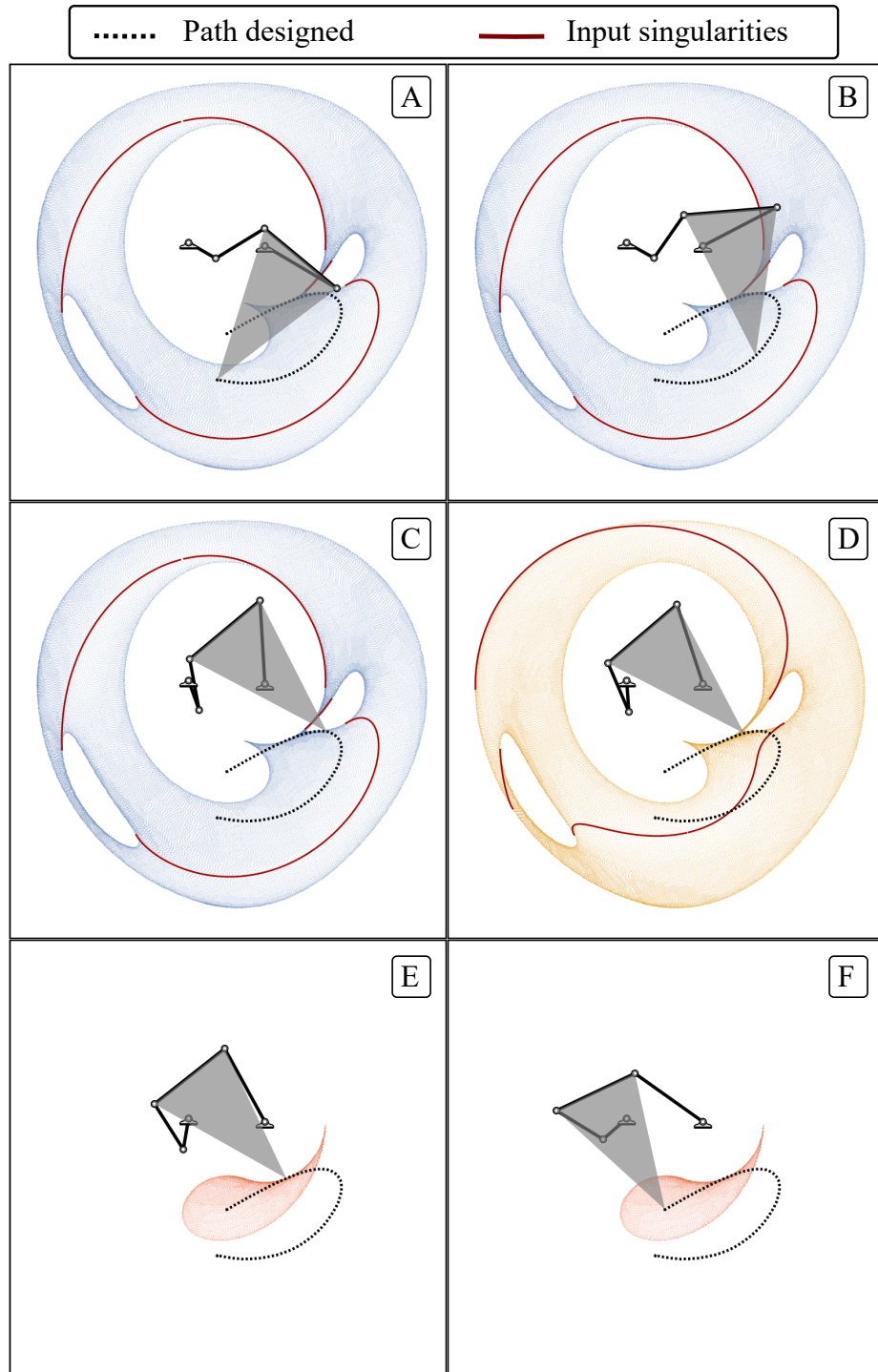


Figure 5.6. Example 2: A feasible path marked with six snapshots, marked alphabetically from A to E, for the ceiling-to-floor example. The workspace and the input singularity curves shown correspond to the output mode to which each configuration belongs. Output modes are distinguished by color.

APPENDIX A

KINEMATIC DERIVATIONS

A.1 Four-Bar Mechanism

Kinematic has three main problems

- Forward Kinematics - known mechanism dimensions and input angles, unknown output coordinate
- Inverse Kinematics - known mechanism dimensions and output coordinate, unknown input angles
- Synthesis - known output coordinates, unknown mechanism dimensions and input coordinates

This appendix serves to illustrate one means of deriving the systems for the above problems in planar kinematics.

Let the ground pivots $A_0, B_0 \in \mathbb{C}^2$ be complex numbers with real-valued components such that $A_0 = a_{0x} + a_{0y}i$ and $B_0 = b_{0x} + b_{0y}i$ where $a_{0x}, a_{0y}, b_{0x}, b_{0y} \in \mathbb{R}$ and $i = \sqrt{-1}$. These coordinates can be expressed as 2×1 column vectors, i.e.

$$A_0 = \begin{bmatrix} a_{0x} \\ a_{0y} \end{bmatrix}$$
 Similarly define the other two pivots and coupler point $C_0, D_0, X_0 \in \mathbb{C}^2$ with their respective angular displacements ϕ, ψ , and θ , measured in degrees.

Note that $R = \text{RotationMatrix}(\theta)$ is the 2×2 Euler matrix
$$\begin{bmatrix} \cos(\theta) & -\sin(\theta) \\ \sin(\theta) & \cos(\theta) \end{bmatrix}$$
 rotating about the z -axis. Define a rotation of θ degrees as $R_\theta = \text{RotationMatrix}(\theta)$.

For an example of this matrix expression, refer to [67].

Each of these problems starts with consideration of either the kinematic closed loop equation Eqn. 2.10 or the coupler equations Eqns. 2.11a and 2.11b. This ap-

pendix considers the angle ϕ to be the actuated angle driving motion and force of the mechanism.

A.1.1 Forward kinematics

To solve the forward kinematic expression for a four-bar mechanism with actuated joint A_0 we start with the loop equation with the unknown variables in bold.

$$A_0 + R_\phi(C_0 - A_0) + \mathbf{R}_\theta(D_0 - C_0) = B_0 + \mathbf{R}_\psi(D_0 - B_0) \quad (\text{A.1})$$

First, we isolate the angle with the coupler point, θ , and take dot products, noting that the dot product of a rotation matrix with itself is the identity matrix. Let $\delta = B_0 - A_0 - R_\phi(C_0 - A_0)$ then

$$(D_0 - C_0) \cdot (D_0 - C_0) = \delta \cdot \delta + 2\delta \cdot (R_\psi(D_0 - B_0)) + (D_0 - B_0) \cdot (D_0 - B_0) \quad (\text{A.2})$$

Expand the matrix multiplications in Eqn. A.2 and move all terms to one side to get

$$\begin{aligned} & 2\delta \cdot (D_0 - B_0) \cos(\psi) + 2 \begin{bmatrix} \delta_y \\ -\delta_x \end{bmatrix} (D_0 - B_0) \sin(\psi) + \\ & (D_0 - B_0) \cdot (D_0 - B_0) - (D_0 - C_0) \cdot (D_0 - C_0) + \delta \cdot \delta = 0 \end{aligned} \quad (\text{A.3})$$

Let $\alpha = 2\delta \cdot (D_0 - B_0)$, $\beta = 2 \begin{bmatrix} \delta_y \\ -\delta_x \end{bmatrix}$ $(D_0 - B_0)$, and $\gamma = (D_0 - B_0) \cdot (D_0 - B_0) - (D_0 - C_0) \cdot (D_0 - C_0) + \delta \cdot \delta$. Then this is a phase offset equation $\alpha \cos(\psi) + \beta \sin(\psi) = -\gamma$ of which $\psi = \arctan(\beta/\alpha) \pm \arccos\left(\frac{-\gamma}{\sqrt{\alpha^2 + \beta^2}}\right)$. Since \arccos admits two solutions (one in the first quadrant and one in second quadrant as shown in Fig. A.1), the \pm specifies which solution we aim to take, commonly referred to as “leg up” or “leg

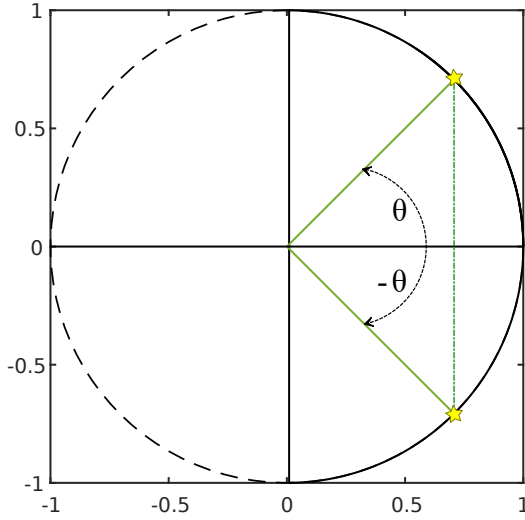


Figure A.1. The function $\arccos(\theta) = x$ is shown in the solid line along the circle; there are two solutions on the circle per value of θ .

down” configurations.

Now, with our computed value for ψ , we can plug it back into Eqn. A.1 to solve for θ . Note

$$R_\theta \begin{bmatrix} x \\ y \end{bmatrix} = \begin{bmatrix} x \cos(\theta) - y \sin(\theta) \\ x \sin(\theta) + y \cos(\theta) \end{bmatrix} = \begin{bmatrix} x & -y \\ y & x \end{bmatrix} \begin{bmatrix} \cos(\theta) \\ \sin(\theta) \end{bmatrix} \quad (\text{A.4})$$

Which simplifies to

$$\begin{bmatrix} \cos(\theta) \\ \sin(\theta) \end{bmatrix} = \begin{bmatrix} (D_0 - C_0)_x & -(D_0 - C_0)_y \\ (D_0 - C_0)_y & (D_0 - C_0)_x \end{bmatrix}^{-1} (\delta + R_\psi(D_0 - B_0)) \quad (\text{A.5})$$

Then $\theta = \arctan\left(\frac{\sin(\theta)}{\cos(\theta)}\right)$.

This derivation is generalized into a computer-friendly algorithm for computing the end-effector position X and the intermediary angles for a displacement angle ϕ

on the actuated pivot A_0 .

Algorithm 1 Four Bar Forward Kinematics Equation

Input: $\{A_0, B_0, C_0, D_0, X_0, \phi, \pm_1\}$

Output: $\{X, \psi, \theta\}$

$$Q \leftarrow \text{RotationMatrix}(\phi)$$

$$\delta := \begin{bmatrix} \delta_x \\ \delta_y \end{bmatrix} = B_0 - A_0 - Q \cdot (C_0 - A_0) \quad \{\cdot \text{ is the dot product operator}\}$$

$$\alpha = 2(D_0 - B_0) \cdot \begin{bmatrix} \delta_x \\ \delta_y \end{bmatrix}$$

$$\beta = 2(D_0 - B_0) \cdot \begin{bmatrix} \delta_y \\ \delta_x \end{bmatrix}$$

$$\gamma = \delta \cdot \delta - (D_0 - C_0) \cdot (D_0 - C_0) + (D_0 - B_0) \cdot (D_0 - B_0)$$

$$\psi = \arctan\left(\frac{\beta}{\alpha}\right) \pm_1 \arccos\left(\frac{-\gamma}{\sqrt{\alpha^2 + \beta^2}}\right)$$

$$\epsilon = \begin{bmatrix} d_{0x} - c_{0x} & d_{0y} - c_{0y} \\ -(d_{0y} - c_{0y}) & d_{0y} - c_{0x} \end{bmatrix} \cdot (B_0 - A_0 - Q \cdot (C_0 - A_0) + S \cdot (D_0 - B_0))$$

$$\theta = \arctan\left(\frac{\epsilon_y}{\epsilon_x}\right)$$

$$X = A_0 + Q \cdot (C_0 - A_0) + T \cdot (X_0 - C_0)$$

The coupler curve then can be parameterically plotted by Alg. 2 for $\phi \in [0, 2\pi]$ either the “leg up” or “leg down” configuration. Note, the actuated pivot is not guaranteed to do a complete rotation but we can still plot $\phi \in [0, 2\pi]$ due to the periodicity of the mechanism movements. Grashof’s condition states that a four-bar with link lengths $\ell = \{l_1, l_2, l_3, l_4\}$, where l_4 is the ground link, will have a complete 360° on the actuated pivot, known as the *crank*, if the following condition holds

$$\max(\ell) + \min(\ell) < \text{sum of the other two link lengths.}$$

For more information on mechanism classifications, refer to [81].

A.1.2 Inverse kinematics

Complementary to forward kinematics are inverse kinematic equations. Inverse kinematics solves for the dimensions of a mechanism given a specified precision point and input angles. These problems are utilized in synthesis, including motion and path synthesis but this derivation will focus on the latter. This derivation will be concerned with deriving the system for exact synthesis, of which a system is derived to be solved simultaneously.

As noted in previous chapters, working in isotropic coordinates offers great numerical advantages. Therefore, this derivation takes $R_\phi = e^{\phi i}$ and so on for the other mechanism angles.

We start with the coupler point equations for a precision point X_j with the unknown variables in bold.

$$\mathbf{A}_0 + R_{\phi_j}(\mathbf{C}_0 - \mathbf{A}_0) + \mathbf{R}_{\theta_j}(X_0 - \mathbf{C}_0) = X_j \quad (\text{A.6a})$$

$$\mathbf{B}_0 + R_{\psi_j}(\mathbf{D}_0 - \mathbf{B}_0) + \mathbf{R}_{\theta_j}(X_0 - \mathbf{D}_0) = X_j \quad (\text{A.6b})$$

Consider the first equation starting with ground pivot A_0 ; we will rearrange the equation as

$$R_{\phi_j}(C_0 - A_0) = X_j - A_0 - R_{\theta_j}(X_0 - C_0) \quad (\text{A.7})$$

Since these are defined isotropically, we simplify Eqn. A.7 by multiplying both sides by their complex conjugates which, noting $R_\theta R_{\theta}^{-1} = 1$, simplifies to

$$(C_0 - A_0)(\bar{C}_0 - \bar{A}_0) = (X_j - A_0 - R_{\theta_j}(X_0 - C_0))(\bar{X}_j - \bar{A}_0 - \bar{R}_{\theta_j}(X_0 - \bar{C}_0)) \quad (\text{A.8})$$

Expanding the right hand side gives the monomial set $\{A_0\bar{C}_0, \bar{A}_0C_0, A_0C_0, \bar{A}_0\bar{C}_0$ or a degree 2 polynomial equation that is linear in $R_{\theta_j}, \bar{R}_{\theta_j}$.

We can do an equivalent derivation with the coupler equation in Eqn. A.6b. This

gives us system of $2j$ equations consisting of the j - “A” and j - “B” side equations that both admit unknown R_{θ_j} values, hence the need to solve this system simultaneously. This can be written as the symbolic matrix

$$\begin{bmatrix} a & b \\ c & d \end{bmatrix} \begin{bmatrix} R_{\theta_j} \\ \bar{R}_{\theta_j} \end{bmatrix} = \begin{bmatrix} -e \\ -f \end{bmatrix}, \quad j = 1, 2, \dots$$

A.2 Five-Bar Mechanism

Five-bar mechanisms have a foundation, literally, of a four-bar mechanism. Unsurprisingly, the kinematic equations of a five bar follow a similar derivation to that of a four-bar’s. Since a four-bar sub-system is needed to solve for the location of pivot F , one sees within Alg. 2 similar steps.

A.2.1 Forward kinematics

We begin with the loop equations, admitting a similar system to that of the four-bar forward kinematics derivation previously described again with the unknown variables bolded.

$$A_0 + R_\phi(C_0 - A_0) + \mathbf{R}_\rho(F_0 - C_0) = B_0 + R_\psi(D_0 - B_0) + \mathbf{R}_\theta(F_0 - D_0) \quad (\text{A.9})$$

We isolate one of the unknown angles, ρ , and dot produce each side with itself, letting $\delta = \delta = A_0 - B_0 + R_\phi \cdot (C_0 - A_0) - R_\psi \cdot (D_0 - B_0)$ and $\mathcal{I} = \begin{bmatrix} 0 & -1 \\ 1 & 0 \end{bmatrix}$

$$(F_0 - C_0)(F_0 - C_0) = \delta \cdot \delta + 2\delta(F_0 - D_0)\cos(\theta) + 2\delta\mathcal{I}(F_0 - D_0)\sin(\theta) \quad (\text{A.10})$$

Which we move all terms to one side and solve for θ via the phase shift equation. We can use θ to solve for our coupler point X . From this, we are only left with

the unknown ρ which we solve through back substitution of the coupler equation
 $A_0 + R_\phi(C_0 - A_0) + R_\rho(X_0 - C_0) = X$.

Algorithm 2 Five Bar Forward Kinematics Equation

Input: $\{A_0, B_0, C_0, D_0, F_0, X_0, \phi, \psi, \pm_1\}$

Output: $\{X, \theta, \rho\}$

$$\begin{aligned}
R_\phi &\leftarrow \text{RotationMatrix}(\phi) \\
R_\psi &\leftarrow \text{RotationMatrix}(\psi) \\
\mathcal{I} &\leftarrow \begin{bmatrix} 0 & -1 \\ 1 & 0 \end{bmatrix} \\
\delta &= A_0 - B_0 + R_\phi \cdot (C_0 - A_0) - R_\psi \cdot (D_0 - B_0) \\
\alpha &= 2\delta \cdot (D_0 - B_0) \\
\beta &= 2\delta \cdot \mathcal{I} \cdot (D_0 - B_0) \\
\gamma &= \delta \cdot \delta - (F_0 - C_0) \cdot (F_0 - C_0) - (F_0 - D_0) \cdot (F_0 - D_0) \\
\rho &= \arctan\left(\frac{\beta}{\alpha}\right) \pm_1 \arccos\left(\frac{-\gamma}{\sqrt{\alpha^2 + \beta^2}}\right) \\
R_\rho &\leftarrow \text{RotationMatrix}(\rho) \\
\epsilon &= \begin{bmatrix} F_0 - D_0 \\ \mathcal{I} \cdot (F_0 - D_0) \end{bmatrix} \cdot (\delta + R_\rho \cdot (F_0 - C_0)) \\
\theta &= \arctan\left(\frac{\epsilon_y}{\epsilon_x}\right) \\
X &= A_0 + R_\phi \cdot (C_0 - A_0) + R_\rho \cdot (X_0 - C_0)
\end{aligned}$$

A.2.2 Inverse kinematics

We begin with the coupler equations, admitting a similar system to that of the four-bar inverse kinematics derivation previously described with the unknown variables in bold.

$$A_0 + \mathbf{R}_\phi(C_0 - A_0) + \mathbf{R}_\rho(F_0 - C_0) = X \quad (\text{A.11})$$

We solve for ϕ in a similar manner as the four-bar, and back substitute to find ρ .

Algorithm 3 Five Bar Inverse Kinematics Equation

Input: $\{A_0, B_0, C_0, D_0, F_0, X_0, X, \pm_1, \pm_2\}$

Output: $\{\phi, \psi, \theta, \rho\}$

$$\mathcal{I} \leftarrow \begin{bmatrix} 0 & -1 \\ 1 & 0 \end{bmatrix}$$

$$\delta = A_0 - B_0 + R_\phi \cdot (C_0 - A_0) - R_\psi \cdot (D_0 - B_0)$$

$$\alpha = 2(X - A_0) \cdot (C_0 - A_0)$$

$$\beta = 2(X - A_0) \cdot \mathcal{I} \cdot (C_0 - A_0)$$

$$\gamma = (X_0 - C_0) \cdot (X_0 - C_0) - (X - A_0) \cdot (X - A_0) - (C_0 - A_0) \cdot (C_0 - A_0)$$

$$\psi = \arctan\left(\frac{\beta}{\alpha}\right) + \pm_1 \arccos\left(\frac{-\gamma}{\sqrt{\alpha^2 + \beta^2}}\right)$$

$$R_\phi = \text{RotationMatrix}(\phi)$$

$$\epsilon = \begin{bmatrix} X_0 - C_0 \\ \mathcal{I} \cdot (X_0 - C_0) \end{bmatrix} \cdot (X - A_0 - R_\phi \cdot (C_0 - A_0))$$

$$\rho = \arctan\left(\frac{\epsilon_y}{\epsilon_x}\right)$$

$$R_\rho \leftarrow \text{RotationMatrix}(\rho)$$

$$\delta = X - B_0 + R_\rho \cdot (F_0 - X_0)$$

$$\alpha = 2\delta \cdot (D_0 - B_0)$$

$$\beta = 2\delta \cdot (\mathcal{I} \cdot (D_0 - B_0))$$

$$\gamma = \arctan\left(\frac{\beta}{\alpha}\right) + \pm_2 \arccos\left(\frac{-\gamma}{\sqrt{\alpha^2 + \beta^2}}\right)$$

$$R_\psi = \text{RotationMatrix}(\psi)$$

$$\epsilon = \begin{bmatrix} F_0 - D_0 \\ \mathcal{I} \cdot (F_0 - D_0) \end{bmatrix} \cdot (\delta - R_\psi \cdot (D_0 - B_0))$$

$$\theta = \arctan\left(\frac{\epsilon_y}{\epsilon_y}\right)$$

APPENDIX B

COGNATE TRANSFORMS AND SOLUTION VALUES FOR CHAPTER 4

B.1 Cognate Transformations for the General Case Formulation

For the four-bar represented in Fig. 4.2 with design variables

$\mathbf{v}_1 = \{A, A^*, B, B^*, l_1, l_2, l_3, Q, Q^*\}$, the two other Roberts' cognates can be computed with the following cognate transformations:

$$\begin{aligned}\mathbf{v}_2 &= \left\{ B, B^*, A + Q(B - A), A^* + Q^*(B^* - A^*), l_2\sqrt{(1 - Q)(1 - Q^*)}, \right. \\ &\quad \left. l_3\sqrt{(1 - Q)(1 - Q^*)}, l_1\sqrt{(1 - Q)(1 - Q^*)}, \frac{1}{1 - Q}, \frac{1}{1 - Q^*} \right\}, \\ \mathbf{v}_3 &= \left\{ A + Q(B - A), A^* + Q^*(B^* - A^*), A, A^*, l_3\sqrt{QQ^*}, l_1\sqrt{QQ^*}, \right. \\ &\quad \left. l_2\sqrt{QQ^*}, \frac{Q - 1}{Q}, \frac{Q^* - 1}{Q^*} \right\}.\end{aligned}$$

Additionally, symmetric representation arising from relabeling of \mathbf{v}_1 is

$$\mathbf{v}'_1 = \{B, B^*, A, A^*, l_3, l_2, l_1, 1 - Q, 1 - Q^*\}.$$

The three Roberts' cognates and their symmetric representations yield $3 \cdot 2 = 6$ members to a group.

B.2 Cognate Transformations for the Pre-specification of One Ground Pivot

For the four-bar represented in Fig. 4.2 design variables

$\mathbf{v}_1 = \{A, A^*, B, B^*, l_1, l_2, l_3, Q, Q^*\}$ such that $B = B^* = 0$, the Roberts' cognate that

preserves the location of the fixed pivot can be computed as \mathbf{v}'_2 via B.1. Thus, there are 2 members to a group.

B.3 Design Positions and Parameters for the Applied Examples

The applied example for the general case used the continuous form of the moment parameters. The values used for the computation of the moments were derived from a recreation of the 6-bar kinematics and an interpolated and integration of the coupler curve. The resulting moments as described in Section 4.3 are given in Table B.1

Tables B.2 and B.3 list the design positions for the applied examples in Section 4.4 and 4.5 with one ground pivot and both ground pivots pre-specified, respectively. In these tables, x is the real part and y is the imaginary part of the design positions. Note the points' respective complex conjugates are similar except for an opposite sign on the imaginary component.

B.4 Solution Values for the Applied Examples

The applied example solutions were evaluated by varied metrics. As the most optimal solution in cost may not always give the optimal design in terms of feasibility or aesthetics, it is important to consider other solutions, including saddle point solutions. The tables given in this section display the ten solutions with the lowest cost value. The real-value leg length variables are provided, one can employ the transformations given in Section 4.2.1 to compute the transformed variables. Additionally, maximum deviation between the design positions and solution path is provided as another metric to assess the solution goodness.

TABLE B.1
 NUMERICAL VALUES OF THE 47 CONTINUOUS MOMENTS OF
 THE GENERAL CASE APPLIED EXAMPLE.

$g_1 =$	$-0.201+0.571i$	$g_{17} =$	$-0.0713+0.129i$	$g_{33} =$	$-0.0274+0.0431i$
$g_2 =$	$-0.251-0.263i$	$g_{18} =$	$-0.0518-0.0933i$	$g_{34} =$	$-0.0163-0.0361i$
$g_3 =$	$0.224-0.0390i$	$g_{19} =$	$0.0786+0.00649i$	$g_{35} =$	$-0.0475+0.102i$
$g_4 =$	$-0.0713+0.137i$	$g_{20} =$	$-0.0375+0.0459i$	$g_{36} =$	$-0.0544-0.0781i$
$g_5 =$	$-0.0475-0.102i$	$g_{21} =$	$0.224+0.0390i$	$g_{37} =$	$0.0786-0.00649i$
$g_6 =$	$0.0824+0.0164i$	$g_{22} =$	$-0.106+0.155i$	$g_{38} =$	$-0.0281+0.0575i$
$g_7 =$	$-0.201-0.571i$	$g_{23} =$	$-0.0713-0.129i$	$g_{39} =$	$-0.0274-0.0431i$
$g_8 =$	$0.417+0.000i$	$g_{24} =$	$0.112+0.000i$	$g_{40} =$	$0.0404+0.000i$
$g_9 =$	$-0.119+0.252i$	$g_{25} =$	$-0.0438+0.0723i$	$g_{41} =$	$-0.0174+0.0266i$
$g_{10} =$	$-0.106-0.155i$	$g_{26} =$	$-0.0281-0.0575i$	$g_{42} =$	$0.0823-0.0164i$
$g_{11} =$	$0.131-0.00107i$	$g_{27} =$	$0.0483+0.00655i$	$g_{43} =$	$-0.0238+0.0669i$
$g_{12} =$	$-0.0544+0.0780i$	$g_{28} =$	$-0.0713-0.137i$	$g_{44} =$	$-0.0375-0.0459i$
$g_{13} =$	$-0.0238-0.0669i$	$g_{29} =$	$0.131+0.00107i$	$g_{45} =$	$0.0483-0.00655i$
$g_{14} =$	$-0.251+0.263i$	$g_{30} =$	$-0.0518+0.0933i$	$g_{46} =$	$-0.0163+0.0361i$
$g_{15} =$	$-0.119-0.252i$	$g_{31} =$	$-0.0438-0.0723i$	$g_{47} =$	$-0.0173-0.0266i$
$g_{16} =$	$0.204+0.000i$	$g_{32} =$	$0.0659+0.000i$		

TABLE B.2
 DESIGN POSITIONS OF THE APPLIED EXAMPLE FOR THE
 PRE-SPECIFICATION OF ONE GROUND PIVOT FORMULATION.

#	x	y	#	x	y
1	0.364598	-1.05667	11	0.341038	-0.838013
2	0.365320	-1.03455	12	0.331590	-0.818017
3	0.365531	-1.01242	13	0.319373	-0.799592
4	0.365220	-0.990290	14	0.304292	-0.783430
5	0.364353	-0.968177	15	0.286853	-0.769836
6	0.362873	-0.946096	16	0.267863	-0.758491
7	0.360690	-0.924074	17	0.248001	-0.748736
8	0.357669	-0.902152	18	0.227699	-0.739930
9	0.353605	-0.880400	19	0.207204	-0.731578
10	0.348201	-0.858944	20	0.186667	-0.723333

TABLE B.3
 DESIGN POSITIONS OF THE APPLIED EXAMPLE FOR THE
 PRE-SPECIFICATION OF BOTH GROUND PIVOTS FORMULATION

#	x	y	#	x	y
1	-0.207019	-2.182090	11	2.063340	-0.938363
2	0.0687999	-2.239100	12	2.153400	-0.674308
3	0.347610	-2.240690	13	2.191820	-0.401537
4	0.624026	-2.193040	14	2.178680	-0.111425
5	0.892661	-2.102330	15	2.187730	0.167889
6	1.147710	-1.975820	16	2.302040	0.424395
7	1.383080	-1.821450	17	2.547380	0.549207
8	1.596310	-1.638030	18	2.771820	0.399482
9	1.783540	-1.427380	19	2.881780	0.093067
10	1.940770	-1.192140	20	2.896430	-0.145470

B.4.1 The general case (no dimensions pre-specified)

The table B.4 gives the 10 solution values of the general case applied example based on lowest absolute cost value. Figure 4.5(b), with Fig. 4.5(a) and Fig. 4.5(d) are among the lowest costs.

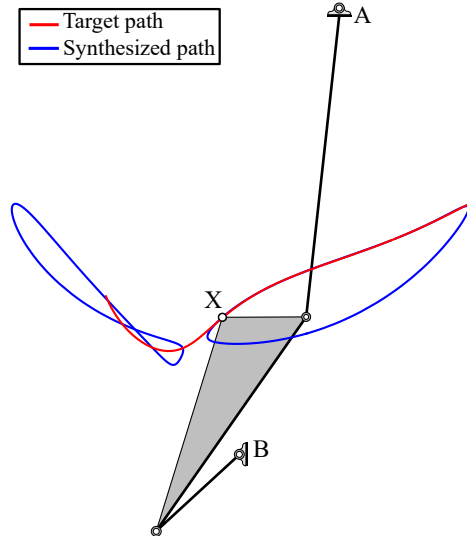


Figure B.1. The computed solution, the global minimum, with the absolute smallest cost function for the zero dimensions pre-specified example.

Figure B.1 shows the computed corresponding to the lowest absolute cost value. This solution is the global minimum, the other local minimum corresponds to the eighth solution of Table B.4. The other solutions in the table are saddle points. Cognate transformations for these solutions can be computed using the formulations given in B.1.

TABLE B.4

THE DIMENSIONS OF THE TOP TEN SOLUTIONS AS PER LOWEST ABSOLUTE COST VALUE FOR THE GENERAL CASE EXAMPLE.
 NOTE THAT FIG. 4.5(B), FIG. 4.5(A), AND FIG. 4.5(D) ARE THE THIRD, FIFTH, AND NINTH LOWEST COSTS, RESPECTIVELY.

	1	2	3	4	5
A	$-0.0854 - 0.0461i$	$-0.0763 - 0.0692i$	$-0.217 - 0.370i$	$-0.418 + 0.0444i$	$-0.0406 - 0.304i$
A^*	$-0.0854 + 0.0461i$	$-0.0763 + 0.0692i$	$-0.217 + 0.370i$	$-0.418 - 0.0444i$	$-0.0406 + 0.304i$
B	$-0.277 - 0.895i$	$-0.343 - 0.143i$	$0.0820 - 0.194i$	$-0.0963 - 0.862i$	$-0.299 - 0.195i$
B^*	$-0.277 + 0.895i$	$-0.343 + 0.143i$	$0.0820 + 0.194i$	$-0.0963 + 0.862i$	$-0.299 + 0.195i$
l_1	0.591	0.159	0.110	0.679	0.190
l_2	0.498	0.182	0.180	0.142	0.159
l_3	0.216	0.0630	0.287	0.4089	0.0694
Q	$0.185 - 0.262i$	$1.469 + 2.763i$	$-1.216 - 1.125i$	$0.366 + 0.264i$	$-0.614 + 2.320i$
Q^*	$0.185 + 0.262i$	$1.469 - 2.763i$	$-1.216 + 1.125i$	$0.366 - 0.264i$	$-0.614 - 2.320i$
Cost	$1.157 \cdot 10^{-8}$	$1.788 \cdot 10^{-8}$	$2.00875 \cdot 10^{-8}$	$3.647 \cdot 10^{-8}$	$4.985 \cdot 10^{-8}$
Max Dev	0.168	0.0971	0.208	0.410	0.115
	6	7	8	9	10
A	$-0.399 + 0.00678i$	$-0.179 - 0.531i$	$-0.142 - 0.962i$	$-0.0111 - 0.272i$	$-0.353 + 0.0308i$
A^*	$-0.399 - 0.00678i$	$-0.179 + 0.531i$	$-0.142 + 0.962i$	$-0.0111 + 0.272i$	$-0.353 - 0.0308i$
B	$-0.0773 - 0.225i$	$-0.385 - 0.772i$	$-0.388 - 0.128i$	$-0.362 - 0.138i$	$-0.209 - 0.0689i$
B^*	$-0.0773 + 0.225i$	$-0.385 + 0.772i$	$-0.388 + 0.128i$	$-0.362 + 0.138i$	$-0.209 + 0.0689i$
l_1	0.0593	0.195	0.446	0.205	0.0733
l_2	0.278	0.141	0.102	0.222	0.198
l_3	0.176	0.386	0.525	0.0524	0.0938
Q	$1.903 - 1.338i$	$-1.100 + 0.575i$	$0.760 - 0.385i$	$-0.377 + 1.842i$	$1.955 - 2.691i$
Q^*	$1.903 + 1.338i$	$-1.100 - 0.575i$	$0.760 + 0.385i$	$-0.377 - 1.842i$	$1.955 + 2.691i$
Cost	$5.154 \cdot 10^{-8}$	$6.134 \cdot 10^{-8}$	$6.708 \cdot 10^{-8}$	$7.346 \cdot 10^{-8}$	$1.622 \cdot 10^{-7}$
Max Dev	0.118	0.230	0.487	0.0970	0.115

TABLE B.5

TABLE SHOWING THE DIMENSIONS OF THE TEN LOWEST
 ABSOLUTE COSTS VALUES FOR THE ONE DIMENSION
 PRE-SPECIFIED APPLIED EXAMPLE.

	1	2	3	4	5
A	$0.137 - 0.973i$	$0.135 - 0.974i$	$0.148 - 0.936i$	$0.170 - 0.919i$	$0.104 - 0.984i$
A^*	$0.137 + 0.973i$	$0.135 + 0.974i$	$0.148 + 0.936i$	$0.170 + 0.919i$	$0.104 + 0.984i$
B	0	0	0	0	0
B^*	0	0	0	0	0
l_1	0.239	0.241	0.313	0.333	0.271
l_2	0.130	0.139	0.684	0.730	0.245
l_3	0.985	0.977	0.418	0.380	0.995
Q	$-0.0498 + 0.0535i$	$-0.0452 + 0.0536i$	$-0.0163 + 0.147i$	$-0.0132 + 0.200i$	$0.00664 + 0.0578i$
Q^*	$-0.0498 - 0.0535i$	$-0.0452 - 0.0536i$	$-0.0163 - 0.147i$	$-0.0132 - 0.200i$	$0.00664 - 0.0578i$
Cost	0.190	0.200	0.274	0.2846	0.431
Max Dev	0.447	0.449	0.295	0.272	0.443
	6	7	8	9	10
A	$0.336 - 0.948i$	$0.0898 - 0.989i$	$0.348 - 0.948i$	$0.502 - 1.183i$	$0.00658 - 1.033i$
A^*	$0.336 + 0.948i$	$0.0898 + 0.989i$	$0.348 + 0.948i$	$0.502 + 1.183i$	$0.00658 + 1.033i$
B	0	0	0	0	0
B^*	0	0	0	0	0
l_1	0.139	0.286	0.115	0.185	0.274
l_2	0.383	0.206	0.325	2.118	0.958
l_3	1.260	0.960	1.246	1.0345	0.189
Q	$-0.271 - 0.0374i$	$0.0269 + 0.0418i$	$-0.257 - 0.0953i$	$0.171 + 0.0178i$	$0.0420 - 0.114i$
Q^*	$-0.271 + 0.0374i$	$0.0269 - 0.0418i$	$-0.257 + 0.0953i$	$0.171 - 0.0178i$	$0.0420 + 0.114i$
Cost	0.448	0.473	0.507	0.537	0.545
Max Dev	0.0957	0.520	0.141	0.0526	0.222

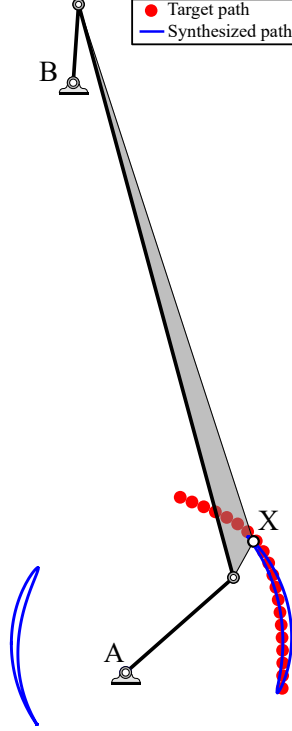


Figure B.2. The computed solution with the absolute smallest cost function for the one dimension pre-specified example.

B.4.2 One dimension pre-specified

A challenge to choosing the solution with the lowest cost value in this situation is that the solution cognates are constrained to those only satisfying the dimension pre-specification. Usually, as in the general case, one may refer to a cognate solution from the group of six. However, in this scenario, we only have one other cognate that satisfies our dimension pre-specification.

Our computations recovered designs similar to the reference, [98], which was the inspiration for this example.

In fact, when sorting the solutions based off different error metrics, such as minimum nearest distance to the curve from a specified position, we can find designs such as this. This metric, as well as the max distance between specified points and their

nearest point on the solution curve (maximum deviation), is one such way to sort solutions. The design and design dimensions are presented in Fig. B.3. This solution is a saddle point and, although it bears a strong resemblance to the reference mechanism, it has too high a cost function for it to appear among desirable solutions when sorted by cost.

TABLE B.6

NUMERICAL VALUES OF THE ONE DIMENSION PRE-SPECIFIED
SOLUTION SHOWN IN FIG. B.3 THAT BEARS THE HIGHEST
RESEMBLANCE TO THE REFERENCE PATH.

A	$-0.684 + 0.338i$
A^*	$-0.684 - 0.338i$
B	0
B^*	0
l_1	1.357
l_2	0.145
l_3	0.744
Q	$0.430 - 3.161i$
Q^*	$0.430 + 3.161i$
Cost	2393.392
Max Dev	0.449

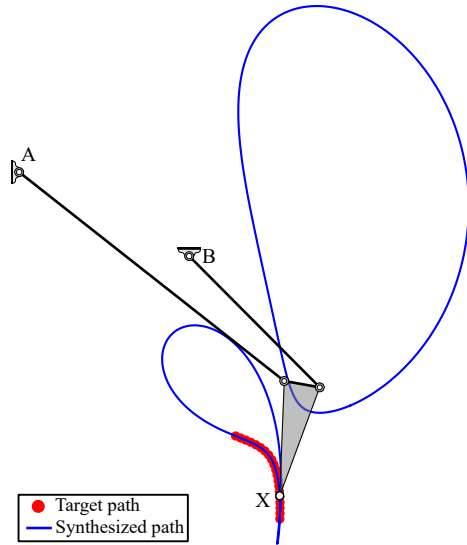


Figure B.3. The solution design, dimensions given in B.6, that bears the highest similarity to the reference design.

B.4.3 Two dimensions pre-specified

Since these values exhibit cognate groups of one member, these solution dimensions are the only designs available for the respective coupler curve.

TABLE B.7

TABLE SHOWING THE DIMENSIONS OF THE TEN LOWEST
 ABSOLUTE COSTS VALUES FOR THE TWO DIMENSION
 PRE-SPECIFIED APPLIED EXAMPLE.

	1	2	3	4	5
A	$0.0101 + 1.0506i$				
A^*	$0.0101 - 1.0506i$				
B	$0.137 - 0.211i$				
B^*	$0.137 + 0.211i$				
l_1	1.147	1.140	3.0964	1.218	1.104
l_2	1.258	1.072	0.855	0.90627	1.0913
l_3	1.139	0.994	2.397	0.867	0.972
Q	$1.117 + 1.295i$	$0.492 + 1.956i$	$0.759 + 0.357i$	$-0.415 + 2.261i$	$0.877 + 1.814i$
Q^*	$1.117 - 1.295i$	$0.4915 - 1.956i$	$0.75885 - 0.357i$	$-0.415 - 2.261i$	$0.877 - 1.814i$
Cost	9.277	16.461	20.0618	20.193	20.422
Max Dev	1.695	1.325	2.436	0.724	1.649
	6	7	8	9	10
A	$0.0101 + 1.0506i$				
A^*	$0.0101 - 1.0506i$				
B	$0.137 - 0.211i$				
B^*	$0.137 + 0.211i$				
l_1	1.182	0.489	0.676	1.297	1.235
l_2	0.963	1.0861	1.155	0.481	0.532
l_3	0.914	0.581	0.728	0.443	0.497
Q	$0.0235 + 2.201i$	$2.140 + 1.593i$	$1.663 + 1.616i$	$-2.767 + 3.0684i$	$-1.642 + 3.503i$
Q^*	$0.0235 - 2.201i$	$2.140 - 1.593i$	$1.663 - 1.616i$	$-2.767 - 3.0684i$	$-1.642 - 3.503i$
Cost	28.679	52.268	76.261	146.184	167.135
Max Dev	0.949	0.708	1.0429	0.727	0.705

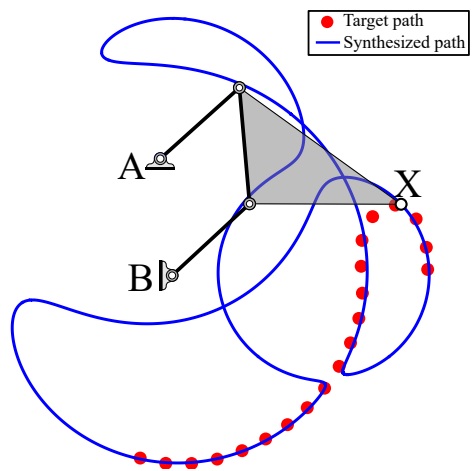


Figure B.4. The computed solution with the absolute smallest cost function for the two dimension pre-specified example.

BIBLIOGRAPHY

1. R. P. Agarwal, R. P. Agarwal, and V. Lakshmikantham. *Uniqueness and nonuniqueness criteria for ordinary differential equations*, volume 6. World Scientific, 1993.
2. E. L. Allgower and K. Georg. *Introduction to Numerical Continuation Methods*. Society for Industrial and Applied Mathematics, 2003.
3. H. Alt. Über die erzeugung gegebener ebener kurven mit hilfe des gelenkviereckes. *Z. Angew. Math. Mech.*, 3(1):13–19, 1923.
4. J. Angeles. Is there a characteristic length of a rigid-body displacement? *Mechanism and Machine Theory*, 41(8):884–896, Aug. 2006.
5. S. S. Balli and S. Chand. Defects in link mechanisms and solution rectification. *Mechanism and Machine Theory*, 37(9):851–876, 2002.
6. A. Baskar. *Optimal Kinematic Synthesis via Saddle Graphs Computed by Random Monodromy Loops*. PhD thesis, University of Notre Dame, 2024.
7. A. Baskar and M. Plecnik. Synthesis of Six-bar Timed Curve Generators of Stephenson-type Using Random Monodromy Loops. *Journal of Mechanisms and Robotics*, 13(1), 2020.
8. A. Baskar and M. Plecnik. Synthesis of Watt-Type Timed Curve Generators and Selection From Continuous Cognate Spaces. *Journal of Mechanisms and Robotics*, 13(5), May 2021.
9. A. Baskar, C. Hills, M. Plecnik, and J. D. Hauenstein. Estimating the Complete Solution Set of the Approximate Path Synthesis Problem for Four-Bar Linkages Using Random Monodromy Loops. In *ASME 2022 International Design Engineering Technical Conferences and Computers and Information in Engineering Conference*. American Society of Mechanical Engineers Digital Collection, Nov. 2022.
10. S. Basu, M.-F. Roy, M. Safey El Din, and E. Schost. A baby step–giant step roadmap algorithm for general algebraic sets. *Found. Comput. Math.*, 14(6):1117–1172, 2014.

11. D. J. Bates and M. Niemerg. Using monodromy to avoid high precision in homotopy continuation. *Mathematics in Computer Science*, 8(2):253–262, Jun 2014.
12. D. J. Bates, J. D. Hauenstein, A. J. Sommese, and C. W. Wampler. Bertini: Software for Numerical Algebraic Geometry.
13. D. J. Bates, J. D. Hauenstein, A. J. Sommese, and C. W. Wampler. Adaptive multiprecision path tracking. *SIAM Journal on Numerical Analysis*, 46(2):722–746, 2008.
14. D. J. Bates, J. D. Hauenstein, A. J. Sommese, and C. W. Wampler. Adaptive multiprecision path tracking. *SIAM Journal on Numerical Analysis*, 46(2):722–746, 2008.
15. D. J. Bates, J. D. Hauenstein, A. J. Sommese, and C. Wampler II. Stepsize control for path tracking. *Contemporary Mathematics*, 496:21, 2009.
16. D. J. Bates, J. D. Hauenstein, C. Peterson, and A. J. Sommese. *Numerical Decomposition of the Rank-Deficiency Set of a Matrix of Multivariate Polynomials*, pages 55–77. Springer Vienna, Vienna, 2010.
17. D. J. Bates, J. D. Hauenstein, and A. J. Sommese. Efficient path tracking methods. *Num. Algorithms*, 58(4):451–459, 2011.
18. D. J. Bates, J. D. Hauenstein, A. J. Sommese, and C. W. Wampler. *Numerically solving polynomial systems with Bertini*, volume 25 of *Software, Environments, and Tools*. Society for Industrial and Applied Mathematics (SIAM), Philadelphia, PA, 2013.
19. A. S. Beloiu and K. C. Gupta. A unified approach for the investigation of branch and circuit defects. *Mechanism and Machine Theory*, 32(5):539–557, 1997.
20. C. Beltrán and A. Leykin. Robust certified numerical homotopy tracking. *Foundations of Computational Mathematics*, 13:253–295, 2013.
21. J. L. Blechschmidt and J. J. Uicker, Jr. Linkage Synthesis Using Algebraic Curves. *Journal of Mechanisms, Transmissions, and Automation in Design*, 108(4):543–548, Dec. 1986.
22. O. Bohigas, M. E. Henderson, L. Ros, and J. M. Porta. A singularity-free path planner for closed-chain manipulators. In *2012 IEEE International Conference on Robotics and Automation*, pages 2128–2134. IEEE, 2012.
23. O. Bohigas, M. Manubens, and L. Ros. *Singularities of Robot Mechanisms: Numerical Computation and Avoidance Path planning*, volume 41. Springer, 2016.

24. D. A. Brake, J. D. Hauenstein, and A. J. Sommese. Numerical local irreducible decomposition. In *International Conference on Mathematical Aspects of Computer and Information Sciences*, pages 124–129. Springer, 2015.
25. D. A. Brake, J. D. Hauenstein, and A. C. Liddell. Decomposing Solution Sets of Polynomial Systems Using Derivatives. In G.-M. Greuel, T. Koch, P. Paule, and A. Sommese, editors, *Mathematical Software – ICMS 2016*, Lecture Notes in Computer Science, pages 127–135. Springer International Publishing, 2016.
26. D. A. Brake, J. D. Hauenstein, and A. C. Liddell Jr. Validating the completeness of the real solution set of a system of polynomial equations. In *Proceedings of the ACM on International Symposium on Symbolic and Algebraic Computation*, pages 143–150, 2016.
27. D. A. Brake, J. D. Hauenstein, A. P. Murray, D. H. Myszka, and C. W. Wampler. The Complete Solution of Alt–Burmester Synthesis Problems for Four-Bar Linkages. *Journal of Mechanisms and Robotics*, 8(4):041018, 04 2016.
28. R. R. Bulatović, S. R. Đorđević, and V. S. Đorđević. Cuckoo Search algorithm: A metaheuristic approach to solving the problem of optimum synthesis of a six-bar double dwell linkage. *Mechanism and Machine Theory*, 61:1–13, Mar. 2013.
29. R. R. Bulatović, G. Miodragović, and M. S. Bošković. Modified Krill Herd (MKH) algorithm and its application in dimensional synthesis of a four-bar linkage. *Mechanism and Machine Theory*, 95:1–21, Jan. 2016.
30. L. Burmester. *Lehrbuch der Kinematic*. Verlag Von Arthur Felix, 1886.
31. J. Canny. *The complexity of robot motion planning*. MIT press, 1988.
32. S. Caro, D. Chablat, A. Goldsztejn, D. Ishii, and C. Jermann. A branch and prune algorithm for the computation of generalized aspects of parallel robots. *Artificial Intelligence*, 211:34–50, 2014.
33. D. G. Chapman. Some properties of the hypergeometric distribution with applications to zoological censuses. *Univ. Calif. Stat.*, 1:60–131, 1951.
34. F. Chazal and A. Lieutier. Weak feature size and persistent homology: computing homology of solids in \mathbb{R}^n from noisy data samples. In *Proceedings of the twenty-first annual symposium on Computational geometry*, pages 255–262. ACM, 2005.
35. T. Chen and T.-Y. Li. Spherical projective path tracking for homotopy continuation methods. *Communication in Information and Systems*, 12(3):195–220, 2012.

36. D. Cox, J. Little, and D. O’Shea. *Ideals, Varieties, and Algorithms: An Introduction to Computational Algebraic Geometry and Commutative Algebra*. Springer-Verlag, 1997.
37. S. Di Rocco, D. Eklund, and O. Gäßvert. Sampling and homology via bottlenecks. *Mathematics of Computation*, 91(338):2969–2995, 2022.
38. S. Di Rocco, P. B. Edwards, D. Eklund, O. Gäßvert, and J. D. Hauenstein. Computing geometric feature sizes for algebraic manifolds. *SIAM Journal on Applied Algebra and Geometry*, 7(4):716–741, 2023.
39. T. Duff, C. Hill, A. Jensen, K. Lee, A. Leykin, and J. Sommars. Solving polynomial systems via homotopy continuation and monodromy. *IMA Journal of Numerical Analysis*, 39(3):1421–1446, July 2019.
40. E. Dufresne, P. Edwards, H. Harrington, and J. Hauenstein. Sampling real algebraic varieties for topological data analysis. In *2019 18th IEEE International Conference On Machine Learning And Applications (ICMLA)*, pages 1531–1536. IEEE, 2019.
41. S. Ebrahimi and P. Payvandy. Efficient constrained synthesis of path generating four-bar mechanisms based on the heuristic optimization algorithms. *Mechanism and Machine Theory*, 85:189–204, Mar. 2015.
42. P. B. Edwards, A. Baskar, C. Hills, M. Plecnik, and J. D. Hauenstein. Output mode switching for parallel five-bar manipulators using a graph-based path planner. In *2023 IEEE International Conference on Robotics and Automation (ICRA)*, pages 9735–9741, 2023.
43. D. Eklund. The numerical algebraic geometry of bottlenecks. *Advances in Applied Mathematics*, 142:102416, 2023.
44. H. Federer. Curvature measures. *Trans. Amer. Math. Soc.*, 93:418–491, 1959.
45. R. L. Fox and K. D. Willmert. Optimum Design of Curve-Generating Linkages With Inequality Constraints. *Journal of Engineering for Industry*, 89(1):144–151, Feb. 1967.
46. R. Ghrist. *Elementary Applied Topology*. CreateSpace, 2014.
47. C. G. Gibson and P. E. Newstead. On the geometry of the planar 4-bar mechanism. *Acta Applicandae Mathematica*, 7(2):113–135, Oct 1986.
48. C. Gosselin and J. Angeles. Singularity analysis of closed-loop kinematic chains. *IEEE Transactions on Robotics and Automation*, 6(3):281–290, June 1990.
49. F. Grashof. Theoretische maschinenlehre. 1875.

50. K. Grove. Critical point theory for distance functions. In *Differential geometry: Riemannian geometry (Los Angeles, CA, 1990)*, volume 54 of *Proc. Sympos. Pure Math.*, pages 357–385. Amer. Math. Soc., Providence, RI, 1993.
51. A. Guigue and M. Hayes. Continuous approximate synthesis of planar function-generators minimising the design error. *Mechanism and Machine Theory*, 101: 158–167, 07 2016.
52. L. Guo, Y. Zhang, J. Wu, and Y. an Yao. Combination of different trajectory description approaches improves the trajectory synthesis performance: Validation by a coarse-to-fine method. *Mechanism and Machine Theory*, 187:105370, 2023.
53. W. Hao, J. D. Hauenstein, B. Hu, Y. Liu, A. J. Sommese, and Y.-T. Zhang. Continuation along bifurcation branches for a tumor model with a necrotic core. *J. Sci. Comput.*, 53:395–413, 2012.
54. P. E. Hart, N. J. Nilsson, and B. Raphael. A formal basis for the heuristic determination of minimum cost paths. *IEEE transactions on Systems Science and Cybernetics*, 4(2):100–107, 1968.
55. J. D. Hauenstein. Numerically computing real points on algebraic sets. *Acta Appl. Math.*, 125:105–119, 2013.
56. J. D. Hauenstein and A. C. Liddell, Jr. Certified predictor-corrector tracking for newton homotopies. *J. Symb. Comput.*, 74:239–254, 2016.
57. J. D. Hauenstein and M. H. Regan. Adaptive strategies for solving parameterized systems using homotopy continuation. *Applied Mathematics and Computation*, 332:19–34, 2018.
58. J. D. Hauenstein and M. H. Regan. Real monodromy action. *Applied Mathematics and Computation*, 373:124983, May 2020.
59. J. D. Hauenstein and J. I. Rodriguez. Multiprojective witness sets and a trace test. *Advances in Geometry*, 20(3):297–318, 2020.
60. J. D. Hauenstein and S. N. Sherman. Using Monodromy to Statistically Estimate the Number of Solutions. In W. Holderbaum and J. M. Selig, editors, *2nd IMA Conference on Mathematics of Robotics*, Springer Proceedings in Advanced Robotics, pages 37–46. Springer International Publishing, 2022.
61. J. D. Hauenstein and A. J. Sommese. Witness sets of projections. *Applied Mathematics and Computation*, 217(7):3349–3354, Dec. 2010.
62. J. D. Hauenstein, A. J. Sommese, and C. W. Wampler. Regeneration homotopies for solving systems of polynomials. *Math. Comp.*, 80(273):345–377, 2011.

63. J. D. Hauenstein, L. Oeding, G. Ottaviani, and A. J. Sommese. Homotopy techniques for tensor decomposition and perfect identifiability. *Journal fÃ¼r die reine und angewandte Mathematik (Crelles Journal)*, 2019(753):1–22, 2019.
64. M. E. Henderson. Multiple parameter continuation: computing implicitly defined k -manifolds. *Internat. J. Bifur. Chaos Appl. Sci. Engrg.*, 12(3):451–476, 2002.
65. A. Hernandez, O. Altuzarra, V. Petuya, and E. Macho. Defining Conditions for Nonsingular Transitions Between Assembly Modes. *IEEE Transactions on Robotics*, 25(6):1438–1447, Dec. 2009.
66. C. Hills, A. Baskar, M. Plecnik, and J. D. Hauenstein. Computing complete solution sets for approximate four-bar path synthesis. *Mechanism and Machine Theory*, 196:105628, 2024.
67. E. C. Hills. Prediction of ligament forces by biplane x-rays in subjects with total knee joint implants. Master’s thesis, Northwestern University, 1982.
68. B. Huber and B. Sturmfels. A polyhedral method for solving sparse polynomial systems. *Mathematics of computation*, 64(212):1541–1555, 1995.
69. B. Huber and J. Verschelde. Polyhedral end games for polynomial continuation. *Numerical Algorithms*, 18:91–108, 1998.
70. R. B. Kearfott and Z. Xing. An interval step control for continuation methods. *SIAM Journal on Numerical Analysis*, 31(3):892–914, 1994.
71. D. R. Kincaid and E. W. Cheney. *Numerical analysis: mathematics of scientific computing*, volume 2. American Mathematical Soc., 2009.
72. D. Koladiya, P. S. Shiakolas, and J. Kebrle. Evolutionary Based Optimal Synthesis of Four-Bar Mechanisms. In *ASME 2003 International Mechanical Engineering Congress and Exposition*, pages 539–544. American Society of Mechanical Engineers Digital Collection, May 2008.
73. S. N. Kramer and G. N. Sandor. Selective Precision Synthesis—A General Method of Optimization for Planar Mechanisms. *Journal of Engineering for Industry*, 97(2):689–701, May 1975.
74. C. J. Krebs. Ecological methodology. 1989.
75. P. M. Larochelle. Circuit and Branch Rectification of the Spatial 4C Mechanism, 09 2000.
76. D. W. Lewis and C. K. Gyory. Kinematic Synthesis of Plane Curves. *Journal of Engineering for Industry*, 89(1):173–175, Feb. 1967.
77. F. C. Lincoln. Calculating waterfowl abundance on the basis of banding returns, 1930.

78. C. Lusk. Watt I indirect cognates of four-bar linkages. In *USCToMM Symposium on Mechanical Systems and Robotics*, pages 90–99. Springer International Publishing, May 2022.
79. C. Lusk. Forty-two Watt I indirect cognates of a four-bar via angular-velocity graph coloring. In *ASME 2022 International Design Engineering Technical Conferences and Computers and Information in Engineering Conference*. American Society of Mechanical Engineers Digital Collection, Aug. 2022.
80. C. Lusk. Exact placement of ground pivots using Watt I indirect cognates of a four-bar mechanism. In *ASME 2023 International Design Engineering Technical Conferences and Computers and Information in Engineering Conference*. American Society of Mechanical Engineers Digital Collection, Aug. 2023.
81. K. M. Lynch and F. C. Park. *Modern Robotics: Mechanics, Planning, and Control*. Cambridge University Press, 2017.
82. E. Macho, O. Altuzarra, C. Pinto, and A. Hernandez. Workspaces associated to assembly modes of the 5R planar parallel manipulator. *Robotica*, 26(3):395–403, May 2008.
83. A. Martín del Campo and J. I. Rodriguez. Critical points via monodromy and local methods. *Journal of Symbolic Computation*, 79:559–574, 2017. SI: Numerical Algebraic Geometry.
84. R. McDougall and S. Nokleby. Synthesis of Grashof Four-Bar Mechanisms Using Particle Swarm Optimization. In *ASME 2008 International Design Engineering Technical Conferences and Computers and Information in Engineering Conference*, pages 1471–1475. American Society of Mechanical Engineers Digital Collection, July 2009.
85. A. P. Morgan. A transformation to avoid solutions at infinity for polynomial systems. *Appl. Math. Comput.*, 18(1):77–86, 1986.
86. A. P. Morgan. *Solving Polynomial Systems Using Continuation for Engineering and Scientific Problems*. Society for Industrial and Applied Mathematics, 2009.
87. A. P. Morgan and A. J. Sommese. Coefficient-parameter polynomial continuation. *Appl. Math. Comput.*, 29(2, part II):123–160, 1989.
88. A. P. Morgan and A. J. Sommese. Coefficient-parameter polynomial continuation. *Appl. Math. Comput.*, 29(2):123–160, 1989. Errata: *Appl. Math. Comput.* 51:207 (1992).
89. A. P. Morgan and A. J. Sommese. Coefficient-parameter polynomial continuation. *Applied Mathematics and Computation*, 29(2):123–160, Jan. 1989.

90. A. P. Morgan and C. W. Wampler, II. Solving a Planar Four-Bar Design Problem Using Continuation. *Journal of Mechanical Design*, 112(4):544–550, Dec. 1990.
91. A. P. Morgan, A. J. Sommese, and C. W. Wampler. Computing singular solutions to nonlinear analytic systems. *Numerische Mathematik*, 58:669–684, 1991.
92. A. P. Morgan, A. J. Sommese, and C. W. Wampler. A power series method for computing singular solutions to nonlinear analytic systems. *Numerische Mathematik*, 63:391–409, 1992.
93. A. Müller and D. Zlatanov. *Singular Configurations of Mechanisms and Manipulators*. Springer, 2019.
94. S. O'Connor, M. Plecnik, A. Baskar, and J. Joo. Complete solutions for the approximate synthesis of spherical four-bar function generators. In *ASME 2023 International Design Engineering Technical Conferences and Computers and Information in Engineering Conference*. American Society of Mechanical Engineers Digital Collection, Aug. 2023.
95. C. G. J. Petersen. The yearly immigration of young plaice in the limfjord from the german sea. *Rept. Danish Biol. Sta.*, 6:1–48, 1896.
96. M. Plecnik. *The Kinematic Design of Six-bar Linkages Using Polynomial Homotopy Continuation*. PhD thesis, University of California, Irvine, 2015.
97. M. Plecnik. Ellipse Synthesis of a Five-bar Linkage. In *ASME 2022 International Design Engineering Technical Conferences and Computers and Information in Engineering Conference*, pages IDETC2022-91341, St. Louis, Missouri, USA, 2022.
98. M. M. Plecnik and R. S. Fearing. A Study on Finding Finite Roots for Kinematic Synthesis. In *ASME 2017 International Design Engineering Technical Conferences and Computers and Information in Engineering Conference*, pages V05BT08A083–V05BT08A083. American Society of Mechanical Engineers, Aug. 2017.
99. R. Rao and R. Pawar. Constrained design optimization of selected mechanical system components using rao algorithms. *Applied Soft Computing*, 89:106141, 2020.
100. S. Roberts. On Three-bar Motion in Plane Space. *Proceedings of the London Mathematical Society*, 1(1):14–23, 1875.
101. Y. L. Sarkisyan, K. C. Gupta, and B. Roth. Kinematic Geometry Associated With the Least-Square Approximation of a Given Motion. *Journal of Engineering for Industry*, 95(2):503–510, May 1973.

102. Ö. Selvi and S. Yavuz. Design and Dimensional Optimization of a Novel Walking Mechanism with Firefly Algorithm. In M. I. C. Dede, M. İtik, E.-C. Lovasz, and G. Kiper, editors, *Mechanisms, Transmissions and Applications*, Mechanisms and Machine Science, pages 67–75. Springer International Publishing, 2018.
103. S. N. Sherman, J. D. Hauenstein, and C. W. Wampler. Curve cognate constructions made easy. In *International Design Engineering Technical Conferences and Computers and Information in Engineering Conference*, volume 83990, page V010T10A024. American Society of Mechanical Engineers, 2020.
104. W. D. Shin, W. Stewart, M. A. Estrada, A. J. Ijspeert, and D. Floreano. Elastic-actuation mechanism for repetitive hopping based on power modulation and cyclic trajectory generation. *IEEE Transactions on Robotics*, 39(1):558–571, 2023.
105. S. Sleesongsom and S. Bureerat. Optimal Synthesis of Four-Bar Linkage Path Generation through Evolutionary Computation with a Novel Constraint Handling Technique. *Computational Intelligence and Neuroscience*, 2018:e5462563, Nov. 2018.
106. A. Smaili and N. Diab. Optimum synthesis of hybrid-task mechanisms using ant-gradient search method. *Mechanism and Machine Theory*, 42(1):115–130, Jan. 2007.
107. S. Smale. Newton’s method estimates from data at one point. In *The merging of disciplines: New directions in pure, applied, and computational mathematics: Proceedings of a Symposium Held in Honor of Gail S. Young at the University of Wyoming, August 8–10, 1985. Sponsored by the Sloan Foundation, the National Science Foundation, and Air Force Office of Scientific Research*, pages 185–196. Springer, 1986.
108. G. S. Soh and J. M. McCarthy. The synthesis of six-bar linkages as constrained planar 3R chains. *Mechanism and Machine Theory*, 43(2):160–170, Feb. 2008.
109. A. J. Sommese and C. W. Wampler. *The Numerical Solution of Systems of Polynomials Arising in Engineering and Science*. World Scientific, Singapore, 2005.
110. A. J. Sommese, J. Verschelde, and C. W. Wampler. Symmetric functions applied to decomposing solution sets of polynomial systems. *SIAM Journal on Numerical Analysis*, 40(6):2026–2046, 2002.
111. A. J. Sommese, J. D. Hauenstein, C. Hills, and C. W. Wampler. Branch points of homotopies, Part II: Enumeration and general theory. submitted, 2024.
112. T. Subbian and D. R. Flugrad, Jr. Four-Bar Path Generation Synthesis by a Continuation Method. *Journal of Mechanical Design*, 113(1):63–69, Mar. 1991.

113. S. Telen, M. V. Barel, and J. Verschelde. A robust numerical path tracking algorithm for polynomial homotopy continuation. *SIAM Journal on Scientific Computing*, 42(6):A3610–A3637, 2020.
114. S. Timme. Mixed precision path tracking for polynomial homotopy continuation. *Advances in Computational Mathematics*, 47(5):75, 2021.
115. Y. Tong, D. H. Myszka, and A. P. Murray. Four-bar linkage synthesis for a combination of motion and path-point generation. In *International Design Engineering Technical Conferences and Computers and Information in Engineering Conference*, volume 55935, page V06AT07A054. American Society of Mechanical Engineers, 2013.
116. L. N. Trefethen and J. Weideman. The exponentially convergent trapezoidal rule. *SIAM review*, 56(3):385–458, 2014.
117. L.-W. Tsai and J.-J. Lu. Coupler-Point-Curve Synthesis Using Homotopy Methods. *Journal of Mechanical Design*, 112(3):384–389, Sept. 1990.
118. M. Urizar, V. Petuya, O. Altuzarra, and A. Hernandez. Computing the Configuration Space for Motion Planning between Assembly Modes. In A. Kecskeméthy and A. Müller, editors, *Computational Kinematics*, pages 35–42, Berlin, Heidelberg, 2009. Springer.
119. J. Verschelde, P. Verlinden, and R. Cools. Homotopies exploiting newton polytopes for solving sparse polynomial systems. *SIAM Journal on Numerical Analysis*, 31(3):915–930, 1994.
120. D. D. Wackerly, W. Mendenhall III, and R. L. Scheaffer. *Mathematical Statistics with Applications*. Thomson Brooks/Cole, Belmont, CA, seventh edition, 2008.
121. C. W. Wampler. Bezout number calculations for multi-homogeneous polynomial systems. *Applied mathematics and computation*, 51(2-3):143–157, 1992.
122. C. W. Wampler. Isotropic coordinates, circularity, and Bézout numbers: Planar kinematics from a new perspective. In *Proceedings of the ASME 1996 IDETC/CIE Conference*, 96-IDETC/MECH-1210, Irvine, California, 1996.
123. C. W. Wampler. The geometry of singular foci of planar linkages. *Mechanism and machine theory*, 39(11):1139–1153, 2004.
124. C. W. Wampler, A. P. Morgan, and A. J. Sommese. Complete Solution of the Nine-Point Path Synthesis Problem for Four-Bar Linkages. *Journal of Mechanical Design*, 114(1):153–159, Mar. 1992.

*This document was prepared & typeset with pdfL^AT_EX, and formatted with
NDDiss2_ε classfile (v3.2017.2[2017/05/09])*